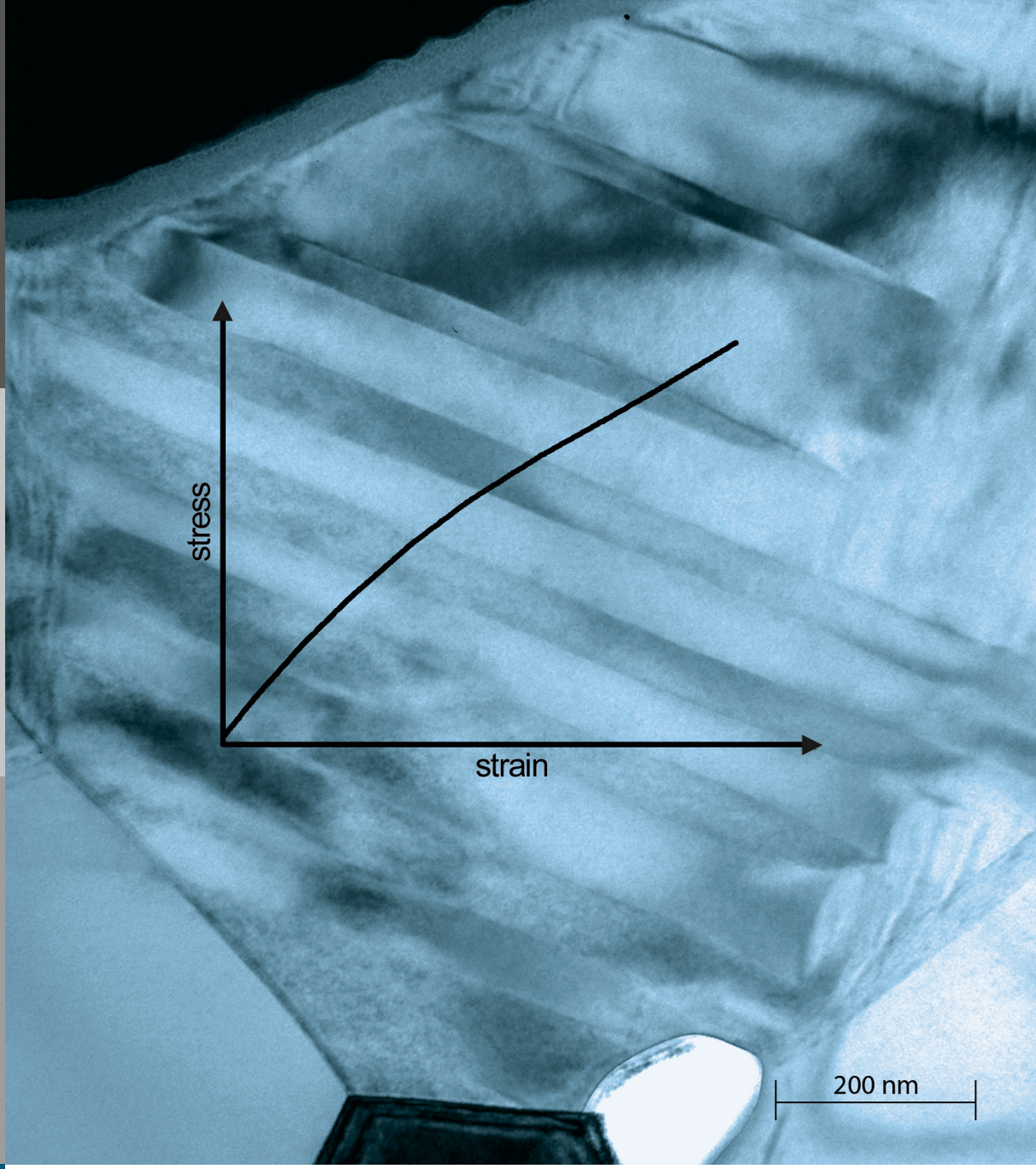

Thermo-Mechanical Properties of Mixed Ion-Electron Conducting Membrane Materials

Bingxin Huang

JÜLICH
FORSCHUNGSZENTRUM

Mitglied der Helmholtz-Gemeinschaft

Schriften des Forschungszentrums Jülich
Reihe Energie & Umwelt / Energy & Environment Band / Volume 124

Forschungszentrum Jülich GmbH
Institute of Energy and Climate Research (IEK)
Microstructure and Properties of Materials (IEK-2)

Thermo-Mechanical Properties of Mixed Ion-Electron Conducting Membrane Materials

Bingxin Huang

Schriften des Forschungszentrums Jülich
Reihe Energie & Umwelt / Energy & Environment Band / Volume 124

ISSN 1866-1793 ISBN 978-3-89336-746-7

Bibliographic information published by the Deutsche Nationalbibliothek.
The Deutsche Nationalbibliothek lists this publication in the Deutsche Nationalbibliografie; detailed bibliographic data are available in the Internet at http://dnb.d-nb.de.

Publisher and Distributor:	Forschungszentrum Jülich GmbH Zentralbibliothek 52425 Jülich Phone +49 (0) 24 61 61-53 68 · Fax +49 (0) 24 61 61-61 03 e-mail: zb-publikation@fz-juelich.de Internet: http://www.fz-juelich.de/zb
Cover Design:	Grafische Medien, Forschungszentrum Jülich GmbH
Printer:	Grafische Medien, Forschungszentrum Jülich GmbH
Copyright:	Forschungszentrum Jülich 2011

Schriften des Forschungszentrums Jülich
Reihe Energie & Umwelt / Energy & Environment Band / Volume 124

D 82 (Diss.,RWTH Aachen University, 2010)

ISSN 1866-1793
ISBN 978-3-89336-746-7

The complete volume is freely available on the Internet on the Jülicher Open Access Server (JUWEL) at http://www.fz-juelich.de/zb/juwel

Kurzfassung

Die vorliegende Arbeit beschäftigt sich mit den thermomechanischen Eigenschaften von $La_{0.58}Sr_{0.4}Co_{0.2}Fe_{0.8}O_{3-\delta}$ (LSCF) und $Ba_{0.5}Sr_{0.5}Co_{0.8}Fe_{0.2}O_{3-\delta}$ (BSCF) – Perovskit-Materialien, die als Sauerstoff-Transport-Membrane (OTM) zur Gastrennung in Betracht gezogen werden. Doppelring-Biege-Tests an scheibenförmigen Proben und instrumentiertes Mikro-Indentionsverfahren wurden als makroskopische beziehungsweise mikroskopische Tests verwendet. Zusätzlich wurden die thermomechanischen Eigenschaften eines dritten möglichen OTM-Materials $La_2NiO_{4+\delta}$ (LNO) untersucht.

Die Ergebnisse der thermomechanischen Messungen des BSCF zeigten eine Anomalie zwischen 200 °C und 400 °C. Insbesondere der temperaturabhänige E-Moduls zeigt ein Minimum um ~ 200 °C. Bruchspannung und Härte weisen ein qualitativ gleiches Verhalten mit einem Minimum zwischen 200 °C und 400 °C auf, bevor sie sich zwischen 500 °C und 800°C erholen. Röntgenbeugunsanalysen bestätigten, dass BSCF im relevanten Temperaturbereich kubisch bleibt. Daher wurde angenommen, dass die Anomalien mit einem Spinübergang des Co^{3+} zusammenhängen, welcher bereits für andere Co-haltige Perovskite berichtet wurde. Diese Annahme konnte experimentell durch Messung der magnetische Suszeptibilitätsmessungen bestätigt werden. Der Bruchweg der Proben wurde durch die mechanischen Anomalien nicht beeinflusst, es wurde nur ein transkristalliner Bruchmodus beobachtet.

Ergänzend zur mechanischen Charakterisierung des BSCF wurde auch für LSCF auch die Temperaturabhänigkeit der Bruchspannung und der Steifigkeit ermittelt. Die Phasen-zusammensetzung des LSCF wurde ‘in-situ‘ mit einem Hochtemperatur-Röntgendiffraktometer (XRD) bestimmt. Es wurden Veränderungen der Phasen-zusammensetzungen in Abhänigkeit der Temperatur festgestellt. Bei Umgebungstemperatur besteht das LSCF-Perovskit-Material

aus zwei Phasen mit: rhomboedrische und kubische Symmetrie. Das Verhältnis der beiden Phasen zu hängt sowohl von der Abkühlgeschwindigkeit als auch von der Atmosphäre ab. Der Übergang von rhomboedrisch zu kubisch erfolgt in Luft zwischen 700 °C und 800 °C. Der Übergang scheint mit einer Veränderung der Wärmekapazität einherzugehen. Die Bruchspannung von LSCF wurde mittels Doppelring-Biege-Tests zwischen Raumtemperatur (RT) und 800 °C bestimmt. Unterhalb 700 °C erhält man nichtlineare Last-Durchbiegungskurven; ein Effekt, welcher der Ferroelastizität der rhomboedrischen Phase zugeordnet werden kann. Sowohl REM als auch TEM untersuchungen bestätigen die Existenz einer Domain-Struktur in den rhomboedrischen Körnern. Der Einfluss der thermischen Vorgeschichte auf die Phasenzusammensetzung und das sich daraus ergebende thermomechanische Verhalten werden diskutiert. Die Härteeindrucks-Bruchzähigkeit ist unempfindlich gegenüber Temperaturveränderungen zwischen RT und 350 °C zu sein.

Zusätzlich zu den zwei perovskitischen Materialien wurden auch die mechanischen Eigenschaften von LNO untersucht. Bruchspannung und Steifigkeit von LNO wurden mittels 4-Punkt-Biegetest von RT bis 900 °C ermiettelt. Die beiden Parameter steigen von RT bis 700 °C leicht an. Die Steifigkeit nimmt jedoch bei noch höheren Temperaturen ab, wohingegen die Bruchspannung ansteigt. Obwohl bis 1000 °C kontinuierlich Sauerstoff aus dem Kristallgitter abgegeben wird, zeigt der thermische Ausdehnungskoeffizient einen nahezu konstanten Wert von RT bis 1000 °C.

Abschließend werden die mechanischen Ergebnisse der drei Membranmaterialien zusammengefasst und im Hinblick auf die praktische Anwendung in der Gastrennung verglichen.

Abstract

The thesis presents thermo-mechanical properties of $La_{0.58}Sr_{0.4}Co_{0.2}Fe_{0.8}O_{3-\delta}$ (LSCF) and $Ba_{0.5}Sr_{0.5}Co_{0.8}Fe_{0.2}O_{3-\delta}$ (BSCF) perovskite materials, which are considered as oxygen transport membranes (OTM) for gas separation units. Ring-on-ring bending test with disk-shaped samples and depth-sensitive micro-indentation have been used as macroscopic and microscopic tests, respectively. In addition, the thermo-mechanical properties of a third OTM candidate material $La_2NiO_{4+\delta}$ (LNO) were investigated.

The results of the thermo-mechanical measurements with the BSCF revealed an anomaly between 200 °C and 400 °C. In particular, the temperature dependence of Young's modulus shows a minimum at ~ 200 °C. Fracture stress and toughness exhibit a qualitatively similar behavior with a minimum between 200 °C and 400 °C, before recovering between 500 °C and 800 °C. X-ray diffraction analyses verified that BSCF remains cubic in the relevant temperature range. Hence the anomalies were assumed to be related to the transition of Co^{3+} spin states reported for other Co-containing perovskites. This assumption could be experimentally confirmed by magnetic susceptibility measurements. The fracture surfaces of the specimens are not affected by the mechanical anomalies at intermediate temperatures, since only a transgranular fracture mode has been observed.

Complementary to the mechanical characterization of BSCF, also the temperature dependency of fracture stress and elastic behavior of LSCF have been determined. Phase compositions of LSCF have been studied by in-situ high temperature XRD. Changes in phase composition with temperature are observed. At ambient temperature the LSCF perovskite material comprises two phases: rhombohedral and cubic symmetry. The ratio of the two phases depends on both cooling rate and atmosphere. The transition of rhombohedral to cubic occurs between 700 °C and 800 °C in air. The transition appears to be associated with a change of heat capacity. The

fracture stress of LSCF was determined on the basis of ring-on-ring bending tests between room temperature (RT) and 800 °C. Below 700 °C non-linear load-displacement curves are obtained, an effect that is attributed to the ferro-elasticity of the rhombohedral phase. Both SEM and TEM verify the existence of a domain structure in the rhombohedral grains. The importance of thermal history on phase composition and the resulting thermo-mechanical behavior is discussed. The indentation fracture toughness appears to be insensitive to temperature variations from RT up to 350 °C.

In addition to the two perovskite materials also mechanical properties of LNO have been determined. Fracture stress and stiffness of LNO were evaluated from RT up to 900 °C based on 4-point bending tests. Both mechanical parameters increase slightly from RT to 700 °C. However, at higher temperatures the stiffness decreases, whereas the fracture stress increases. Although oxygen is continuously released from the lattice up to 1000 °C, the thermal expansion coefficient shows an almost constant value from RT up to 1000 °C.

Finally the mechanical results of the three membrane materials are summarized and compared with respect to practical application in gas separation units.

Table of Contents

Introduction....4

1. Literature review....6

1.1 Transport mechanisms....6

1.2 Perovskites and K_2NiF_4 structured material....7

1.2.1 $Ba_{0.5}Sr_{0.5}Co_{0.8}Fe_{0.2}O_{3-\delta}$ (BSCF)....9

1.2.2 $La_{0.58}Sr_{0.4}Co_{0.8}Fe_{0.2}O_{3-\delta}$ (LSCF)....10

1.2.3 Oxygen permeation flux data for perovskites....12

1.2.4 $La_2NiO_{4+\delta}$ (LNO)....13

1.2.5 Oxygen permeation of BSCF, LSCF and LNO....15

1.3 Thermal and chemical expansion....16

1.4 Spin transition....22

1.5 Fracture stress, fracture toughness and Young's modulus....22

1.6 Creep....30

2. Experiments....34

2.1 BSCF and LSCF perovskites....34

2.1.1 Ring-on-ring tests....35

2.1.2 Micro-indentation....36

2.1.3 X-ray diffraction....39

2.1.4 Thermal property characterization....40

2.1.5 Transmission electron microscopy....40

2.1.6 Creep tests....40

2.2 Experiments with $La_2NiO_{4+\delta}$ (LNO)....41

2.2.1 Four point bending tests....42

2.2.2 Complementary characterizations....43

3. Results and discussion....44

3.1 BSCF....44

3.1.1 Young's modulus and fracture stress....44

3.1.2 Indentation results 47
3.1.3 Comparison of Young's modulus, fracture stress and fracture toughness 55
3.1.4 Fracture surfaces 57
3.1.5 Discussion of possible mechanisms governing the mechanical anomaly 59
3.1.5.1 Structural characterization with XRD 60
3.1.5.2 Phase stability at high temperatures 61
3.1.5.3 Association and dissociation of defects 65
3.1.5.4 Spin transition 66
3.1.5.5 Thermal and chemical expansion 68
3.2 LSCF 70
3.2.1 Non-linearity of load-displacement 70
3.2.2 Young's modulus 72
3.2.2.1 Young's modulus in air 72
3.2.2.2 Young's modulus under vacuum (10^{-5} mbar) 73
3.2.3 Phase compositions of LSCF 75
3.2.4 DTA/TG 77
3.2.5 Thermal and chemical expansion 79
3.2.6 Domain structure of LSCF 80
3.2.7 Fracture stress 84
3.2.8 Indentation 86
3.2.8.1 Temperature dependence 86
3.2.8.2 Cooling rate dependence 87
3.2.9 Magnetic susceptibility 90
3.2.10 Residual stresses 90
3.2.11 Fracture surface 91
3.2.12 Creep 94
3.3 LNO 99
3.3.1 Stiffness of LNO 99

3.3.2 Fracture stress 101
3.3.3 TG/DTA 102
4. Conclusions 104
4.1 BSCF 104
4.2 LSCF 105
4.3 LNO 106
4.4 Comparison of BSCF, LSCF and LNO 106
References 110
List of Figures 121
List of Tables 125
Nomenclature 126
Acknowledgements 129
List of publications 130

Introduction

Global warming is an increasing challenge for mankind with consequences such as rising sea levels, glacier retreat and arctic shrinkage already observed [1-3]. One of the major causes for global warming is attributed to the emission of greenhouse gases. In the atmosphere they absorb and emit radiation within the thermal infrared range. The main greenhouse gases in the Earth's atmosphere are water vapour, carbon dioxide, methane, nitrous oxide, and ozone [4-6]. The increasing greenhouse gas concentrations result from human activity such as fossil fuel burning and deforestation [5-7]. Therefore, efforts are increasingly directed towards a reduction of the CO_2 emission. One option to burn fuels and at the same time not to release CO_2 into atmosphere is separation capture and sequestration. There are three possible technical solutions for CO_2 capture in fossil power plants: post-combustion, oxyfuel and pre-combustion (Figure 1.1). In the post combustion process CO_2 is separated from N_2. The other two solutions utilize air separation before combustion to obtain pure oxygen. In the oxyfuel process the oxygen is used for the combustion, whereas in the pre-combustion, a CO-CO_2 shift reaction is performed.

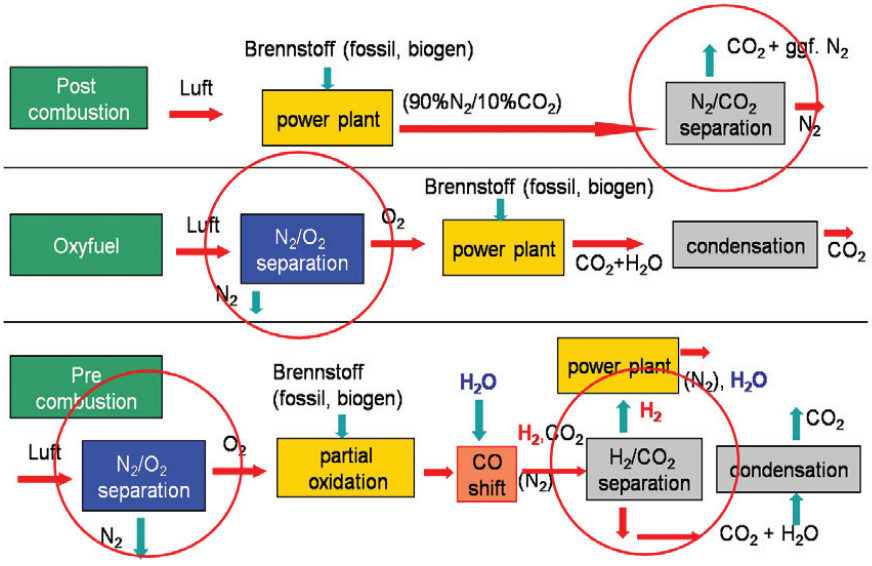

Figure 1.1: Schematic representation of possible separation processes in fossil power plants

The CO_2 capture is in both cases carried out after condensation. In particular, for the N_2/O_2 separation (Figure 1.1) inorganic membranes have been proposed as being more efficient than the established conventional air liquefying techniques.

For application as membranes in power plant, the materials should exhibit high oxygen conductivity, chemical and structural stability in long term operation, compatibility of thermal expansion with metallic structures, and a high resistance to mechanical failure (e.g. fracture stress). The present thesis focuses on three of these inorganic membrane materials $Ba_{0.5}Sr_{0.5}Co_{0.8}Fe_{0.2}O_{3-\delta}$, $La_{0.58}Sr_{0.4}Co_{0.2}Fe_{0.8}O_{3-\delta}$ and $La_2NiO_{4+\delta}$. They all utilize the selective oxygen permeation at elevated temperatures. Due to their mixed ion-electron conductivity (MIEC), the three oxygen transport membranes (OTM) also keep charge neutrality. Besides the functional performances of high oxygen transport the mechanical integrity of the membranes plays a key role in the envisaged gas separation applications. The thesis has the aim to describe the thermo-mechanical behaviour of the three MIEC membranes.

1. Literature review

Mixed ion-electron conductivity (MIEC) materials with high oxygen permeation are currently exploited as promising oxygen transport membranes (OTMs) for gas separation. Perovskites like $Ba_{0.5}Sr_{0.5}Co_{0.8}Fe_{0.2}O_{3-\delta}$ (BSCF) and $La_{0.58}Sr_{0.4}Co_{0.2}Fe_{0.8}O_{3-\delta}$ (LSCF) as well as materials with K_2NiF_4 structure like $La_2NiO_{4+\delta}$ (LNO) have been proposed for OTM application, since they exhibit strong oxygen permeation at elevated temperatures. The oxygen transport mechanisms of these three candidate materials are addressed, and the permeation is compared with data of other perovskite compositions reported in literature. With higher temperature the OTM materials loose oxygen which promotes the oxygen transport through the lattice. The loss of oxygen has in addition impact on the material expansion. Also changes in the spin-state of perovskites can influence the material expansion. The underlying mechanism and results reported to date about this effect are presented. Macro- and micro-mechanical characterizations for perovskites with similar composition as the three materials are reviewed.

1.1 Transport mechanisms

MIEC materials can selectively separate oxygen from air by the lattice diffusion of the oxygen ions [8]. Besides appropriate temperature for diffusion, the driving force for oxygen transport is the difference of the chemical potential of oxygen between the two surfaces of the membrane [9]. The steady flux of oxygen ions is charge compensated by a counter flux of electrons, and the surface activity of oxygen is also enhanced by surface electrons. The transport of oxygen through a dense MIEC membrane involves several successive processes: the surface exchange reaction on the feed side; dissociation of an oxygen molecule into oxygen atoms; combination with electrons to form O^{2-}; lattice diffusion of oxygen ions. The reactions on the sweep side are reverse processes to those of the feed side. The slowest process is expected to determine the overall rate of oxygen permeation [10]. The transport process is schematically presented in Figure 1.2.

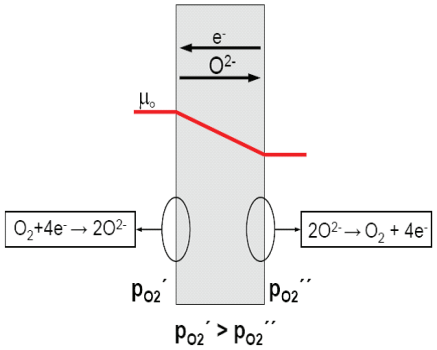

Figure 1.2: Schematic representation of the transport process of oxygen through a membrane with different oxygen partial pressure P_{O2}'>P_{O2}'' on both surfaces

1.2 Perovskites and K_2NiF_4 structured material

Ionic conductivity was first reported in yttrium stabilized zirconia [11]. However, besides the lack of charge compensation, the low permeability and a high operating temperature limit its application in OTM membranes [10, 12]. In both aspects MIEC materials have advantages and are currently applied or developed as promising materials for cathodes of a solid state fuel cell (SOFC) and for ceramic membranes in oxygen separation units [13, 14]. The steady flux of oxygen ions is charge compensated by a counter flux of electrons, and the electrons also enhance the surface exchange process [15].

Among the MIEC materials the perovskites oxides of the type ABO_3 (rare earth metal ions in A sites and transition metal ions in B sites) have been most extensively investigated in the last decades. Perovskite is a general term of a structural family of inorganic materials with the structure of $CaTiO_3$ [10, 16]. The ideal perovskite has cubic symmetry with the space group Pm3m. The B cation is 6-fold and the A cation 12-fold coordinated with the oxygen anions. The structure, which is schematically displayed by Figure 3, reveals that the transition metal ions (B) are located at the centre of the cube, forming an octahedral with 6 nearest oxygen ions. The angles between the six equal B-O bonds are 90 °. A-ions are located at the corners surrounded by twelve equidistant oxygen ions (Figure 3(a)). Alternatively, the structure can

also be viewed with the A cation located in the centre of the cube and B located at the corner (Figure 3(b)) [17].

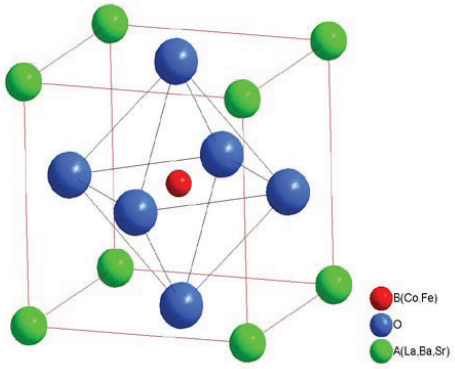

(a) B-ions cube centered

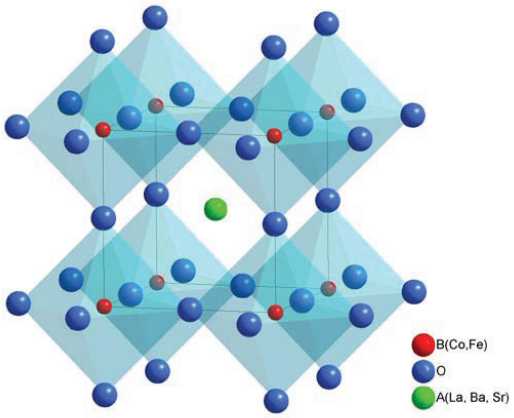

(b) A-ions cube centered

Figure 1.3: Atomic structure of perovskite

In the ideal cubic symmetry, when the atoms are assumed to be closely packed, it can be stated that:

$$2(R_B+R_O)=a \quad (1.1)$$

$$2(R_A+R_O)=\sqrt{2}a \quad (1.2)$$

where R_A, R_B, R_O are the radius of A, B, O atoms, respectively, and a is the lattice constant. Combining the equations (1.1) and (1.2), the relation between the ionic radii is given by:

$$(R_A+R_O)=\sqrt{2}(R_B+R_O) \quad (1.3)$$

With respect to the stability of the cubic symmetry of the perovskites, a tolerance factor (t) has been defined by Goldschmidt [18]:

$$t = \frac{R_A + R_O}{\sqrt{2}(R_B + R_O)} \quad (1.4)$$

Normally, when the tolerance factor (t) is between 0.8 and 1, the perovskite structure is preserved [16]. The ideal cubic perovskite structure is stable only for t-values very close to 1. However in many cases the composition and stoichiometry of the perovskites causes a distorted structure. In fact, orthorhombic, rhombohedral, tetragonal, monoclinic, and triclinic symmetry are frequently observed besides the cubic symmetry [16].

1.2.1 $Ba_{0.5}Sr_{0.5}Co_{0.8}Fe_{0.2}O_{3-\delta}$ (BSCF)

Variants of $Ba_xSr_{1-x}Co_{0.8}Fe_{0.2}O_{3-\delta}$ and $La_xSr_{1-x}Co_{1-y}Fe_yO_{3-\delta}$ with perovskite structure are the most promising oxygen-permeable MIEC materials and currently discussed for membrane application [14, 19-22]. The origin of BSCF can be traced back to $SrCoO_{3-\delta}$, which is an important perovskite-type parent compound [17]. More specifically, BSCF is modifications of $SrCo_{1-y}Fe_yO_{3-\delta}$, which was one of the first perovskites suggested as an oxygen transport membrane [21, 23, 24]. One of the six oxygen lattice positions in $SrCoO_{3-\delta}$ is unoccupied and the oxygen diffusion follows a vacancy mechanism. Also the bond strength of Co-O is relatively weak, so high oxygen conductivity is obtained [25, 26]. However, there is a phase transition from high temperature cubic structure to low temperature hexagonal structure between 800 °C and 900 °C. The high oxygen permeation is only achieved in the cubic structure, but oxygen permeation is low in the hexagonal phase [27-29]. Based on $SrCoO_{3-\delta}$

many groups have studied the oxygen permeation of the doped systems $A_xSr_{1-x}B_yCo_{1-y}O_{3-\delta}$ [21, 30-37]. $SrCo_{0.8}Fe_{0.2}O_{3-\delta}$ was found to exhibit the highest oxygen permeation flux. However, the $SrCo_{0.8}Fe_{0.2}O_{3-\delta}$ has only limited mechanical and phase stability due to the small radius of Sr [24, 31, 38], see equation (1.4). Since the cubic symmetry is stable when the tolerance factor is close to 1, Shao et al. [39] used the large Ba atom to substitute Sr. They found that a 50 % replacement of Sr by Ba was the best composition to stabilize the cubic symmetry. BSCF maintained cubic symmetry up to 1000 °C in the P_{O2} range of 1 to 10^{-5} atm, and had a higher concentration of oxygen vacancies in random distribution [14]. Chen et al. investigated the phase structure, oxygen non-stoichiometry and electrical conductivity of the system $Ba_{0.5}Sr_{0.5}Co_{1-y}Fe_yO_{3-\delta}$ (y = 0.0 - 1.0) [40], and observed a higher oxygen permeation and phase stability in $Ba_{0.5}Sr_{0.5}Co_{0.8}Fe_{0.2}O_{3-\delta}$. Oxygen stoichiometry, oxygen permeation properties and structural stability of BSCF have been extensively investigated [14, 41, 42]. The initial oxygen stoichiometry of BSCF was found to be ~ 2.48 if cooled in air from sintering temperature [14].

1.2.2 $La_{0.58}Sr_{0.4}Co_{0.8}Fe_{0.2}O_{3-\delta}$ (LSCF)

The $La_{1-x}Sr_xCo_{1-y}Fe_yO_{3-\delta}$ perovskite-type oxides, which have been extensively studied for application as membranes for oxygen separation [43, 44], are well known for their excellent electronic and oxygen ionic conductivity at elevated temperature [10, 19, 45-48] (see Table 1.1). Fossdal et al. [49] studied the phase structure of $La_{1-x}Sr_xFeO_{3-\delta}$ in the temperature regime between RT and 1000 °C (Figure 1.4). For $0 < x < 0.2$ the $La_{1-x}Sr_xFeO_{3-\delta}$ material has an orthorhombic structure at RT. With increasing x the perovskite gradually transforms to rhombohedral and cubic symmetry. The cubic symmetry is favoured by a higher content of Sr and high temperature. In particular $La_{0.6}Sr_{0.4}Co_{0.2}Fe_{0.8}O_{3-\delta}$ was extensively studied [47, 50-55].

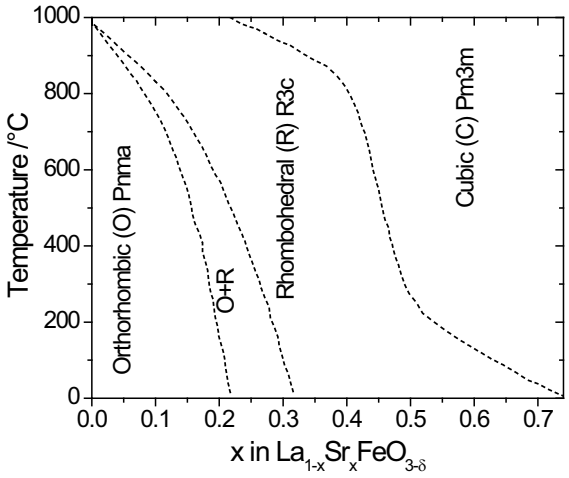

Figure 1.4: Pseudobinary phase diagram for the $La_{1-x}Sr_xFeO_{3-\delta}$ system ($x \leq 0.75$) in air [49]

However, under application-relevant operation conditions the perovskites must in addition to a high oxygen flux rate also exhibit a satisfactory mechanical strength. During membrane operation a high oxygen partial pressure (P_{O2}) and a low P_{O2} are maintained at the two surfaces of the membrane, respectively. As a result, a stable oxygen gradient is generated across the membrane. The material that is exposed to the low P_{O2} loses part of its oxygen, resulting in a reduction of B site cations M^{n+} to a lower valence $M^{(n-1)+}$ [56], and the lattice of the perovskite will expand [57, 58]. It has been verified that a phase transition may also be induced by an oxygen deficiency [59], and hence both effects could cause a mismatch of the lattice parameters on the two surfaces of the membrane. Consequently, stresses are likely to be generated that may lead to membrane fracture.

The $La_{1-x}Sr_xCo_{1-y}Fe_yO_{3-\delta}$ perovskites have a rhombohedral symmetry at low temperature, and transform at higher temperature to a cubic symmetry by a second order phase transition. The transition temperature depends on the amount of dopant [49, 60]. $LaCoO_3$ remains rhombohedral up to its melting point (1740 °C), whereas the transition temperature of LSCF is ~ 750 °C in air. Along with this transition the Young's modulus increases by ~ 50 % [49, 59].

It has been reported that the Young's modulus of $LaCr_{0.79}Mg_{0.05}Al_{0.16}O_{3-\delta}$ (LCMA) increases with decreasing partial pressure of oxygen, which was attributed to oxygen-vacancy related differences in the crystallographic bonding properties [61, 62].

The stress-strain behavior of rhombohedral LSCF is also influenced by its ferro-elasticity [59, 63]. Ferro-elastic deformation results in a hysteresis of the stress-strain behavior [64]. Since there are two equivalent directions of the rhombohedral structure, a spontaneous reorientation of domains can occur under mechanical stress [65]. Ferro-elastic domain switching may increase the fracture toughness of materials [66], and cause stress relaxation in zones of higher stress. Hence, ferro-elasticity is an important non-linear deformation mechanism that needs attention to understand the mechanical behavior of LSCF perovskite.

1.2.3 Oxygen permeation flux data for perovskites

The oxygen flux of reported perovskite-based membranes is compiled in Table 1.1. $La_{1-x}Sr_xCo_yFe_{1-y}O_{3-\delta}$ exhibits a lower oxygen flux than BSCF, but the chemical stability of $La_{1-x}Sr_xCo_yFe_{1-y}O_{3-\delta}$ is more pronounced [10, 50, 67]. Teraoka et al. have investigated the rate of oxygen permeation in the system $La_{1-x}Sr_xCo_{0.4}Fe_{0.6}O_{3-\delta}$ (x=0.0, 0.4, 0.8 and 1), and the rate of oxygen permeation was found to decrease with increasing x value [37].

Table 1.1 Oxygen permeation flux data for perovskite structure membranes

Membrane	Temperature (° C)	J_{O2}(mol·s^{-1}·cm^{-2})	Shape	Thickness (mm)	Reference
$Ba_{0.5}Sr_{0.5}Co_{0.8}Fe_{0.2}O_{3-\delta}$	850-900	8.929×10^{-8} to 1.563×10^{-6}	Disk	1.8	[21] [32] [68]
	800-900	7.068×10^{-7} to 2.307×10^{-6}			
	850-950	1.406×10^{-6} to 3.266×10^{-6}			
$La_{0.6}Ba_{0.4}Co_{0.8}Fe_{0.2}O_{3-\delta}$	860	1.536×10^{-6}	Disk	1.5	[36]
$La_{0.4}Ba_{0.6}Co_{0.2}Fe_{0.8}O_{3-\delta}$	900	3.348×10^{-7}	Disk	2.3-3.1	[69]
$La_{0.2}Ba_{0.8}Co_{0.2}Fe_{0.8}O_{3-\delta}$	900	3.125×10^{-7}	Disk	2.3-3.1	[69]

$La_{0.6}Ca_{0.4}Co_{0.8}Fe_{0.2}O_{3-\delta}$	860	1.364×10^{-6}	Disk	1.5	[36]
$La_{0.4}Ca_{0.6}Co_{0.2}Fe_{0.8}O_{3-\delta}$	900	1.414×10^{-7}	Disk	0.55	[69]
$LaCo_{0.8}Fe_{0.2}O_{3-\delta}$	860	1.786×10^{-8}	Disk	1.5	[36]
$La_{0.6}Sr_{0.4}CoO_{3-\delta}$	870	3.770×10^{-7}	Disk	1	[37]
	850	$\sim1\times10^{-6}$	Disk	0.24-1.3	[70]
	850	1.778×10^{-8}	Disk	1	[24]
	820-860	5.365×10^{-7} to 7.649×10^{-7}	Disk	1.5	[36]
$La_{0.6}Sr_{0.4}Co_{0.2}Fe_{0.8}O_{3-\delta}$	850-900	0.400×10^{-7} to 1.050×10^{-7}	Tube	0.219	[71]
$La_{0.6}Sr_{0.4}Co_{0.4}Fe_{0.6}O_{3-\delta}$	1000-1100	2.530×10^{-8} to 1.280×10^{-7}	Disk	1	[37]
$La_{0.6}Sr_{0.4}Co_{0.8}Fe_{0.2}O_{3-\delta}$	860	4.591×10^{-7}	Disk	1.5	[36]
$La_{0.4}Sr_{0.6}Co_{0.2}Fe_{0.8}O_{3-\delta}$	900	8.185×10^{-8}	Disk	0.55	[72]
	900	4.092×10^{-7}	Disk	2.3-3.1	[69]
$La_{0.2}Sr_{0.8}Co_{0.2}Fe_{0.8}O_{3-\delta}$	900	5.060×10^{-7}	Disk	2.3-3.1	[69]
$La_{0.2}Sr_{0.8}Co_{0.4}Fe_{0.6}O_{3-\delta}$	1000-1100	1.280×10^{-7} to 3.720×10^{-7}	Disk	1	[37]
$La_{0.6}Sr_{0.4}Co_{0.8}Mn_{0.2}O_{3-\delta}$	860	3.720×10^{-7}	Disk	1.5	[36]
$La_{0.6}Sr_{0.4}Co_{0.8}Ni_{0.2}O_{3-\delta}$	860	1.076×10^{-6}	Disk	1.5	[36]
$SrCoO_{3-\delta}$	850-1000	0 to 3.35×10^{-7}	Disk	1	[24]
$SrCo_{0.4}Fe_{0.6}O_{3-\delta}$	1000-1100	7.210×10^{-7}	Disk	1	[37]
$SrCo_{0.8}Fe_{0.2}O_{3-\delta}$	850	1.738×10^{-7}	Disk	1	[24]
	870	2.485×10^{-6}	Disk	1	[37]
	780-850	8.000×10^{-8} to 5.433×10^{-7}	Disk	1-5.5	[31]

1.2.4 $La_2NiO_{4+\delta}$ (LNO)

The LNO material possesses a K_2NiF_4 structure. The ideal crystal structure can be described as an alternation of perovskite layers with rock salt layers along the c-direction [73, 74], as is illustrated in Figure 1.5. The oxygen ion transport in LNO phases occurs via a complex mechanism combining interstitial migration in the rock salt layers and vacancy migration in the perovskite layers [75, 76]. The LNO phases are oxygen-hyperstoichiometric ($\delta > 0$) at

temperatures below ~ 1000 °C. The oxygen non-stoichiometry (δ) is close to 0.14 when slowly cooled in air [77-81].

LNO has certain advantages compared to perovskite materials. They include higher chemical stability, stable thermal expansion, and lower chemical expansion. The isothermal chemical expansion caused by an oxygen pressure gradient is lower than 0.05 % [73, 82], which reduces thermo-mechanical integrity problems for the membrane application.

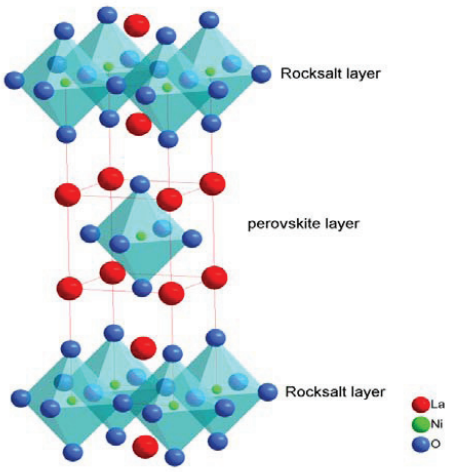

Figure 1.5: Atomic structure of LNO

The oxygen flux of K_2NiF_4 structured membranes reported in literature is compiled in Table 1.2. R_2NiO_4 (R=Pr, Nd, Ni) system exhibits a higher oxygen flux than Ln_2CuO_4 (Ln=Pr, Nd) system.

Table 1.2 Oxygen permeation flux data for K_2NiF_4 structured membranes

Membrane	Temperature (° C)	J_{O2}(mol·s^{-1}·cm^{-2})	Shape	Thickness (mm)	Reference
$Pr_2Ni_{0.75}Cu_{0.25}Ga_{0.05}O_4$	1000	4.967×10^{-6}	Disk	0.5	[83]
$Pr_2Ni_{0.75}Cu_{0.25}Ga_{0.07}O_4$	1000	4.916×10^{-6}	Disk	0.5	[83]
$Pr_2Ni_{0.6}Cu_{0.2}Fe_{0.2}O_4$	900	5.109×10^{-7}	Disk	0.5	[84]

$Pr_2Ni_{0.8}Cu_{0.2}O_4$	900	5.408×10^{-7}	Disk	0.5	[84]
$Pr_2Ni_{0.7}Cu_{0.2}Fe_{0.1}O_4$	900	5.833×10^{-7}	Disk	0.5	[84]
$Pr_2Ni_{0.75}Cu_{0.2}Fe_{0.05}O_4$	900	6.813×10^{-7}	Disk	0.5	[84]
$La_2Ni_{0.88}Fe_{0.02}Cu_{0.10}O_{4+\delta}$	900	1.331×10^{-7}	Disk	1	[85]
$La_2Cu_{0.7}Co_{0.3}O_{4+\delta}$	850	8.159×10^{-8}	Disk	1	[85]
$Pr_2CuO_{4+\delta}$	900	2.507×10^{-9}	Disk	1	[85]
$La_2Ni_{0.90}Fe_{0.10}O_{4+\delta}$	900	8.137×10^{-8}	Disk	1	[85]
$Nd_2CuO_{4+\delta}$	900	4.664×10^{-10}	Disk	1	[85]
$Nd_2Ni_{0.8}Cu_{0.2}O_4$	900	1.250×10^{-7}	Disk	1	[86]
$Pr_2Ni_{0.8}Cu_{0.2}O_4$	900	1.168×10^{-7}	Disk	1	[86]
$La_2Ni_{0.8}Cu_{0.2}O_4$	900	8.965×10^{-8}	Disk	1	[86]
La_2NiO_4	850	8.096×10^{-8}	Disk	1	[73]

1.2.5 Oxygen permeation of BSCF, LSCF and LNO

The oxygen flux as a function of temperature for BSCF, LSCF and LNO is displayed in Figure 1.6 [87]. BSCF exhibits the highest oxygen flux throughout the temperature range. Note that the oxygen flux of LNO is in the application relevant temperature range (~ 800 °C – 900 °C) for OTMs slightly higher than that of LSCF.

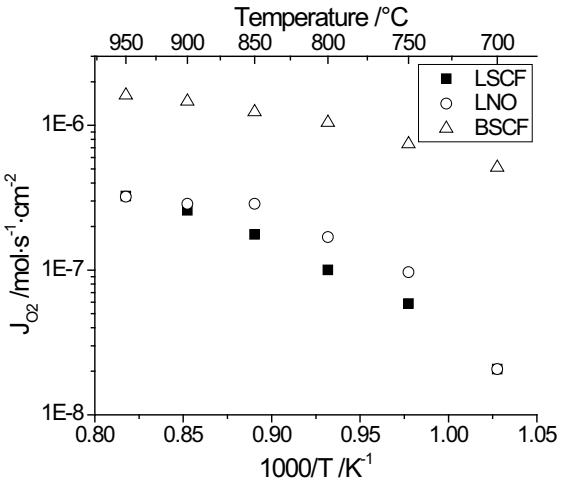

Figure 1.6: Dependence of oxygen flux of LSCF, BSCF und LNO on temperature [87]

1.3 Thermal and chemical expansion

Thermal expansion of materials is an increase in volume as the temperature is raised [88]. The technical thermal expansion coefficient α_{Tech} is calculated by:

$$\alpha_{Tech} = \frac{1}{L_0}\frac{L - L_0}{T - T_0} \tag{1.5}$$

where L is the specimen length measured at a given temperature T, while L_0 corresponds to the initial length of the specimen at RT (T_0). α_{Tech} is an average value of expansion between initial temperature T_0 and a given temperature T. However, in order to recognize transitions in material behaviour with temperature the scientific TEC appears to be more useful. The latter can be expressed by:

$$\alpha_{Sci} = \frac{1}{L}\frac{dL}{dT} \tag{1.6}$$

The thermal expansion of materials is normally only correlated with the anharmonic vibration of the lattice. The potential energy of the lattice as a function of bond length is shown in Figure 1.7. The potential energy is not symmetric with respect to the minimum point (r_0), and the lattice vibration is anharmonic. The curve in the low r regime ($r < r_0$) is steeper, so the bond length has a higher probability to stay in the range of bigger r ($r > r_0$). As a result, the bond length increases as the temperature is raised (Figure 1.7). The anharmonic vibration contributes to the thermal expansion over the whole temperature range, and thus normally the related TEC values remain relatively stable.

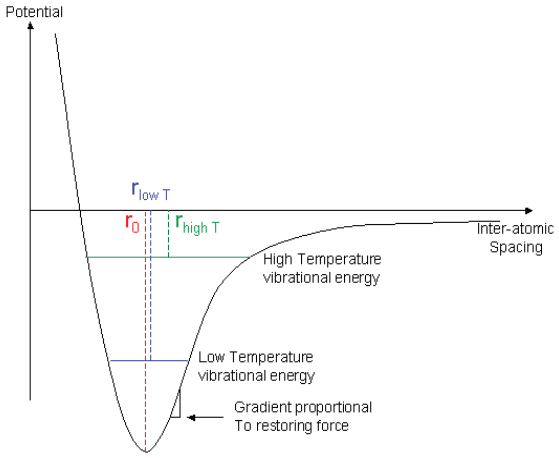

Figure 1.7: Potential energy as a function of bond length

However, the thermal expansion of perovskites might consist of three components: anharmonic lattice vibration, spin transition, and chemical expansion. The lattice expansion due to spin transition will be discussed in section 1.4. Here only the chemical expansion is addressed in more detail.

With the increase of temperature and the decrease of oxygen partial pressure, perovskites may lose part of its oxygen, and at the same time cations are reduced to a lower valence:

$$2M^{n+} + O^{2-} \rightarrow 2M^{(n-1)+} + O_2(g) \qquad (1.7)$$

Along with this process which is conventionally called chemical expansion the lattice expands in addition to the anharmonic vibration expansion (Figure 1.8) [46, 49, 89]. Two possible explanations for this chemical expansion are given in the literature [46]: i) the repulsion forces between mutually exposed cations when oxygen ions are released from the lattice; ii) the increase in cation size due to the reduction of the cations from higher to lower valences, an effect which occurs simultaneously with the creation of oxygen vacancies in order to maintain electrical neutrality.

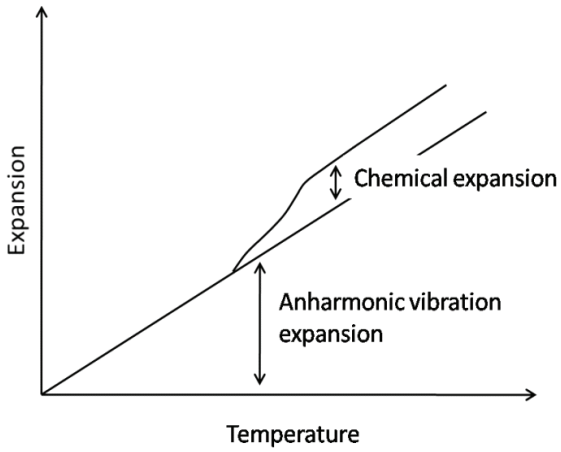

Figure 1.8: Contribution of chemical expansion to the thermal expansion

Zhu et al [90] studied the thermal expansion in the $Ba_xSr_{1-x}Co_{0.8}Fe_{0.2}O_{3-\delta}$ system in air (Figure 1.9). All thermal expansion curves are nonlinear, and a chemical expansion is observed for all compositions above 500 - 600 °C. Samples with x = 0.1 and 0.2 exhibit a normal expansion below ~ 500 °C, but a much higher chemical expansion above ~ 500 °C. Samples with x = 0, 0.4, 0.5 and 0.6 have similar expansion rates, but the expansion rates fluctuate with Ba content.

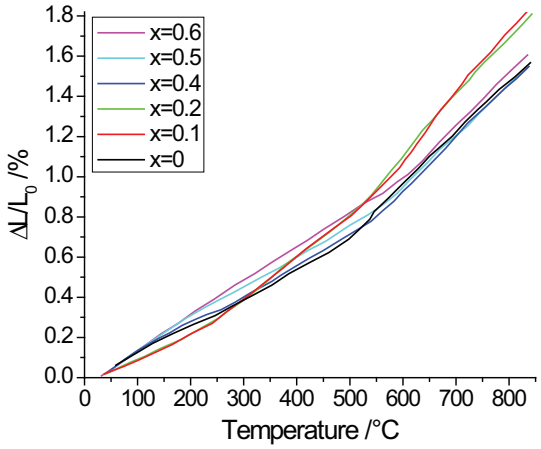

Figure 1.9: Thermal expansion behaviour of $Ba_xSr_{1-x}Co_{0.8}Fe_{0.2}O_{3-\delta}$ in air [90]

Lein et al. [58] studied the lattice constant of $La_{0.5}Sr_{0.5}Fe_{1-x}Co_xO_{3-\delta}$ as a function of temperature in air and nitrogen (Figure 1.10). The lattice constant increases more rapidly in nitrogen than in air due to the chemical expansion. Even in air the chemical expansion contributes to the increase of the lattice constant at high temperature. Therefore, changes in the slope can be observed at about 600 °C.

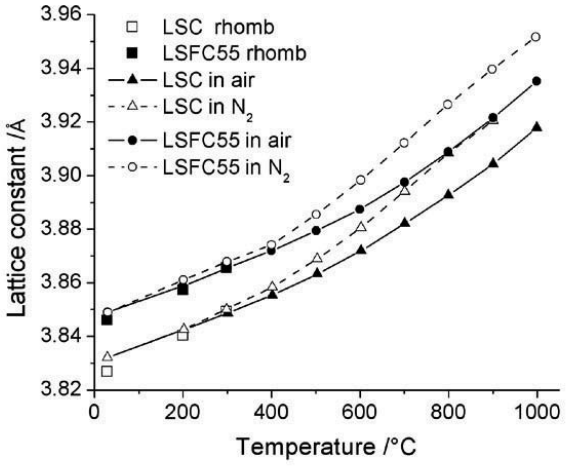

Figure 1.10: The cubic lattice constant of $La_{0.5}Sr_{0.5}Fe_{0.5}Co_{0.5}O_{3-\delta}$ (LSCF55) and $La_{0.5}Sr_{0.5}CoO_{3-\delta}$ (LSC) as a function of temperature in air and in nitrogen atmosphere. The solid and dashed lines are guides to the eye. The squares are the pseudo cubic lattice constant in air obtained from a rhobohedral model [58].

Thermal expansion data of $La_{0.4}Sr_{0.6}Co_{0.2}Fe_{0.8}O_{3-\delta}$ in air were reported by Swierczek [52]. The thermal expansion of $La_{0.4}Sr_{0.6}Co_{0.2}Fe_{0.8}O_{3-\delta}$ is lower compared with BSCF, and a chemical expansion is observed above ~ 600 °C (Figure 1.11)

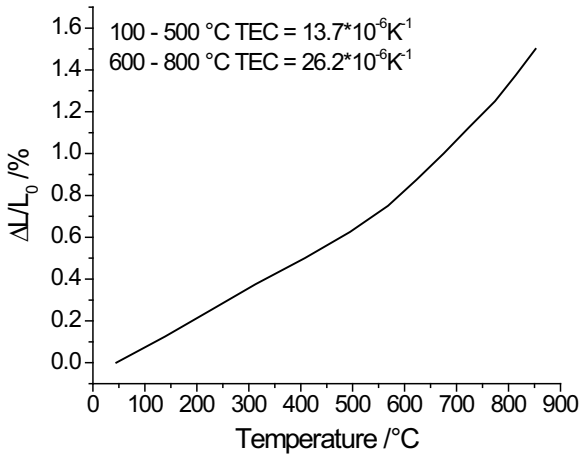

Figure 1.11: Thermal expansion behaviour of $La_{0.4}Sr_{0.6}Co_{0.2}Fe_{0.8}O_{3-\delta}$ in air [52]

The chemical expansion can be defined as $\varepsilon_c=\Delta a/a_0$, where $\Delta a=a-a_0$ is the change in the unit cell as a function of oxygen partial pressure at constant temperature. For example, the chemical expansion of $La_{0.6}Sr_{0.4}Fe_{0.2}Co_{0.8}O_{3-\delta}$ is given in Figure 1.12 in terms of the lattice constant.

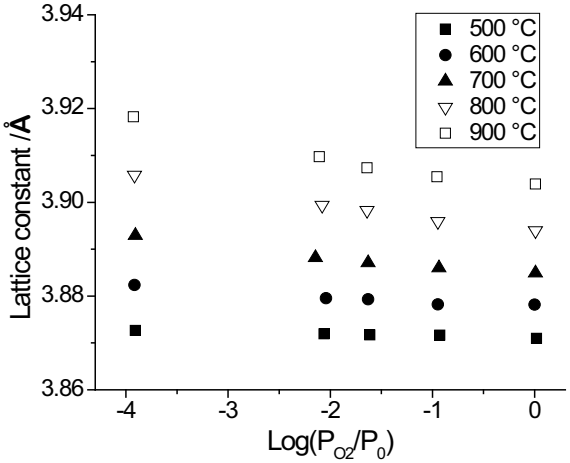

Figure 1.12: Lattice constant of $La_{0.6}Sr_{0.4}Fe_{0.2}Co_{0.8}O_{3-\delta}$ as a function of oxygen partial pressure (P_0 = 1 atm) [46]

In order to compare different materials the chemical expansion can be normalized by the change in oxygen deficiency, $\varepsilon_c/\Delta\delta$, where $\Delta\delta = \delta - \delta_0$ is the change in the oxygen deficiency from the reference state δ_0. Therefore, this parameter is taken as an indicator of how much the lattice expands per oxygen vacancy. However, the chemical expansion depends not only on $\Delta\delta$, but also on the composition of the materials. Table 1.3 compiles the chemical and normalized chemical expansion $\varepsilon_c/\Delta\delta$ for different MIEC materials. Although the overall thermal expansion of BSCF is higher than that of $La_xSr_{1-x}Co_yFe_{1-y}O_{3-\delta}$ [52, 90], the normalized chemical expansion of $La_xSr_{1-x}Co_yFe_{1-y}O_{3-\delta}$ is ~ 0.03 - 0.04, and is only ~ 0.012 for BSCF. Therefore, the higher TEC of BSCF is mainly due to the higher expansion related with lattice vibration. The lower value of $\varepsilon_c/\Delta\delta$ for BSCF may be caused by the higher oxygen deficiency, since 3-δ is about 2.51 at RT when cooled in air [91].

Table 1.3 Chemical expansions for different compositions

Composition	ε_c	$\Delta\delta$	$\varepsilon_c/\Delta\delta$	Temperature [°C]
$La_{0.5}Sr_{0.5}FeO_{3-\delta}$ [49]	0.0058	0.097	0.059	800
$La_{0.5}Sr_{0.5}Fe_{0.5}Co_{0.5}O_{3-\delta}$ [58]	0.0045	0.116	0.039	800
$La_{0.5}Sr_{0.5}Fe_{0.5}Co_{0.5}O_{3-\delta}$ [58]	0.0043	0.122	0.036	1000
$La_{0.5}Sr_{0.5}CoO_{3-\delta}$ [58]	0.0041	0.116	0.035	800
$La_{0.7}Ca_{0.3}CrO_{3-\delta}$ [92]	0.0036	0.101	0.036	1000
$La_{0.7}Ca_{0.3}Cr_{0.9}Al_{0.1}O_{3-\delta}$ [92]	0.0040	0.118	0.034	1000
$La_{0.6}Sr_{0.4}Fe_{0.2}Co_{0.8}O_{3-\delta}$ [46]	0.0039	0.180	0.022	800
$La_{0.3}Sr_{0.7}FeO_{3-\delta}$ [93]	0.0040	0.125	0.032	875
$La_{0.7}Sr_{0.3}Fe_{0.6}Ga_{0.4}O_{3-\delta}$ [93]	0.0015	0.035	0.044	875
$Ba_{0.5}Sr_{0.5}Co_{0.8}Fe_{0.2}O_{3-\delta}$ [91]	0.00038	0.05	0.008	500
	0.00152	0.14	0.011	700
	0.00244	0.19	0.013	850
	0.00296	0.24	0.012	1000

1.4 Spin transition

In perovskites the B cation is 6-fold coordinated with the oxygen anions, and located in the center of the cube, forming octahedral complexes BO_6 with 6 nearest oxygen ions. The spin transition of Co^{3+} in $LaCoO_3$ has been studied extensively since the 1950s [94-97]. As shown in Figure 1.13, the 5 orbitals in the 3d shell of Co^{3+} (d^6) are split by the crystal field into two groups: t_{2g} (3 orbitals) and e_g (2 orbitals). The energy of the t_{2g} orbitals is lower than that of the e_g orbitals. At very low temperature, the 6 electrons of Co^{3+} occupy the t_{2g} orbitals, and the e_g orbitals are empty. Since all electrons are paired, the spin of Co^{3+} is zero. With increasing temperature electrons can be thermally activated to e_g orbitals. Each electron has a half-spin, and depending on the number of unpaired electrons the spin of Co^{3+} can be 1 or 2. Some of non-magnetic Co^{3+} (LS, S=0) are thermally activated to magnetic Co^{3+} (IS, S=1 or HS, S=2). At about 200 °C the ratio of magnetic Co^{3+} is assumed to saturate [98].

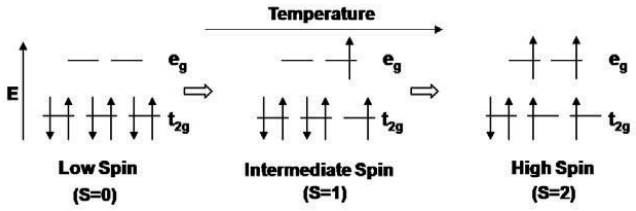

Figure 1.13: Schematic diagram of Co^{3+} spin transition in perovskites

1.5 Fracture stress, fracture toughness and Young's modulus

For structural application of the perovskite membranes in gas separation units their mechanical properties are of key importance. In addition to the functional performances, one of the challenges especially for industrial applications is to prevent the mechanical failure of the membranes. The mechanical integrity is challenged not only by exposure to elevated temperatures and thermal cycles but also to a large chemical gradient of oxygen [99-101]. Therefore, the knowledge of mechanical properties is essential for an estimation of structural

reliability of the membrane during heating/cooling and operation. Fracture stress, fracture toughness and Young's modulus are key mechanical properties to be known. Measured values of Young's modulus may include contributions of porosity, plastic deformation, roughness etc, which is normally called apparent Young's modulus. The apparent Young's modulus is hereafter also referred to as stiffness. In the present thesis Young's modulus and stiffness are both used subsequently without distinction. Data of facture stress, fracture toughness and Young's modulus are found in literature preferentially for La-containing perovskites. They are listed in table 1.4, table 1.5 and table 1.6 respectively.

Table 1.4 Fracture stresses of perovskite materials at various temperatures

Material	Fracture stress (MPa)	Test method
$LaFeO_3$	202 ± 18 (RT) 235 ± 38 (800 °C)	4-point bending [102]
$LaCoO_3$	53 (RT) ~ 50 (850 °C)	4-point bending [103]
	86 (RT) 109 ± 19 (800 °C)	4-point bending [104]
$La_{0.8}Ca_{0.2}CoO_3$	98(RT) 91 ± 4 (800 °C)	4-point bending [104]
$La_{0.5}Sr_{0.5}CoO_{3-\delta}$	138 ± 12 (RT) 181 ± 18 (800 °C)	4-point bending [99]
$La_{0.5}Sr_{0.5}Fe_{0.5}Co_{0.5}O_{3-\delta}$	128 ± 12 (RT) 166 ± 15(800 °C) 181 ± 23(1000 °C)	4-point bending [99]
$La_{0.5}Sr_{0.5}Fe_{0.25}Co_{0.75}O_{3-\delta}$	71 ± 7(RT) 61 ± 20(400 °C)	4-point bending [99]

	121 ± 11(600 °C) 120 ± 11(800 °C)	
$La_{0.8}Sr_{0.2}CoO_{3-\delta}$	76 (RT) 57 (850 °C)	4-point bending [103]
$La_{0.8}Sr_{0.2}Fe_{0.8}Co_{0.2}O_{3-\delta}$	165 (RT)	Biaxial [105]
$La_{0.6}Sr_{0.4}Fe_{0.8}Co_{0.2}O_{3-\delta}$	155 (RT)	Biaxial [105]
$La_{0.4}Sr_{0.6}Fe_{0.8}Co_{0.2}O_{3-\delta}$	50 (RT)	Biaxial [105]
$La_{0.2}Sr_{0.8}Fe_{0.8}Co_{0.2}O_{3-\delta}$	40 (RT)	Biaxial [105]
$La_{0.8}Sr_{0.2}CrO_{3-\delta}$	49 (RT) 67 (800 °C)	Biaxial [101]
$La_{0.7}Sr_{0.3}O_{3-\delta}$	234 (RT)	3-point bending [106]
$La_{0.8}Ca_{0.2}CoO_{3-\delta}$	150 (RT) ~ 63 (850 °C)	4-point bending [103]
$La_{0.75}Ca_{0.25}CrO_{3-\delta}$	122 ± 26 (RT) ~ 60 (800 °C)	4-point bending [107]
$La_{0.7}Ca_{0.3}CrO_{3-\delta}$	256 (RT)	3-point bending [106]
$La_{0.2}Sr_{0.8}Cr_{0.2}Fe_{0.8}O_{3-\delta}$	340 (RT) 113 (1000 °C)	C-ring [108]
$La_{0.6}Sr_{0.4}Cr_{0.2}Fe_{0.8}O_{3-\delta}$	138 (RT)	Biaxial [109]
$La_{0.7}Sr_{0.3}Cr_{0.8}Fe_{0.2}O_{3-\delta}$	230 (RT)	4-point bending [110]
$La_{0.8}Sr_{0.2}Cr_{0.2}Fe_{0.8}O_{3-\delta}$	243 (RT)	Biaxial [109]
$La_{0.5}Sr_{0.5}MnO_{3-\delta}$	78 (RT) 59 (200 °C) 109 (400 °C) 171 (600 °C) 188 (700 °C) 200 (800 °C)	4-point bending [111]
$La_{0.875}Sr_{0.125}MnO_{3-\delta}$	164 (RT) 109 (400 °C)	3-point bending [112]

	150 (800 °C) 222 (1000 °C)	
$La_{0.5}Sr_{0.5}Mn_{0.96}Co_{0.04}O_{3-\delta}$	38 (RT) 59 (300 °C) 142 (450 °C) 115 (600 °C) 115 (750 °C)	4-point bending [111]
$LaCr_{0.9}Mg_{0.1}O_3$	140 (RT) 247 (125 °C) 87 (1000 °C)	4-point bending [113]
$La_{0.9}Sr_{0.1}Ga_{0.8}Mg_{0.2}O_{3-\delta}$	162 ± 14 (RT) 55 ± 11 (900 °C)	Biaxial [114]
$La_{0.8}Sr_{0.2}Ga_{0.85}Mg_{0.15}O_{3-\delta}$	139 ± 17 (RT)	3-point bending [115]
$La_{0.8}Sr_{0.2}Cr_{0.97}V_{0.03}O_{3-\delta}$	62 ± 5 (RT)	4-point bending [61]
$LaCr_{0.79}Mg_{0.05}Al_{0.16}O_{3-\delta}$	148 ± 10 (RT)	4-point bending [61]
$SrCe_{0.95}Yb_{0.05}O_3$	171 ± 7	3-point bending [116]

The review was mainly focused on La-doped perovskites due to the lack of the data of Ba-doped perovskites. Regarding the fracture stress, some trends can be extracted from the data, although caution is advised with respect to the failure causing defects from different preparation sources. The fracture stress of $LaFeO_3$ is 202 ± 18 MPa at RT, but increases to 235 ± 38 MPa at 800 °C [102]. The replacement of Fe by Co reduces the fracture stress significantly. The fracture stress of $LaCoO_3$ is 86 MPa at RT and 109 ± 19 MPa at 800 °C, respectively [104]. The fracture stress of $La_{0.8}Ca_{0.2}CoO_3$ is 98 MPa at RT and 91 ± 4 MPa at 800 °C, which means that the effect of Ca is similar to that of Co. However, the replacement of 50 % La with Sr increases the fracture stress to 138 ± 12 MPa at RT and 181 ± 18 MPa at 800 °C respectively [99]. For the $La_{1-x}Sr_xFe_{0.8}Co_{0.2}O_3$ system, when x increases from 0.2 to 0.4, the fracture stress decreases slightly from 165 MPa to 155 MPa, and by further increasing x to

0.6 the fracture stress decreases abruptly to 50 MPa [105]. Despite the variations with composition it is interesting that obviously higher fracture stresses at 800 °C compared to RT are not unusual.

Table 1.5 Fracture toughness of perovskite materials at various temperatures

Material	K_{IC} [MPa·m$^{0.5}$]	Test method
$LaFeO_3$	2.5 (RT) 2.2 (400 °C) 3.1 (800 °C)	Single edge notched beam (SENB) [102]
$LaCoO_3$	1.23 ± 0.06 (RT) 1.2 ± 0.11(150 °C) 1.1 ± 0.05 (200 °C) 0.95 ± 0.06 (400 °C) 1.05 ± 0.04 (700 °C) 1.05 ± 0.15 (800 °C)	Single edge V notch beam (SEVNB) [104]
$La_{0.8}Ca_{0.2}CoO_3$	2.2 (RT) 1.0 (800 °C)	SEVNB [66]
$La_{0.5}Sr_{0.5}CoO_3$	1.5 ± 0.3 (RT) 2.9 ± 0.4 (800 °C)	SENB [99]
$La_{0.5}Sr_{0.5}Fe_{0.5}Co_{0.5}O_3$	1.2 ± 0.1 (RT) 1.5 ± 0.2 (800 °C) 2.3 ± 0.2 (1000 °C)	SEVNB [99]
$La_{0.9}Sr_{0.1}Ga_{0.8}Mg_{0.2}O_3$	2.1 (RT) 0.75 (600 °C)	SENB [117]
$LaCr_{0.9}Mg_{0.1}O_3$	2.8 (RT) 3.9 (125 °C) 1.9 (1000 °C)	SENB [113]
$La_{0.8}Ca_{0.2}CoO_3$	1.92 (RT) 1.5 ± 0.4 (150 °C)	SEVNB [104]

	1.2 ± 0.1 (200 °C) 0.78 ± 0.3 (400 °C) 0.78 ± 0.1 (550 °C) 1.0 ± 0.2 (700 °C) 1.14 ± 0.2 (800 °C)	
$BaZrO_3$	1.5 (RT)	Indentation [118]

The fracture toughness values of $LaFeO_3$ appear stable from RT to 400 °C (Figure 1.14), and increase slightly at 800 °C [102]. The fracture toughness of $LaCoO_3$ maintains a relatively stable value from RT up to 800 °C [104]. Similar to fracture stress, the fracture toughness of $LaFeO_3$ is much higher than that of $LaCoO_3$. The fracture toughness of $La_{0.5}Sr_{0.5}Fe_{0.5}Co_{0.5}O_3$ increases at high temperatures maybe due to creep effects [99]. Interestingly, the fracture toughness of $La_{0.8}Ca_{0.2}CoO_3$ decreases rapidly from RT to 400 °C, and thereafter recovers slightly up to 800 °C [104]. This anomaly is attributed to a spin transition of Co^{3+} in the lattice [104].

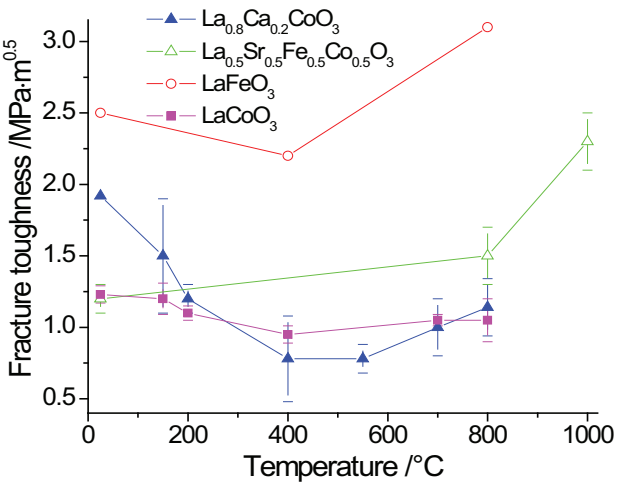

Figure 1.14: Fracture toughness of perovskites as a function of temperature

Table 1.6 Young's modulus of perovskite materials at various temperatures

Material	Young's modulus (GPa)	Test method
$LaFeO_3$	213 ± 14 (RT) 206 ± 24 (800 °C)	4-point bending [102]
$La_{0.5}Sr_{0.5}Fe_{0.5}Co_{0.5}O_3$	131 ± 1 (RT) 130 ± 1 (800 °C)	Resonant ultrasound spectroscopy [99]
$La_{0.5}Sr_{0.5}CoO_3$	135 ± 1 (RT) 135 (800 °C) 126 (1000 °C)	Resonant ultrasound spectroscopy [99]
$LaCoO_3$	83 ± 3 (RT)	4-point bending [103]
$La_{0.8}Sr_{0.2}CoO_3$	86 ± 13 (RT)	4-point bending [103]
$La_{0.8}Ca_{0.2}CoO_3$	112 ± 3 (RT)	4-point bending [103]
$La_{0.8}Sr_{0.2}Fe_{0.8}Co_{0.2}O_3$	161 ± 2 (RT)	Ultrasonic [105]
$La_{0.6}Sr_{0.4}Fe_{0.8}Co_{0.2}O_3$	152 ± 3 (RT)	Ultrasonic [105]
$La_{0.4}Sr_{0.6}Fe_{0.8}Co_{0.2}O_3$	167 ± 9 (RT)	Ultrasonic [105]
$La_{0.2}Sr_{0.8}Fe_{0.8}Co_{0.2}O_3$	188 ± 6 (RT)	Ultrasonic [105]
$BaZrO_3$	240.5 (RT) 239.5 (280 °C) 237.7 (480 °C) 235.9 (650 °C) 228.6 (835 °C) 215.5 (1015 °C)	Ultrasonic [119]
$SrHfO_3$	219.8 (RT)	ultrasonic pulse-echo [120]
$La_{0.8}Sr_{0.2}Fe_{0.7}Ga_{0.3}O_{3-\delta}$	120 (RT) 85 (200 °C) 86 (400 °C) 90 (600 °C) 95 (800 °C)	ultrasonic pulse-echo [121]

	92 (1000 °C)	
$La_{0.8}Sr_{0.2}FeO_{3-\delta}$	170 (RT) 155 (200 °C) 110 (340 °C) 120 (600 °C) 130 (800 °C) 127 (1000 °C)	ultrasonic pulse-echo [121]

The Young's modulus of $LaFeO_3$ is 213 ± 14 GPa at RT [102]. The replacement of Fe with Co decreases the Young's modulus strongly, and the value is only 83 ± 3 GPa for $LaCoO_3$ [103]. The replacement of La with 20 % Sr does not affect the Young's modulus, and the value of Young's modulus is 86 ± 13 GPa for $La_{0.8}Sr_{0.2}CoO_3$, while the replacement of La with 20 % Ca enhances the Young's modulus dramatically, and Young's modulus of $La_{0.8}Ca_{0.2}CoO_3$ becomes 112 ± 3 GPa [103]. With further replacement of Sr, Young's modulus of $La_{0.5}Sr_{0.5}CoO_3$ increases strongly to 135 ± 1 GPa [99].

The Young's modulus of $BaZrO_3$ is about 240 GPa at RT [119], and behaves like 'normal' ceramics, i.e. decreases slightly with temperature [122]. An anomaly of Young's modulus is observed for $La_{0.8}Sr_{0.2}FeO_3$ and $La_{0.8}Sr_{0.2}Fe_{0.7}Ga_{0.3}O_3$. The Young's modulus of $La_{0.8}Sr_{0.2}FeO_3$ decreases rapidly from RT to 340 °C, and rises slowly up to 800 °C (Figure 1.15).

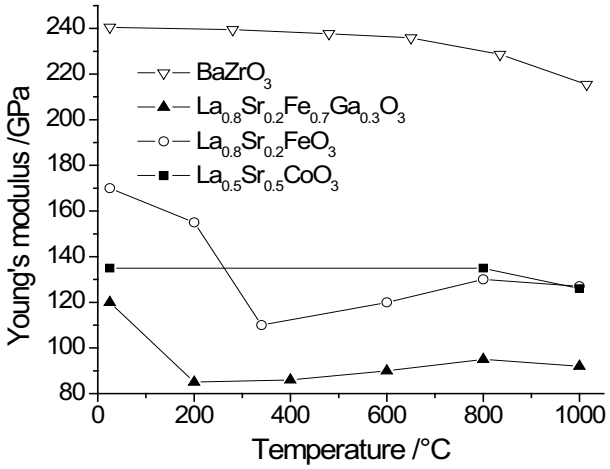

Figure 1.15: Dependence of Young's modulus of perovskite materials on temperature

In conclusion, the review of the published mechanical data reveals that chemically similar perovskites may exhibit totally different mechanical properties. The complexity of the fracture stress, fracture toughness and Young's modulus results presented above as a function of temperature does not allow predictions regarding mechanical behaviour in the case of the three membrane materials. The obvious need to characterize the mechanical properties of these three OTM materials individually was followed in the present thesis.

1.6 Creep

Creep is a plastic deformation process under a fixed stress at an elevated temperature. Normally the temperature is greater than 0.4 T_m (absolute melting temperature), and the stress is lower than the yield strength of the material. Consequently creep is prominent in materials that are subjected to high temperature for long terms. The strain rate increases as the temperature is raised [123-125]. In general, creep can be described by three different stages: primary, secondary and tertiary creep (Figure 1.16) [126].

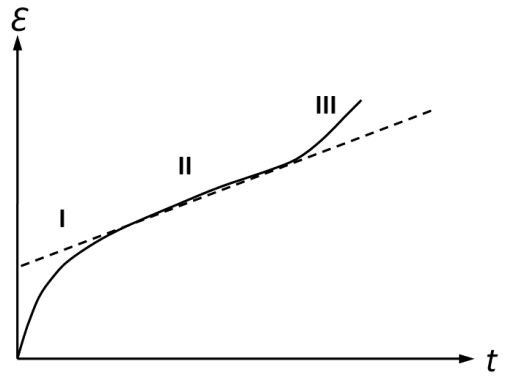

(a) Three stages of creep in tension. I) primary II) secondary III) tertiary

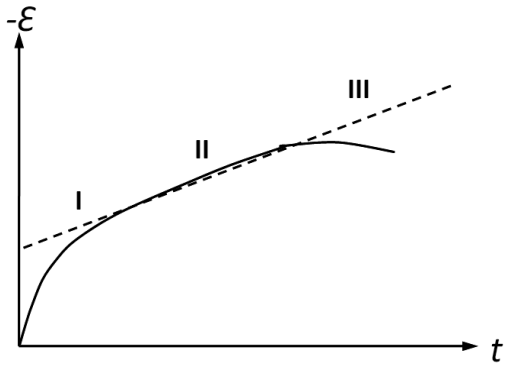

(b) Three stages of creep in compression. I) primary II) secondary III) tertiary

Figure 1.16: Schematic representation of creep behaviour

In the primary creep, the strain rate is relatively high, but slows down with increasing strain due to work hardening. When work hardening and thermal softening reach a balance, the strain rate reaches a stable value. This stage is called secondary or steady-state creep, and the strain rate of creep usually refers to the rate in this stage. In the tertiary stage, the strain rate exponentially increases with the strain, which ultimately leads to failure of the sample.

For many ceramics the creep rate in the steady-state region can be given by the equation [127]:

$$\frac{d\varepsilon}{dt} = A(\frac{1}{d})^{p}(P_{O_2})^{m}\sigma^{n}\exp(-\frac{E_a}{RT}) \qquad (1.8)$$

where $\frac{d\varepsilon}{dt}$ is the steady-state creep rate, A is a constant, d is the grain size, p is the inverse grain size exponent, P_{O2} is the partial pressure of oxygen, m is the oxygen partial pressure exponent, σ is the applied stress, n is the stress exponent, E_a is the activation energy, R is the gas constant and T is the absolute temperature.

P_{O2}, σ and T are external testing conditions that can be controlled. The parameters p, m, n and E_a have to be extracted from experiments. They are commonly considered as being characteristic values, but may also change due to the external conditions.

The creep mechanisms which govern equation (1.8) depend on material, temperature, applied stress and atmosphere. Strain can be achieved by lattice diffusion, grain boundary diffusion, movement of dislocations, or grain boundary sliding accommodated with diffusion, and normally several or all mechanisms contribute to the creep. But also one mechanism may dominate the creep depending on temperature, applied stress and atmosphere. If the creep is mainly governed by lattice diffusion (Nabarro-Herring creep), then the grain size dependence should be p=2 [124]. If the creep mainly occurs by grain boundary diffusion (Coble creep), p=3 can be expected [123].

The OTM membranes are operated at high temperature under stress and in a chemical gradient. Moreover in industrial application, the membrane must maintain structural stability over a long period of operation. Therefore, creep is of crucial importance for estimating the structural stability of the membrane materials.

Table 1.7 displays compressive creep rates for different materials at 1200 °C in air and at 5 MPa load. Although this temperature is significantly higher than that in membrane application, some trends can be deduced from the data. For the La-Sr-Fe-Co systems the increase of Sr and Co seems to increase the creep rate, which is consistent with the influence of the two elements on oxygen deficiency.

Table 1.7 Creep rates at 1200 °C in air and 5 MPa load for different compositions

Composition	Creep rate [s^{-1}]	Grain size [μm]
$SrFeO_{3-\delta}$, 5% A excess [128]	$4 \cdot 10^{-6}$	<5
$SrFeO_{3-\delta}$, 5% B excess [128]	$3 \cdot 10^{-6}$	<5
$BaTiO_3$ [129]	$6 \cdot 10^{-6}$	19.3
$La_{0.9}Sr_{0.1}MnO_3$ [130]	$1 \cdot 10^{-6}$	5
$La_{0.9}Sr_{0.1}Ga_{0.8}Mg_{0.2}O_3$ [131]	$1 \cdot 10^{-8}$	19.6
$(La_{0.9}Sr_{0.1})_{0.98}Ga_{0.8}Mg_{0.2}O_3$ [131]	$4 \cdot 10^{-9}$	16.2
$(La_{0.9}Sr_{0.1})_{0.95}Ga_{0.8}Mg_{0.2}O_3$ [131]	$3 \cdot 10^{-9}$	21.2
$La_{0.8}Sr_{0.2}Ga_{0.85}Mg_{0.15}O_3$ [132]	$2 \cdot 10^{-7}$	8
$La_{0.5}Sr_{0.5}Fe_{0.5}Co_{0.5}O_3$ [133]	$3 \cdot 10^{-6}$	1.1
$La_{0.5}Sr_{0.5}CoO_{3-\delta}$ [133]	$4 \cdot 10^{-5}$	1.7
$SrCo_{0.8}Fe_{0.2}O_{3-\delta}$ [134]	$9 \cdot 10^{-3}$	2.4
$La_{0.2}Sr_{0.8}Fe_{0.8}Cr_{0.2}O_{3-\delta}$ [135]	$6 \cdot 10^{-6}$	3.2

The activation energy, E_a in equation (1.8) can be calculated from the linear regression of a plot of $\ln^{\text{creep rate}}$ versus inverse temperature at constant load. The activation energy of creep was reported to vary from 112 to 837 $kJ \cdot mol^{-1}$ [128-130, 134-139], while the activation energy for oxygen diffusion in the same perovskites is 50 - 170 $kJ \cdot mol^{-1}$ [33, 37, 140-142]. Therefore, the creep rate appears to be determined by the diffusion of cations.

2. Experiments

The experiments in the present work were conducted to obtain primary results on the thermo-mechanical and structural behaviour of disc-shaped BSCF and LSCF specimens as well as rectangular LNO bars. The fracture stress was mechanically determined applying ring-on-ring and 4 point bending tests. The fracture toughness was derived from the length of the indentation cracks. Micro-structural properties were accessed by scanning electron microscopy (SEM) and transmission electron microscopy (TEM). The TEM foils were prepared by the focused ion beam (FIB) method. Phase analyses by X-ray diffraction (XRD) and measurements of thermal expansion coefficient (TEC) by optical dilatometer complemented the investigations. The steady-state creep rate of LSCF was measured in air and vacuum (10^{-5} mbar) in the temperature range of 650 – 950 °C.

2.1 BSCF and LSCF perovskites

The $Ba_{0.5}Sr_{0.5}Co_{0.8}Fe_{0.2}O_{3-\delta}$ (BSCF) and $La_{0.58}Sr_{0.4}Co_{0.2}Fe_{0.8}O_{3-\delta}$ (LSCF) samples were produced by IEF-1, Forschungszentrum Jülich GmbH. They had a similar disc-shaped geometry but were prepared from different powder sources. The BSCF powders, supplied by Treibacher Industrie AG, Austria, were uniaxially pressed with a pressure of 105 MPa and sintered at 1000 °C for 12 hours. The heating rate was 5 K/min and the cooling rate 0.5 K/min. The Archimedes density of the as-received samples was determined to be 5.37 g/cm^3 with a porosity of 4.5 %. Assuming a spherical geometry the average grain size of the equivalent diameter was 10.1 ± 4.3 µm.

The LSCF powders were synthesized by a spray-drying technique using aqueous solutions of appropriate quantities of nitrate salts [143]. The powders were uniaxially pressed with a pressure of 120 MPa and sintered at 1200 °C for 3 hours. The heating rate and cooling rate were both 0.5 K/min. The Archimedes' density of the as-received samples was determined to

be 5.81 g/cm^3 with a porosity of 6 %. The average grain size of the equivalent diameter was 0.6 ± 0.2 µm.

2.1.1 Ring-on-ring tests

The ring-on-ring test has been used extensively for fracture stress measurements on brittle materials, which can eliminate the edge effects compared to bending bars [144, 145]. The ring-on-ring test is schematically displayed in Figure 2.1.

(a) Overview

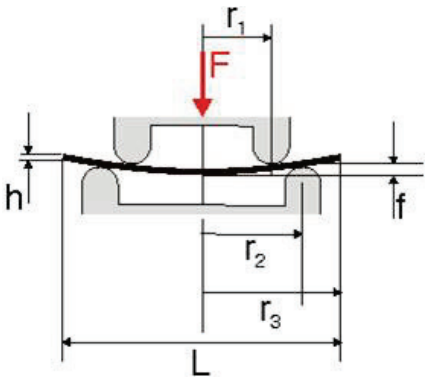

(b) Cross section

Figure 2.1: Schematic representation of ring-on-ring test

Since the disc-shaped samples were not completely flat and also possessed large surface defects, they were ground (P2500 abrasive) before being loaded in biaxial ring-on-ring bending tests. The test conditions followed the procedures recommended in the ASTM standard C 1499-05 [146]. The data were evaluated using the equations for linear bending theory. Accordingly, the equibiaxial flexure stress was derived from:

$$\sigma = \frac{3P}{2\pi \cdot t_h^2}\left[(1+\nu)\ln(\frac{R_2}{R_1}) + \frac{1-\nu}{2}(\frac{R_2^2 - R_1^2}{R_3^2})\right] \quad (2.1)$$

where P is the applied force, t_h is the specimen thickness, ν the Poisson ratio and R_1, R_2 and R_3 are the radii of the loading ring, supporting ring and (circular) specimen, respectively. The values of t_h, R_1, R_2 and R_3 were 1.1 mm, 9.0 mm, 18.6 mm and 21.8 mm, respectively. Since the number of tests was limited, only the mean value and the standard deviation are given. The apparent elastic modulus was calculated using [147]:

$$E = \frac{3\left(1-\nu^2\right)\cdot R_1^2 \cdot \Delta P}{2\pi \cdot \Delta d_e \cdot t_h^3}\cdot\left[\left(\frac{R_2}{R_1}\right)^2 - 1 - \ln\left(\frac{R_2}{R_1}\right) + \frac{1}{2}\left(\frac{1-\nu}{1+\nu}\right)\cdot\left(\frac{\left(R_2^2 - R_1^2\right)^2}{R_2^2 R_3^2}\right)\right] \quad (2.2)$$

where d_e is the central deflection of the specimen, and the other parameters are the same as in equation (2.1).

At each temperature 5 specimens were tested to obtain fracture stress at selected temperatures between RT and 800 °C. For the tests at elevated temperatures, a heating rate of 2 K/min was used, and a dwell time of 1 hour was chosen before testing. The ring-on-ring tests were carried out with a universal mechanical testing machine (Instron 1362). The central displacement of the specimen was recorded with a sensor that contacted the lower surface of the sample. The loading rate was 100 N/min in all tests. The stiffness was determined from the linear part of the load-displacement curve in a stress range of 15 - 25 MPa.

2.1.2 Micro-indentation

The principle of instrumented indentation testing is to measure the force that has to be applied to a diamond tip as a function of penetration depth for both loading and unloading process. Depth-sensitive indentation is now widely used for measuring local mechanical properties of thin films and materials of small volume. Besides conventional hardness determination, mechanical properties, such as Young's modulus, fracture toughness, and residual stresses, can

also be extracted from indentation tests. Although there are different tip geometries, only the Vickers indenter will be discussed, since it was exclusively used in the present work.

The Vickers indenter has pyramid-shaped tip with four sides and an angle of 136 ° between two opposite sides. Typical load-displacement curves of a depth sensitive indentation test are shown in Figure 2.2.

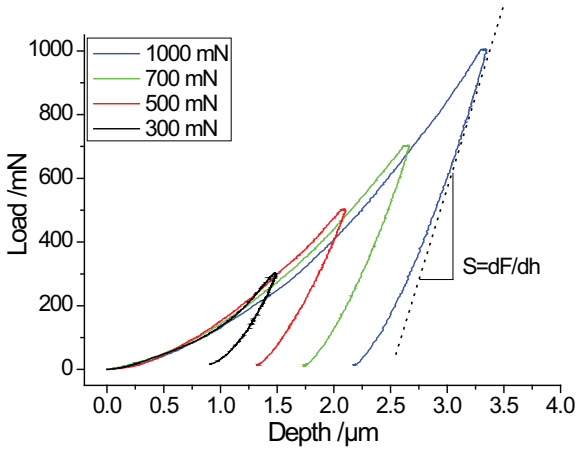

Figure 2.2: Typical load-displacement curves of indentation

The hardness H_{IT} can be derived as [148]:

$$H_{IT} = \frac{F_m}{A_p} \tag{2.3}$$

where F_m is the maximum load, A_p is the projection area of the impression. It should be noted that the physical meaning of hardness is not well defined. Hardness is an integral property of elastic deformation, plastic deformation, and resistance to crack propagation.

The calculation of Young's modulus is based on [148]:

$$E_{IT} = \frac{(1-v_s^2)}{\frac{1}{E_r} - \frac{(1-v_i^2)}{E_i}} \qquad E_r = \frac{\sqrt{\pi}}{2\beta}\frac{S}{\sqrt{A_p}} \qquad (2.4)$$

where E_{IT} indentation elastic modulus, v_s poisson's ratio of sample, v_i poisson's ratio of indenter, E_r reduced modulus, E_i elastic modulus of indenter, β indenter constant. S is given in Figure 2.1.

A permanent impression in the material will be left after indentation (Figure 2.3), and if the load is sufficiently high, four cracks are generated along the four edges of the impression. For the brittle materials the indentation fracture toughness K_{Ind} can be estimated by simply measuring the crack length and using the relationship [149, 150]:

$$K_{Ind} = \kappa_r \frac{F_m}{c^{3/2}} \qquad (2.5)$$

where c is the crack length. The parameter κ_r is related to the elastic/plastic behaviour and is given by $\kappa_r = \kappa(E/H)^{1/2}$. Following the Oliver and Pharr procedure [148], hardness H and stiffness E can be evaluated from the indentation load-penetration curve and hence the ratio of E/H can be determined. Note that Equation (2.5) was not derived from first principles, thus the constant κ=0.016 had to be adjusted by calibrating indentation toughness results with those of standard macroscopic tests [149, 150].

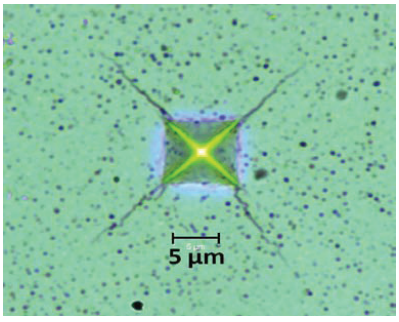

(a) Optical microscopy image of indentation impression

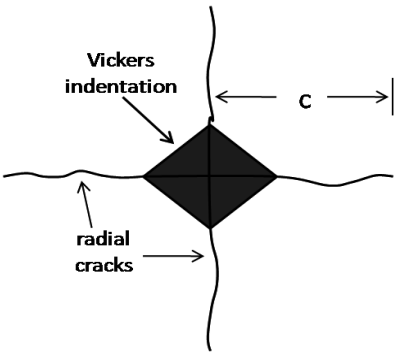

(b) Schematic indentation impression

Figure 2.3: Impression of indentation

In addition to the global ring-on-ring test for fracture stress and stiffness measurement, depth-sensitive micro-indentation was used to determine hardness, Young's modulus, and the indentation fracture toughness [149, 150]. The indentation fracture toughness was calculated applying equation (2.5). The length of the indentation cracks was measured using the optical microscope of the indentation system (CSM: Coating and Surface Measurement, CH). The indentation fracture toughness was determined from RT to ~ 350 °C, which is the maximum temperature that could be reached using the heating stage.

In real application, the membranes are operated under an oxygen gradient. In order to imitate this condition, disk-shaped samples of BSCF and LSCF were annealed at 900 °C for 2 hours under a gradient of oxygen. In this dual atmosphere experiments one surface of the sample was exposed to air, and the other surface exposed to vacuum (2 mbar). After annealing the sample was cooled to RT with a slow rate of 0.5 K/min to exclude thermal stresses induced by sharp temperature gradients. At RT micro-mechanical properties were measured with indentation on polished cross sections of the specimens.

2.1.3 X-ray diffraction

The lattice structure was examined by X-ray diffraction analysis (Siemens Diffractometer D5000) with a step scan using CuKα radiation, operated at 40 kV and 40 mA. The step size and

step time were 0.02 °/step and 10 s, respectively. The quantity of phase compositions was analyzed with Rietveld refinement from the XRD data. Complementary in-situ high-temperature XRD measurements were carried out with a high temperature stage (HTK S1).

2.1.4 Thermal property characterization

The linear thermal expansion coefficient (TEC) was continuously measured using an optical dilatometer (Misura, Expert System Solutions S.r.l. Italia) in the temperature range from room temperature (RT) up to 900 °C. Tubular samples supplied by HITK (length 50.1 mm, diameter 14.8 mm, thickness 1.1 mm) were used. The heating rate was 1 K/min. Differential thermal analysis (DTA) and thermogravimetry (TG) (STA 449C Jupiter Netzsch) were performed in air with a heating rate of 2 K/min. Young's modulus was also measured with a resonance method (Grindsonic) from RT up to 900 °C.

2.1.5 Transmission electron microscopy

The domain structure of LSCF was observed with a scanning electron microscope (SEM, LEO1530, Zeiss, Germany) and a transmission electron microscope (TEM, Philips CM200). The slip lines around impressions of BSCF were studied with an optical microscope and TEM. The TEM specimens of the BSCF and LSCF perovskites were prepared by focused ion beam (FIB, LEO1540, Zeiss) cutting. The magnetic characteristics and the temperature dependence of susceptibility were measured with a Quantum Design PPMS with heating stage using a rate of 2 K/min.

2.1.6 Creep tests

Compressive creep tests were performed in air and vacuum (10^{-5} mbar) in the temperature range of 700 – 950 °C. Tubular samples of LSCF were mounted between two Al_2O_3 push rods. A preload of ~ 0.3 MPa was applied during heating to ensure good contact between the sample and the push rods, and at creep temperatures the same load was kept for ~ 20 h to reach

equilibrium and to remove the roughness of the contact surfaces. Applying a constant load of 30 MPa the measurements lasted up to 24 h.

2.2 Experiments with $La_2NiO_{4+\delta}$ (LNO)

The samples were prepared from spray pyrolysis powders and sintered at 1400 °C in air with a cellulose based pore former to obtain a membrane material with a defined pore structure. The specimens were extruded in a rectangular shape with 6 hollow internal compartments (Figure 2.4).

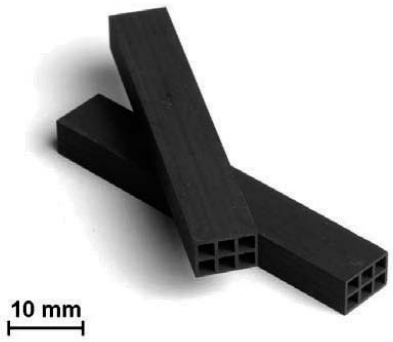

(a) Photo of the LNO samples

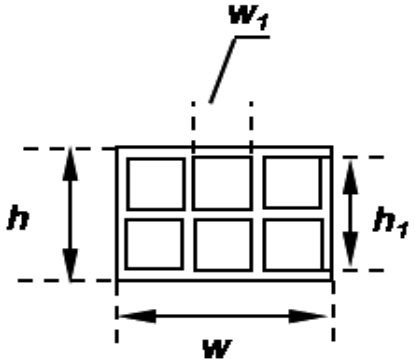

(b) Cross section of the LNO sample

Figure 2.4: Investigated LNO samples

2.2.1 Four point bending tests

The stiffness and fracture stress were determined based on data obtained using 4-point bending test with a universal mechanical testing machine (Instron 1362). The tests were carried out from RT up to 900 °C. For tests at elevated temperatures a heating rate of 4 K/min was chosen, and before testing a dwell time of 1 hour was chosen to reach thermal equilibrium. In all tests the load rate was 50 N/min. The stiffness was determined from the load - displacement curve. It was assumed that failure started from the surface of the specimens under the highest stress.

The bending moment of inertia of the sample was derived from:

$$I = \frac{wh^3}{12} - 3\frac{w_1 h_1^3}{12} \tag{2.6}$$

where w is the width, h is the height, h_1 is height of 2 compartments, and w_1 is the width of a compartment (Figure 2.3 (b)). The values of w, h, h_1 and w_1 were 8.4 mm, 5.7 mm, 4.7 mm and 2.1 mm, respectively. The moment of inertia of the central layer was neglected, since the moment of inertia is proportional to the cubic distance from the central axis of the composite. The moment in the experiments was derived:

$$M = \frac{P}{2}\frac{(L_s - l_s)}{2} \tag{2.7}$$

where P is the applied force, L_s (40 mm) is support pin distance, l_s (20 mm) is load pin distance. The fracture stress was determined using:

$$\sigma = \frac{M}{I}\frac{h}{2} \tag{2.8}$$

The Young's modulus was calculated:

$$E = \frac{Ml_s^2}{2Id_e} \tag{2.9}$$

where d_e is the central deflection of the specimen.

2.2.2 Complementary characterizations

Similar to the perovskite materials, the LNO bars were also additionally characterized with respect to structural and thermal properties. The lattice structure was characterized by X-ray diffraction analysis (Diffractometer Siemens D5000) with a step scan using CuKα radiation. The linear thermal expansion coefficient (TEC) was measured by using a differential dilatometer (Misura, Expert System Solutions S.r.l. Italia) in the temperature range from RT up to 1000 °C. The heating rate in the measurements was 1 K/min. Differential thermal analysis (DTA) and thermogravimetry (TG) (STA 449C Jupiter Netzsch) were carried out in air with a heating rate of 1 K/min.

3. Results and discussion

In this section, the thermo-mechanical results of BSCF, LSCF and LNO are presented and discussed sequentially. Macro-mechanical behavior measured with ring-on-ring test (for LSCF and BSCF) and 4 point bending test (for LNO) as well as micro-mechanical properties determined from indentation tests are presented. The various characterization results are discussed to explain the mechanical behavior. Particular focus is directed to the anomaly of Young's modulus observed in BSCF. The effect is attributed to the spin transition of Co^{3+}. This transition is confirmed by measurements of magnetic susceptibility.

3.1 BSCF

Operation of the membranes in real components requires mechanical integrity not only under steady state condition but also during thermal cycling. However, knowledge on the thermo-mechanical properties of BSCF is limited. In the subsequent sections, the thermo-mechanical behaviour of disk-shaped BSCF specimens is evaluated.

3.1.1 Young's modulus and fracture stress

The Young's modulus of BSCF was determined from a ring-on-ring bending test between RT and 800 °C in air and vacuum (10^{-5} mbar) (Figure 3.1.1). For measurements in vacuum, the as-received samples were heated to 900 °C, and annealed for 2 hours to reach the equilibrium in oxygen deficiency under vacuum. The Young's modulus values were measured during the cooling process for the first heating cycle and during heating or cooling for the subsequent heating cycles.

In air, a value of 63.3 ± 2.6 GPa was obtained at RT. With increasing temperature a sharp decrease in Young's modulus and a minimum at ~ 200 °C is observed. At higher temperature Young's modulus increases again significantly and reaches at 300 °C ~ 84 % of the RT value. Above 300 °C the temperature dependence of the Young's modulus of BSCF behaves as expected for ceramic materials, i.e. it decreases slightly with increasing temperature. The

temperature dependence of Young's modulus of polycrystalline ceramics, without grain boundary softening, is typically a decrease of about 1 % per 100 K [122]. After annealing in vacuum Young's modulus is 71.9 ± 1 GPa at RT, which is about 12 % higher than the value in air. The results are consistent with the values measured by indentation (see section 3.1.2). Under vacuum an even stronger decrease of Young's modulus is present form RT to 250 °C (Figure 3.1.1), and the value stays relatively stable until 500 °C, before increasing again up to 800 °C. The described anomaly of Young's modulus of BSCF is emphasized by comparison with the dotted line for ceramics with 'normal' behavior in Figure 3.1.1.

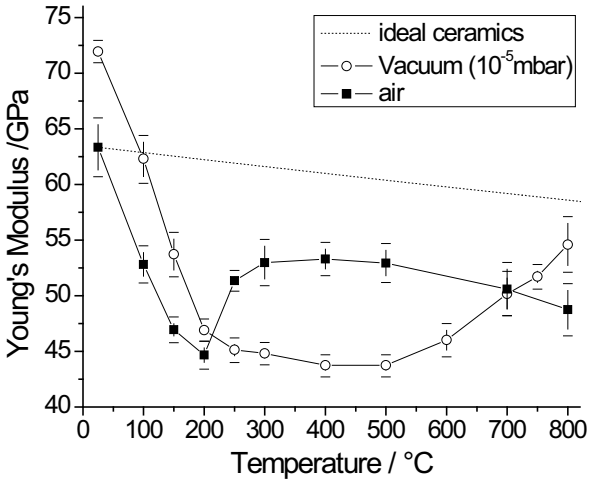

Figure 3.1.1: Young's modulus of BSCF measured in ring-on-ring bending test as a function of temperature and P_{O2} (air and 10^{-5} mbar). The Young's modulus expected for 'normal' ceramics (dotted line) is displayed for comparison.

The Young's modulus was also measured by a dynamic impulse excitation method in the temperature range RT ~ 900 °C in air (Figure 3.1.2). The dynamic Young's modulus determined during heating and cooling show a certain shift against the values obtained in bending tests, but agree qualitatively well with respect to the presence of a minimum at ~ 200 °C.

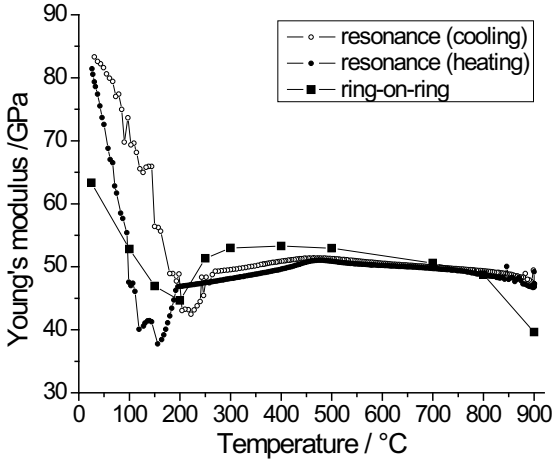

Figure 3.1.2: Young's modulus measured with ring-on-ring test and dynamic resonance frequency method in air (data provided by IMCE, Belgium)

The fracture stress was measured with ring-on-ring tests at selected temperatures in the range RT to 800 °C in air (Figure 3.1.3). Similar to Young's modulus, the fracture stress decreases sharply to a minimum between 200 °C and 400 °C, followed by an increase up to 800 °C.

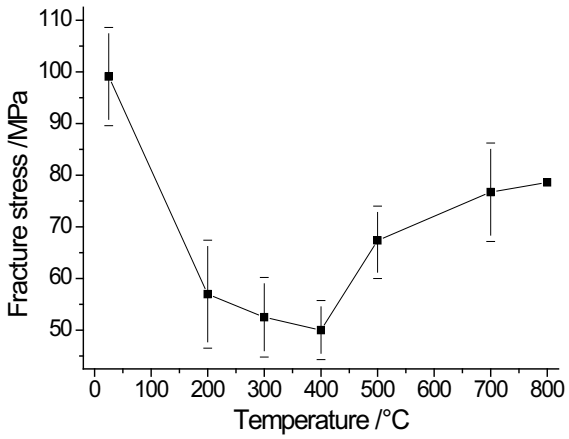

Figure 3.1.3: Fracture stress of BSCF measured with ring-on-ring bending test as a function of temperature in air

3.1.2 Indentation results

The micro-indentation tests using a Vickers tip are influenced by the porosity of the BSCF but basically show well defined impressions with cracks from the four corners. Figure 3.1.4 displays two magnifications of the same impression.

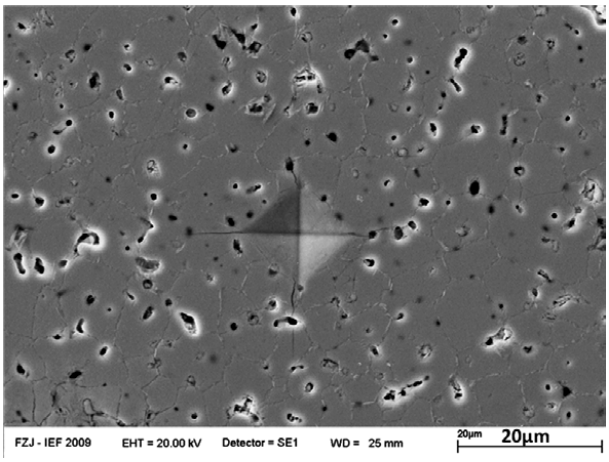

(a) SEM micrograph of BSCF with Vickers impression (600mN) and indentation cracks

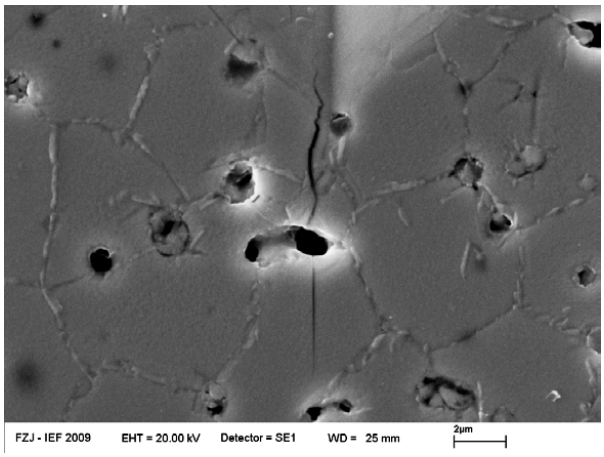

(b) Magnified bottom corner of the impression

Figure 3.1.4: Impression of indentation

Young's modulus and hardness of BSCF as determined from the load-displacement curves (equation (2.3) and (2.4)) in ambient atmosphere are shown in Figures 3.1.5 and 3.1.6. Both Young's modulus and hardness decrease slightly (~10 %) with increasing load. Note that

calibration test with BK-7 glass showed no load dependence. The decrease of hardness and Young's modulus with increasing indentation load is known as the indentation size effect (ISE) [151]. The ISE was observed in single crystals with different types of bonding (metallic, ionic, and covalent) [151, 152]. Many mechanisms have been proposed to explain the ISE. The ISE was related to surface effects [153], the strain gradient effects [154-156], the structural non-uniformity of the deformed volume [157], the change in the contribution of the elastic and plastic deformation at the indentation [151], the friction between the indenter and the sample [158, 159], etc. The variety of proposed mechanisms emphasizes the rather complicated nature of the ISE. Most of the mechanisms developed are based on a dislocation related origin of the ISE. Therefore, one could expect the presence of the ISE in crystalline solids, particularly in single crystals. However, in numerous investigations the ISE was also reported for poly-crystalline materials irrespective of the grain size [159, 160], nanocrystalline materials [161], amorphous solids and polymers [162]. The Young's modulus of a composite system depends on the volume fraction of each phase [163]. Although the dependence of Young's modulus and hardness on grain size is reported for nanocrystalline ceramic [164], the volume fraction of grain boundary for normal material (grain size >1 μm) is very small. The grain size of BSCF is 10.1 ± 4.3 μm, so the grain boundaries apparently do not contribute to the ISE. Here both the surface effect and the strain gradient effect are suggested to contribute the ISE [153-156].

In order to compare the indentation with the ring-on-ring bending results, the Young's modulus of the 1 N impression seems reasonable. Micro-indentation yielded a value of 72.0 ± 1.9 GPa at a load of 1000 mN for BSCF, while a value of 63.3 ± 2.6 GPa was obtained from ring-on-ring test. Since a larger volume is stressed in the bending test, the influence of larger defects on Young's modulus may explain the lower value.

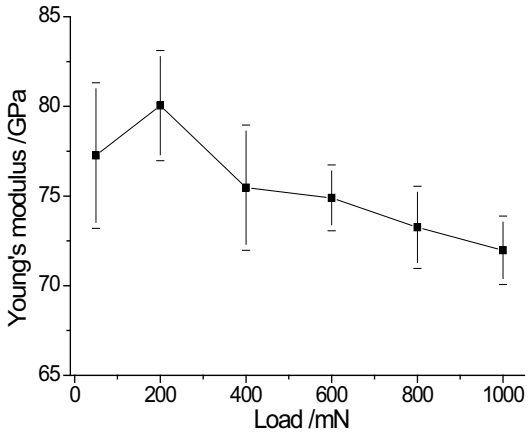

Figure 3.1.5: Young's modulus of BSCF measured by indentation as a function of loading force in ambient atmosphere. For each load 36 indentations were applied, and the standard deviation was given.

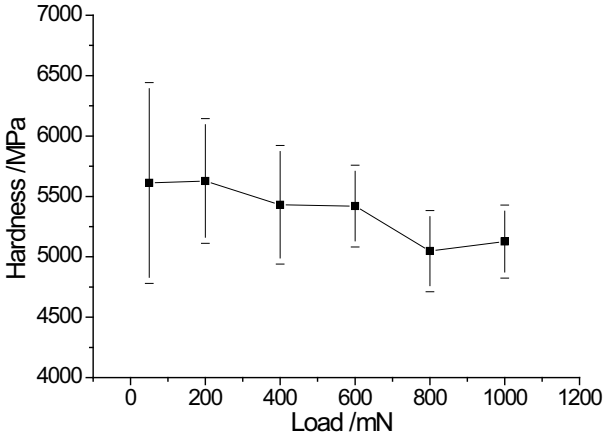

Figure 3.1.6: Hardness of BSCF measured by indentation as a function of loading force in ambient atmosphere. For each load 36 indentations were applied, and the standard deviation was given.

The fracture toughness was determined from the length of indentation cracks. First the applicability of equation (2.5) was examined at RT assuming that K_{Ind} should be independent of load for constant fracture toughness, i.e. linearity had to be demonstrated in a $c^{3/2}/P$ plot (see

Figure 3.1.7). The good linearity proves the validity of the method for determining fracture toughness. Efforts to establish the temperature dependence of fracture toughness were experimentally limited in the present work to measurements between RT and 350 °C. That was the maximum temperature which the used CSM heating stage could reach.

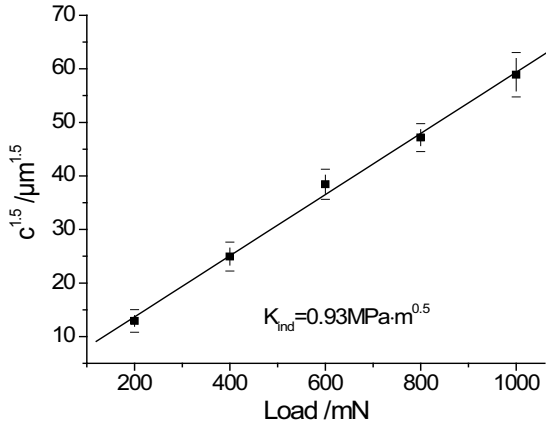

Figure 3.1.7: Crack length as a function of indentation load in ambient atmosphere. For each load 36 indentations were applied, and the standard deviation was given.

In order to investigate the influence of cooling rate and atmosphere on the Young's modulus and fracture toughness, samples were heated to 900 °C for 2 hours, and cooled with a cooling rate of 5 K/min in air and a cooling rate of 1 K/min in vacuum, respectively. Also a sample was directly taken out from the furnace at 900 °C, and quenched to RT in ambient atmosphere. The cooling rate of the quenched sample was assumed to be larger than 50 K/min. The Young's modulus and fracture toughness were measured by indentation with a load of 1000 mN in ambient atmosphere. The average value was calculated from 36 indentations for each load, and the standard deviation was given. Within the range of uncertainty the Young's modulus appeared to be independent from cooling rate (Figure 3.1.8). The Young's modulus of the sample annealed under vacuum (10^{-5} mbar) was about 5 % higher than the value of as-received

samples. Also the fracture toughness increased slightly with increasing cooling rate (Figure 3.1.9).

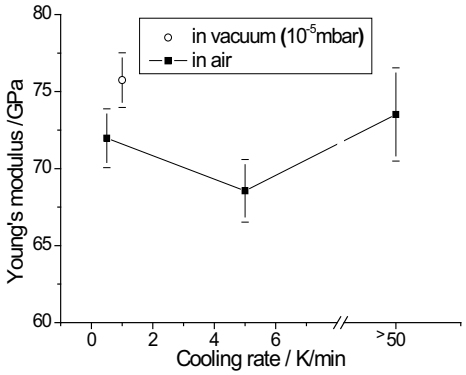

Figure 3.1.8: Young's modulus as a function of cooling rate measured in ambient atmosphere. For each cooling rate 36 indentations were applied, and the standard deviation was given.

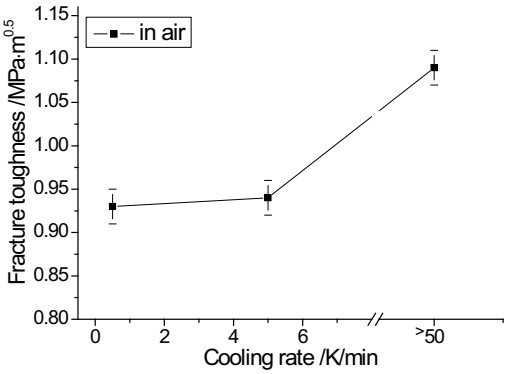

Figure 3.1.9: Fracture toughness as a function of cooling rate measured in ambient atmosphere. For each cooling rate 36 indentations were applied, and the standard deviation was given.

In real application the membrane is operated under an oxygen gradient. Therefore also the mechanical properties of samples annealed under dual atmosphere are of importance. Samples were annealed at 900 °C for 2 hours under a gradient of oxygen. One surface of the sample was exposed to air, and the other surface exposed to vacuum (2 mbar). At RT micro-mechanical properties were measured on the two surfaces and on polished cross sections of the specimens.

The values of hardness, Young's modulus and fracture toughness are constant across the thickness within the limit of uncertainty (Figure 3.1.10).

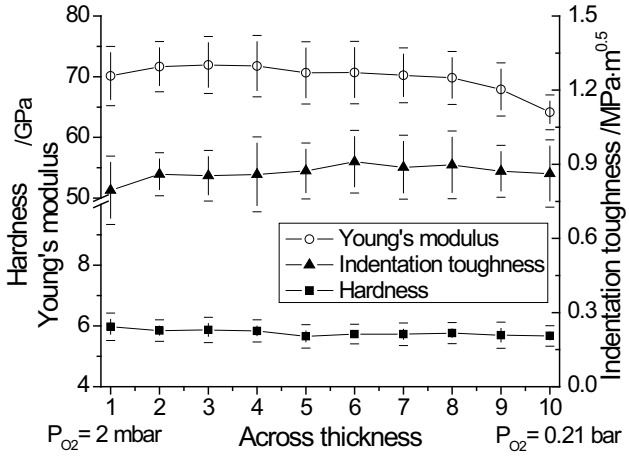

Figure 3.1.10: Young's modulus, hardness and fracture toughness through the thickness of BSCF specimens annealed in dual atmosphere (air/2 mbar)

Within a limited temperature range RT - 350 °C the indentation toughness was also derived from indentation tests with a load of 600 mN in air. Similar to the fracture stress results in the same temperature range, the indentation toughness decreases rapidly from RT to 150 °C, and then remains stable up to 350 °C.

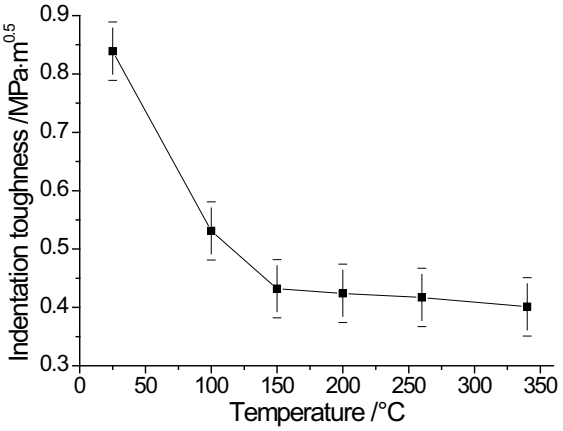

Figure 3.1.11: Indentation fracture toughness of BSCF as a function of temperature in air

A typical impression obtained at ~ 300 °C is shown in Figure 3.1.12(a). Contrary to the indentation pattern at RT, testing above 260 °C leads to deformation traces in grains surrounding the impression. The deformation traces were analyzed by optical microscopy, SEM and TEM (Figure 3.1.12), and identified as slip (Figure 3.1.12(c)). The slip traces reveal mainly a single orientation in a particular grain, which may indicate plastic deformation on a defined lattice plane. The slip plane could be indexed by TEM diffraction patterns to be (111) (Figure 3.1.12(d)). Interestingly ring-on-ring tests which were carried out at 900 °C with a maximum stress of ~ 45 MPa revealed no slip traces. The results indicate that a higher load stress is required for plastic deformation. In fact, around an impression the stresses are close to the hardness values, i.e. about 5000 MPa. During operation the membrane most likely does not experience such high stresses, and it can be concluded that plastic deformation by slip is not an important deformation process for membrane application.

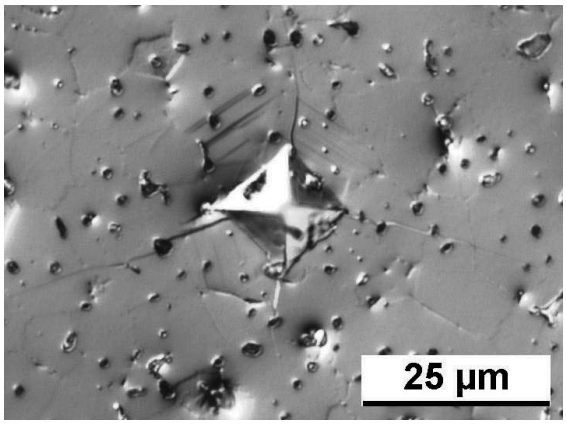

(a) Slip traces around indentation impression (600 mN). Optical micrograph of impression performed at 260 °C

(b) Slip traces around indentation impression observed by SEM

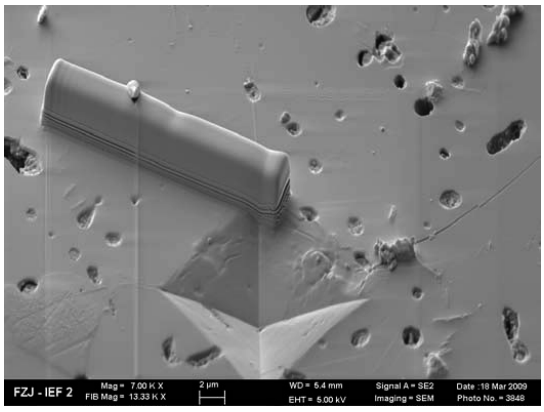

(c) Lamella of FIB cutting

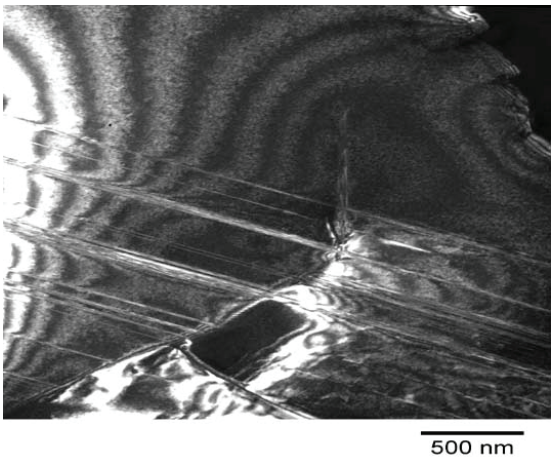

(d) TEM micrograph of Slip traces indexed as (111) planes

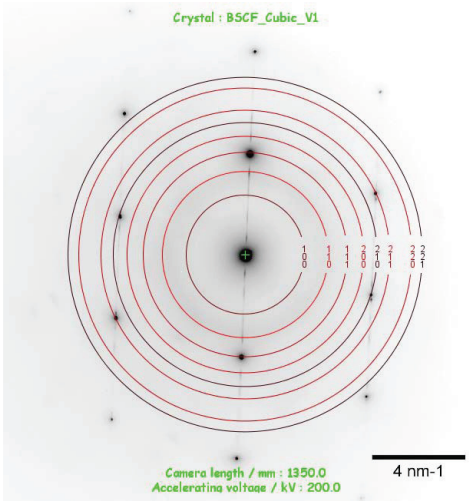

(e) Diffraction patterns by TEM

Figure 3.1.12: Slip traces of BSCF around indentation impression observed by TEM and SEM

3.1.3 Comparison of Young's modulus, fracture stress and fracture toughness

The thermo-mechanical characterizations of BSCF revealed for all determined parameters a decrease at intermediate temperature. Obviously there is qualitative agreement, but the normalized curves do not match quantitatively. In order to directly visualize the relative change, the values of Young's modulus, fracture stress and fracture toughness at various temperatures

were normalized with respect to the values of the as-received samples (Figure 3.1.13) [165]. Surprisingly the Young's modulus at 200 °C maintains 71 % of the value at RT, while the fracture stress is reduced to 57 %. The drop in indentation fracture toughness is even higher, only 32 % of the initial RT-value is measured at 200 °C. In general, fracture toughness and fracture stress are related by [122]

$$K_{Ind} = Y \sigma_c \sqrt{c} \qquad (3.1.1)$$

where Y is a crack shape geometry factor (Y = 1.27 for semicircular surface cracks [122]), σ_c is the fracture stress, and c is a critical crack length. For RT the average fracture stress of ~ 99 MPa, with a fracture toughness of 0.99 MPa·√ m thus yields a critical crack length of $c \approx 62$ μm. The size of defects may change during heating due to thermal expansion, but the relative change in size of such a defect with temperature is expected to be very small. Therefore, the normalized values of fracture stress and fracture toughness should show identical behavior. And they are basically consistent, which is displayed in Figure 3.1.13.

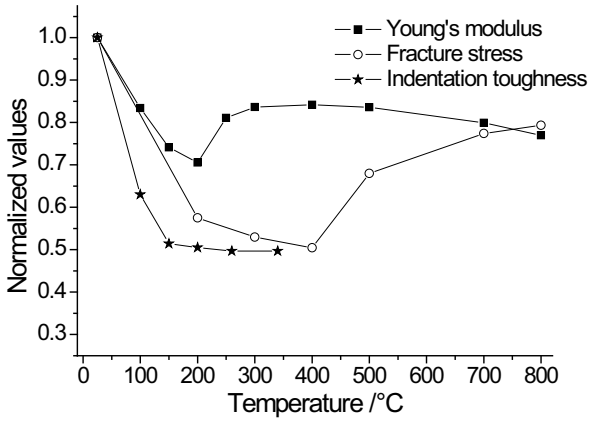

Figure 3.1.13: Normalized values of the Young's modulus, fracture stress and indentation fracture toughness

3.1.4 Fracture surfaces

The fracture surfaces of the specimens tested at various temperatures were investigated with SEM to gain information about the fracture mode. Fracture surfaces from specimens tested between RT and 900 °C are shown in Figure 3.1.14. Transgranular fracture is observed for all temperatures. Although precipitates appear along the grain boundaries obove 700 °C, this effect causes no interfacial weakening. Also, no deterioration of the mechanical properties by the second phase was observed.

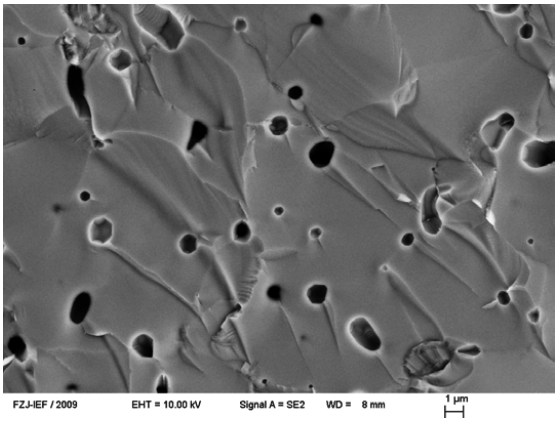

(a) at RT

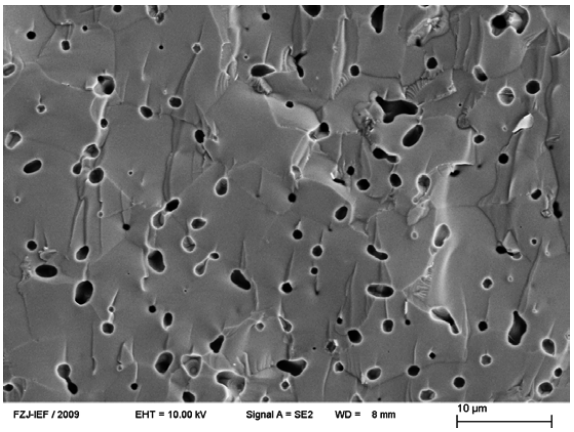

(b) 200 °C

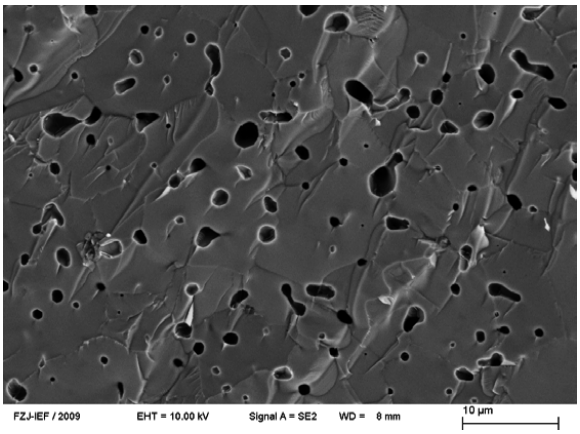

(c) 400 °C

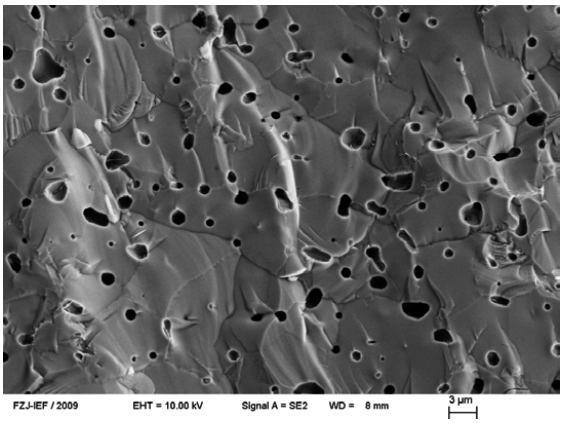

(d) 500 °C

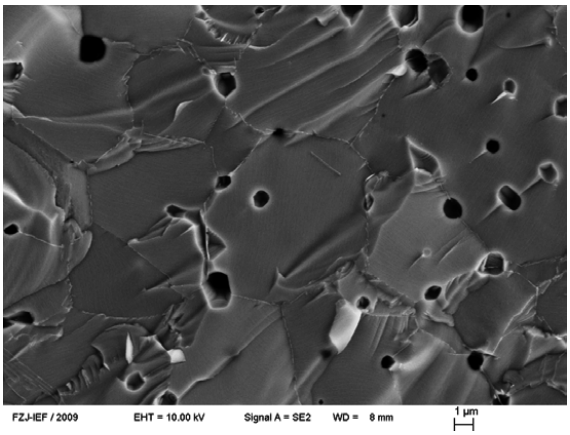

(e) 700 °C

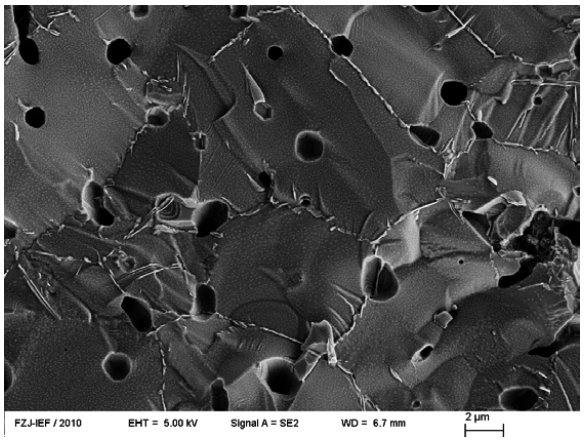

(f) 800 °C

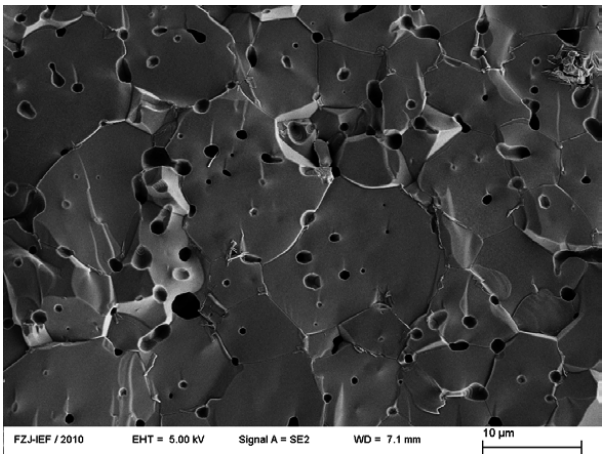

(g) 900 °C

Figure 3.1.14: Fracture surfaces of BSCF specimens tested at various temperatures

3.1.5 Discussion of possible mechanisms governing the mechanical anomaly

Only few explanations for a Young's modulus anomaly of perovskites can be found in the literature [41, 94, 166, 167]. The effect has been attributed essentially to four possible mechanisms: 1. unfreezing of domain walls [166]; 2. Phase transition [41]; 3. association/dissociation of defects and ions [167]; 4. spin transition from low spin (LS) to high spin (HS) [94].

A rapid decrease of the Young's modulus at intermediate temperatures (between RT and ~ 300 °C) reported for $LaAlO_3$ was attributed to the gradual unfreezing of domain walls [166]. However this mechanism is not likely to be the reason for the mechanical anomaly of BSCF. BSCF has a cubic symmetry in the respective temperature range, so there is no domain formation and switching effect [65, 168]. Furthermore, no signs of domain structure were observed in the present study with TEM. Also an unfreezing of domain walls would not explain the recovery of Young's modulus.

A similar sharp decrease in fracture toughness reported for $LaCoO_3$ and $La_{0.8}Ca_{0.2}O_3$, has been attributed in part to the continuous decrease of ferro-elasticity with increasing temperature [66, 104]. As discussed for Young's modulus, that cannot be the case for BSCF, since BSCF has a cubic structure at the relevant temperatures and shows total para-elastic behavior. No hysteresis in the load-displacement curves was observed in ring-on-ring testing.

As an alternative mechanism it has been suggested that the association/dissociation reaction between point defects could cause mechanical anomalies in particular temperature ranges [100, 167]. An intermediate temperature anomaly reported for $LaCoO_3$ [104, 169] was attributed to a spin transition of Co^{3+}. The effect will be discussed in detail below.

It is not known why the fracture stress remains low up to 400 °C and rises up from 500 °C (Figure 3.1.3). Between 400 °C and 500 °C only the TEC increases rapidly due to chemical expansion, and the Young's modulus maintains a stable value. This cannot explain, however, the fracture stress increase at higher temperatures. Further experimental work might help to shed more light on the discrepancy of the fracture stress and the Young's modulus.

3.1.5.1 Structural characterization with XRD

Samples were heated to 150 °C, 200 °C and 300 °C, respectively, with a heating rate of 0.5 K/min and then annealed for 24 hours in order to get more insight into the origin of the

anomaly. Afterwards the samples were quenched in water. The crystal structure was characterized with XRD at RT. All quenched samples exhibited pure cubic structure (Figure 3.1.15). It has been reported that BSCF maintained a cubic structure from RT up to 1000 °C in air [14, 42]. However, it has also been reported [41] that the cubic structure of BSCF transforms during long-term exposure (10 days) gradually to a hexagonal polymorph in the temperature range 700 °C – 900 °C. The transformation is claimed to proceed via a nucleation and growth mechanism [41]. At low temperatures the transformation is inhibited due to the low diffusion rates and high nucleation energy in the lattice. Considering the temperature range and time range of the present experiments, BSCF should maintain a cubic structure throughout the tests. Therefore, a phase transition can be excluded as a possible reason for the mechanical anomaly.

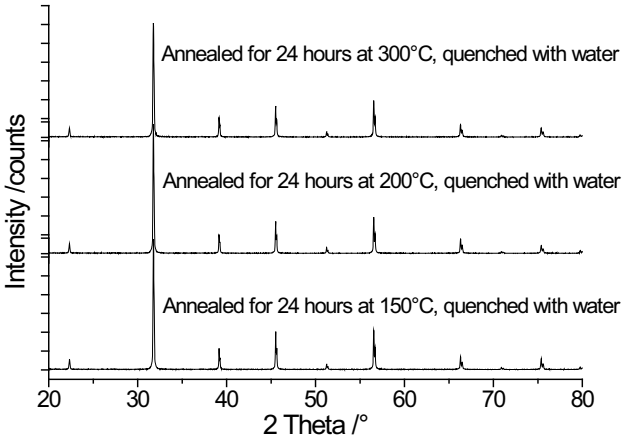

Figure 3.1.15: XRD results of BSCF annealed at various temperatures

3.1.5.2 Phase stability at high temperatures

In order to get insight into the high temperature behavior, the samples were heated to 750 °C, 800 °C and 950 °C with a heating rate of 5 K/min, respectively, and then annealed for 336 hours. After annealing the samples were directly taken out from the furnace to quench the high temperature structure.

For the sample annealed at 750 °C a second phase appears to be visible in the optical micro-graph. This second phase can only be observed along the grain boundaries in a sample annealed at 800 °C. The sample annealed at 950 °C exhibits only a single phase, as is shown in Figure 3.1.16.

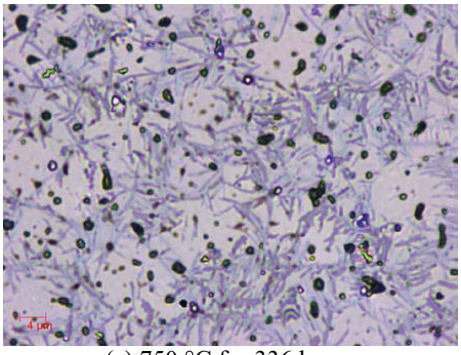

(a) 750 °C for 336 hours

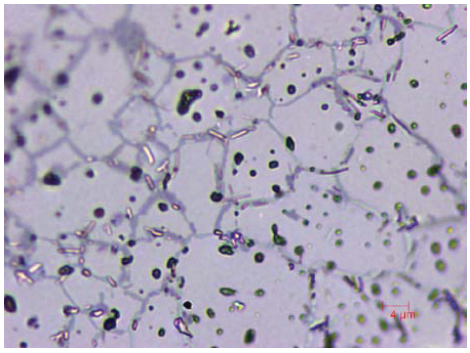

(b) 800 °C for 336 hours

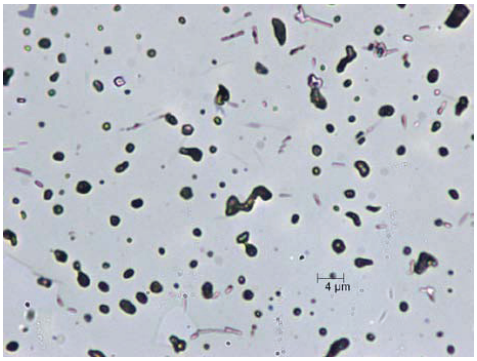

(c) 850 °C for 336 hours

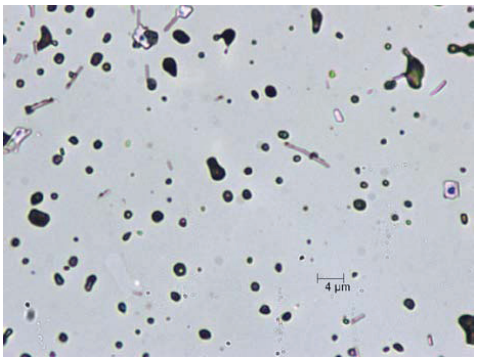

(d) 900 °C for 336 hours

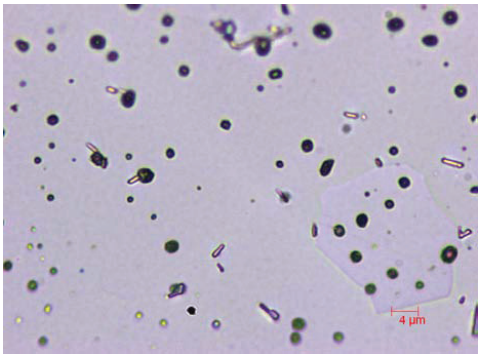

(e) 950 °C for 336 hours

Figure 3.1.16: Optical micrographs of samples annealed at various temperature

The second phase was identified by XRD to have hexagonal structure, and the quantity of hexagonal phase decreased with annealing temperature from 750 °C to 800 °C. The pure cubic structure of the as-received samples could be in meta-stable state due to low diffusion rate, and thus has a potential to transform to hexagonal structure.

The precipitation effect of BSCF can be interpreted by a basic thermodynamic process. A solid solution is formed if two ingredients are soluble:

$$AO_2+BO \rightarrow ABO_3 \qquad (3.1.2)$$

The solving process implies that the bonds in AO_2 and BO are first broken, and then recombine to form ABO_3. When the two solutes are oxides, the nearest neighbors of A and B are still oxygen atoms. However, the structure and coordination number of A (B) in the solution maybe

be different from the ingredients, and the next neighbors are also different. Therefore, the enthalpy of solving ΔH (= $H(ABO_3)$ - $H(AO_2)$ - $H(BO)$) could be negative (exothermic), zero, or positive (endothermic). The entropy of solving ΔS (= $S(ABO_3)$ - $S(AO_2)$ - $S(BO)$) is positive, for the solving process always increases the disorder. The Gibbs free energy of solving is $\Delta G = \Delta H - T\Delta S$. The sign of ΔG determines the direction of the process. When ΔG is negative, the solution is stable. When ΔG is positive, the solution tends to separate into two ingredients. When ΔH is negative, the ΔG is always negative independent from temperature. That means the solution is stable at all temperatures. When ΔH is positive, ΔG is positive for low temperature ($T < \frac{\Delta H}{\Delta S} = T_0$), and the solution tends to separate; ΔG is negative for high temperature ($T > \frac{\Delta H}{\Delta S} = T_0$), and solution is stable.

The driving force for separation is the inverse of the Gibbs energy of dissolution

$$-\Delta G=-(\Delta H-T\Delta S)=-(T_0\Delta S-T\Delta S)=(T-T_0)\Delta S \qquad (3.1.3)$$

The lower the temperature is, the higher is the driving force. However, besides the driving force the separation is also controlled by diffusion and activation energy (nucleation process) or only by diffusion (spinodal decomposition). Therefore, at low temperatures, even when the driving force is high, the solution may be in a meta-stable state due to the low diffusion rate. The precipitation was mainly found along grain boundaries and on the surface, which could be due to the lower activation energy (surface energy of nucleation, elastic energy of volume change) and high diffusion rate compared with the lattice.

From the thermodynamic analysis of solution and the experimental results, it can be concluded that the critical temperature of dissolving is between 800 °C and 850 °C.

3.1.5.3 Association and dissociation of defects

The BSCF contains two types of point defects, metal ions and oxygen vacancies. They could interact with each other by an association/dissociation reaction [167]:

$$M' + V^{\bullet\bullet} \leftrightarrow (M':V^{\bullet\bullet})^{\bullet} \qquad (3.1.4)$$

The reaction is accompanied by a volume change. The strain associated with the shift of the equilibrium is called chemical strain [167]. Although some conclusions can be drawn from the simple dimer cluster ($M'V^{\bullet\bullet}$)$^{\bullet}$ model, trimers ($2M'V^{\bullet\bullet}$) may also play a significant role in BSCF [167, 170]. The Clausius-Clapeyron equation describes the effect of small changes [171]:

$$\frac{\Delta P}{\Delta T} = \frac{S_2 - S_1}{V_2 - V_1} = \frac{\Delta S}{\Delta V} = \frac{\Delta H}{T_e \Delta V} \qquad (3.1.5)$$

where ΔP is a small pressure change (stress), ΔT is a small temperature change, ΔH is the enthalpy change of the reaction, ΔV is the associated volume change, and T_e is the reaction temperature without external stress. The equilibrium can be changed by external stress, but the critical stress increases with a deviation from T_e. The external stress plays a significant role only in a temperature range around T_e. At low temperature the reaction is frozen, and at high temperature the clusters dissociate completely [167]. As a result of this relationship, the total strain ε_t comprises two parts, mechanical strain ε_m and reaction strain ε_r. The apparent elastic modulus was calculated by the quotient of external stress σ and total strain ε_t. Depending on the value of chemical strain ε_m, the apparent E-modulus may exhibit an anomaly at intermediate temperatures.

An enthalpy change is observed at about 240 °C – 250 °C in the DTA curve (Figure 3.1.17), which might be an indication of an association/dissociation process. However, the same anomaly was also measured by the resonance evaluation of the elastic behavior (see Figure 3.1.2). Since the atoms only vibrate a small distance, the association/dissociation reaction may

not contribute to the anomaly of Young's modulus. Furthermore, the reaction strain cannot explain the decreases of the fracture stress and the indentation fracture toughness, since the reaction strain always relaxes the stress in the highly stressed zone.

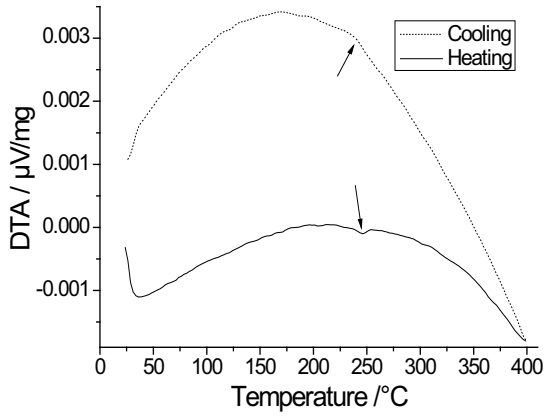

Figure 3.1.17: Differential thermal analysis (DTA) curve of BSCF in air

3.1.5.4 Spin transition

The spin transition of Co^{3+} in $LaCoO_3$ has been studied extensively since the 1950s [94-97]. As shown in Figure 1.13, five orbitals in the 3d shell of Co^{3+} (d^6) are split by the crystal field into two groups: t_{2g} (3 orbitals) and e_g (2 orbitals). In an atom the 5 orbitals in the 3d shell are degenerate, i.e. they have the same energy level, but the electrons distribution is changed by the interaction with oxygen ions in the lattice. The energy of the t_{2g} orbitals is lower than that of the e_g orbitals. At very low temperature, the 6 electrons of Co^{3+} occupy the t_{2g} orbitals, and the e_g orbitals are empty. Since all electrons are paired, the spin of Co^{3+} is zero. With increasing temperature electrons can be thermally activated to e_g orbitals. Each electron has a half-spin, and depending on the number of unpaired electrons the spin of Co^{3+} can be 1 or 2. Some of non-magnetic Co^{3+} (LS, S=0) are thermally activated to magnetic Co^{3+} (IS, S=1 or HS, S=2). At about 200 °C the amount of magnetic Co^{3+} is saturated [98].

This transition can be confirmed by measurements of the magnetic susceptibility. The susceptibility (χ) of paramagnetic materials is described by the Curie-Weiss law [88]:

$$\chi = \frac{C}{T - \Delta} \tag{3.1.4}$$

where T is the temperature, C and Δ ($< T$) are positive material constants. Normally χ decreases with temperature. However, C contains the density of the magnetic moments n_1:

$$C = n_1 C_1 \rightarrow \chi = \frac{n_1 C_1}{T - \Delta} \tag{3.1.5}$$

If the density of magnetic moments (n_1) increases more rapidly, χ may increase with temperature. The magnetic susceptibility of BSCF was measured with a Quantum Design Physical Property Measurement System (PPMS). The susceptibility of BSCF as a function of temperature is shown in Fig. 3.1.18 [165]. A maximum of χ can be observed at ~ 250 °C. The result confirms the existence of a spin transition. The transition is accompanied by an abnormal expansion of Co ions [95, 169], which may strongly influence the mechanical behavior of BSCF [104].

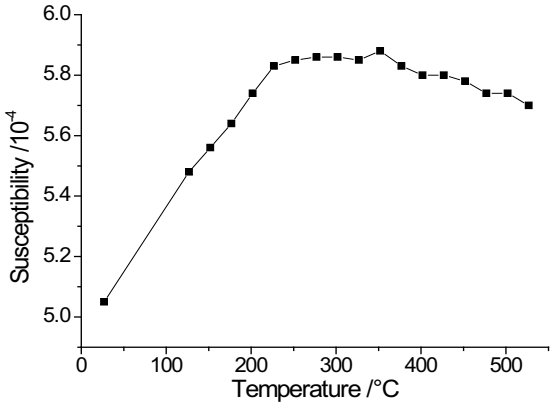

Figure 3.1.18: Magnetic susceptibility of BSCF as a function of temperature in air

3.1.5.5 Thermal and chemical expansion

With increasing temperature or decreasing oxygen partial pressure, the perovskite loses part of its oxygen with oxygen vacancies being left [56]. At the same time, metal ions M^{n+} are reduced to lower valence $M^{(n-1)+}$: $2M^{n+} + O^{2-} \rightarrow 2M^{(n-1)+} + O_2(g)$. Since the radius of $M^{(n-1)+}$ is larger than that of M^{n+}, along with this reaction the lattice of the perovskite will expand. This effect is called chemical expansion [57, 58].

Thermal expansion and the scientific and technical [165] TECs of BSCF are displayed in Figure 3.1.19(a) and 3.1.19(b). Obviously the scientific TEC (α_{Sci}) shows the effect of the lattice expansion better resolved. Correspondingly, only α_{Sci} is taken into account in the following considerations. The lattice expansion could consist of four components. These are lattice vibration, spin transition, dissociation of point defects and chemical expansion. As discussed above, the low spin - high spin transition is accompanied by abnormal expansion of the Co ions. The higher value at RT – 200 °C on the α_{Sci} curve may be related to such a transition, which is consistent with the susceptibility values. The susceptibility increases rapidly from RT to 250 °C. The rapid increase of the α_{Sci} from 450 °C to 530 °C is attributed to chemical expansion, since an apparent oxygen loss is observed above 450 °C by TG investigations (Figure 3.1.20). However, the additional peaks in the α_{Sci} curve are not yet fully understood. These effects might also be related to vacancy - ion cluster configurations [104, 168, 172].

An enthalpy change observed at ~ 240 °C - 250 °C in the DTA curve (Fig. 3.1.17) has been attributed to the dissociation of point defects [167]. However, no volume changes that might be expected to take place as a result of such reactions can be observed in the thermal expansion curve (Fig. 3.1.19(b)).

The TG curve of BSCF is shown in Fig. 3.1.20. From ~ 490 °C lattice oxygen is gradually released with increasing temperature. After the cooling process the sample does not return to its

original weight until ~ 400 °C. The hysteresis at about 400 °C – 500 °C could be due to the limitation of oxygen diffusion. The composition of BSCF is not stable at high temperatures, and from ~ 490 °C part of the lattice oxygen is released (Fig. 3.1.20). However, above 300 °C Young's modulus behaves like that of a normal ceramic, which indicates that Young's modulus is not very sensitive to oxygen stoichiometry.

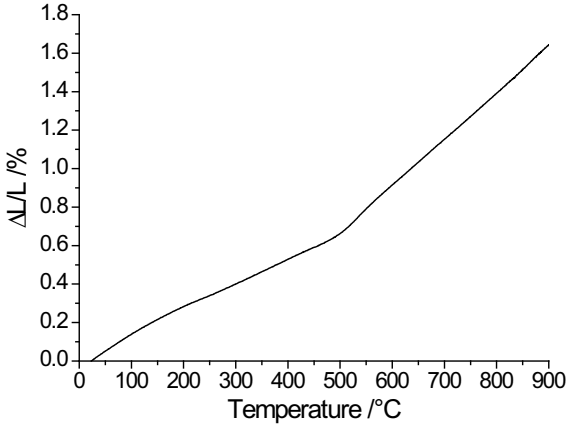

(a) Thermal expansion

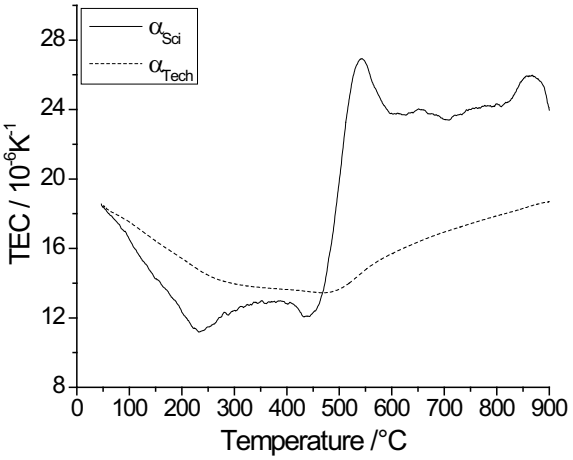

(b) α_{Sci} (solid line) and α_{Tech} (dotted line)

Figure 3.1.19: Thermal expansion behavior of BSCF in air

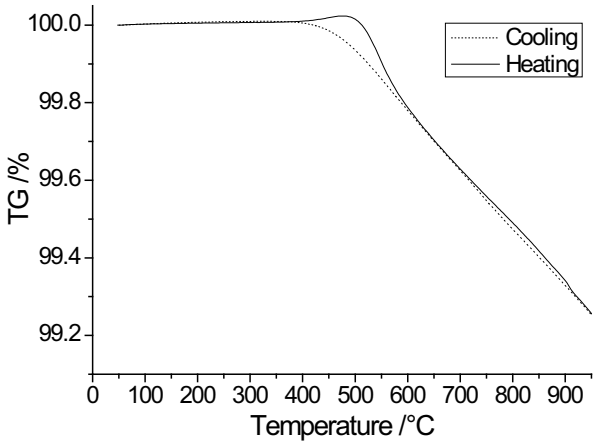

Figure 3.1.20: Thermal gravity (TG) curves of BSCF

3.2 LSCF

3.2.1 Non-linearity of load-displacement

Typical load-displacement curves measured at various temperatures using ring-on-ring tests are shown in Figure 3.2.1. Below 700 °C the curves are non-linear. At RT a decrease of the slope is observed above ~ 80 N (40 MPa). This deviation point gradually decreases with increasing temperature, and cannot be recognized anymore at 700 °C. Between 200 °C and 700 °C an increase of the slope is also observed when further increasing the load.

Complementary SEM investigations after room temperature bending tests revealed the presence of crystallographic domains in many grains of the stressed sample surface. Hence the non-linear deformation characteristics are likely to be related to the ferro-elasticity of the perovskite material [65]. A detailed analysis of the ferro-elastic effect in LSCF will be given later.

The onset of domain activity seems to be reflected by the first deviation towards a shallower slope of the load-displacement curves. Interestingly, after some displacement corresponding to

higher loads, the deformation curves tend to become steeper again indicating a saturation of the domain formation process. Since the rhombohedral distortion from cubic symmetry appears to decrease gradually to zero from RT to the transition temperature (~ 750 °C) [10, 59, 173], it can be assumed that the critical stress for domain switching decreases with increasing temperature. No defined change in slope is observed at 700 °C, and the critical stress would therefore be almost equal to zero. At RT the specimens break before the saturation stress is reached, whereas between 200 °C and 700 °C the saturation is observed. At 800 °C the samples have a cubic structure and are para-elastic, hence the load-displacement curve is linear [59].

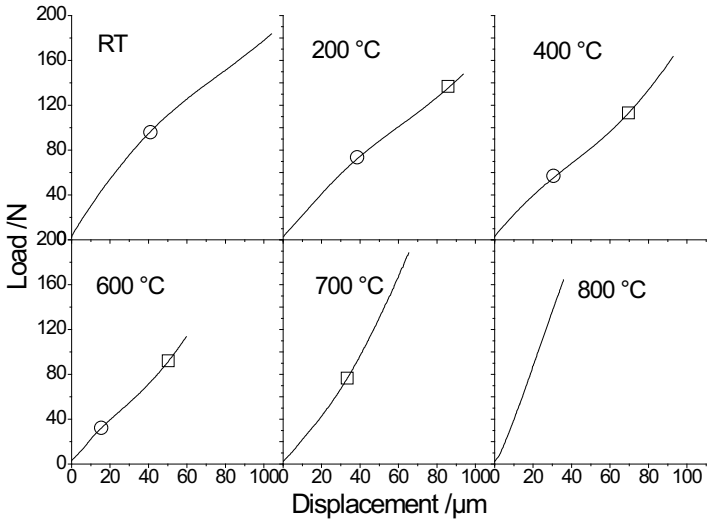

Figure 3.2.1: Typical load-displacement curves of LSCF at various temperatures in air. The first deviation of the slope from linearity is indicated by circles (○), and the saturation point is indicated by rectangles (□). The samples fractured at the end of the curves.

When the first and the second deflection of the slope are assumed to be the onset and the saturation of the domain switching, respectively, the load of the onset and the saturation of the domain switching can be qualitatively obtained at various temperatures from Figure 3.2.1. The

onset load is ~ 100 N at RT, and decreases almost linearly to zero at 700 °C. The saturation load is ~ 140 N at 200 °C, and decreases linearly to ~ 80 N at 700 °C (Figure 3.2.2).

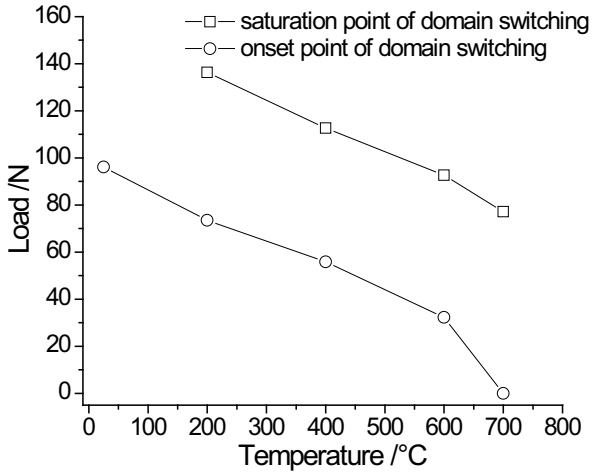

Figure 3.2.2: Temperature dependence of onset and saturation load of domain switching in LSCF

3.2.2 Young's modulus

3.2.2.1 Young's modulus in air

To evaluate the interesting temperature effect of the elastic behavior of LSCF, a series of loading/unloading cycles has been carried out at various temperatures between RT and 800 °C in air. Young's moduli measured by ring-on-ring test and first preliminary results obtained with resonance method are shown as a function of temperature in Figure 3.2.3. The Young's moduli determined using the two methods agree well. The Young's modulus exhibits an initial decrease, and stays relatively stable up to ~ 600 °C, followed by a strong increase. The initial decrease of Young's in LSCF is larger than in normal ceramics, i.e. a higher decrease than 1% per 100 K with increasing temperature [122]. Since it is very unlikely that the ferro-elastic domains can switch during resonance measurement, a correlation with the easier onset of

domain switching with increasing temperature can be excluded. Further experiments need to be done to elaborate and explain the phenomenon of initial decrease of Young's modulus.

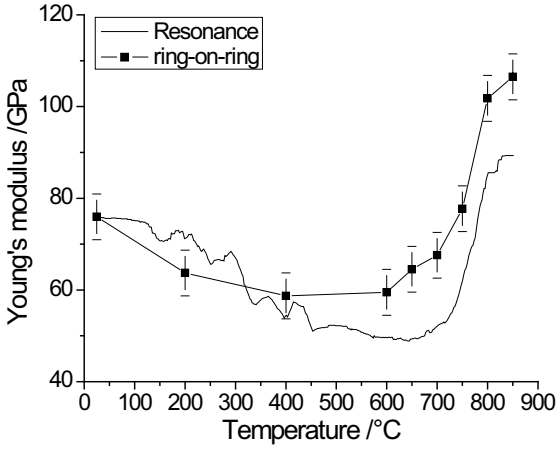

Figure 3.2.3: Young's modulus of LSCF as a function of temperature measured by ring-on-ring test and resonance method in air. For ring-on-ring tests, 5 measurements were carried out for each temperature, and the standard deviations were given.

Earlier reports [19, 48, 49] suggested that the lattice structure of La(Sr)Fe(Co)O_3 depends on temperature and the amount of Sr and Co doping. As shown in Figure 1.4, a transition from rhombohedral to cubic symmetry occurs at about 800 °C for $La_{0.6}Sr_{0.4}FeO_{3-\delta}$ [49]. This transition is a second-order transition, i.e. no discrete volume or enthalpy change occurs as a result of the phase transition [49]. Cubic symmetry is favoured by increasing temperature and oxygen deficiency [60, 174]. The strong increase of Young's modulus between 700 °C and 800 °C seems to reflect this rhombohedral to cubic transition.

3.2.2.2 Young's modulus under vacuum (10^{-5} mbar)

The samples were annealed at 900 °C for 2 hours under vacuum (10^{-5} mbar), and the Young's modulus was measured using ring-on-ring tests during the cooling process for the first heating cycle and heating or cooling process for the subsequent heating cycles. During the first heating of the as-received samples, the values of Young's modulus under vacuum conditions are still

the same like those in air due to the slow diffusion of oxygen. Upon cooling high values of Young's modulus are maintained until RT, and no abrupt change is observed throughout the temperature range (Figure 3.2.4).

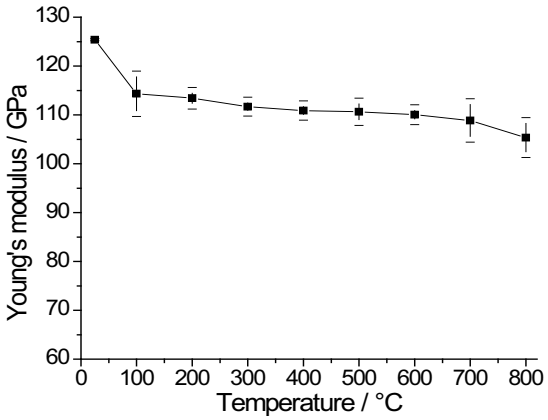

Figure 3.2.4: Young's modulus of LSCF under vacuum (10^{-5} mbar). The average value was calculated from 5 measurements, and the standard deviation was given.

The oxygen deficiency in the samples is higher under vacuum than in air for a particular temperature [175, 176], and the higher concentration of oxygen vacancies in vacuum is responsible for the stabilisation of the cubic structure [60, 174]. The stabilization (existence at a lower temperature than in air) of the cubic structure under vacuum is suggested to be a result of the formation of an ordered structure [174, 177].

The difference of Young's modulus determined from separate tests in air and vacuum generates interest in dual atmosphere exposure of a single sample. A sample was annealed at 900 °C for 2 hours under a steady gradient of oxygen. Note that this test should represent the operation conditions of the membrane. During annealing one side of the sample was exposed to air, and the other side to vacuum (20 mbar). Keeping the difference in P_{O2}, the sample was cooled thereafter with a rate of 0.5 K/min to RT. Micro-mechanical properties were characterized by indentation with a load of 1000 mN at RT. Young's modulus and hardness maintain a relatively

stable value across the thickness, but the indentation toughness decreases from ~ 0.64 to ~ 0.42 MPa·m$^{0.5}$ with increasing P_{O2} (Figure 3.2.5). Since Young's modulus increases by ~ 50 % with the transition from rohmbohedral to cubic symmetry (compare Figure 3.2.3 and Figure 3.2.4), the almost stable value of Young's modulus in Figure 3.2.5 indicates that the chosen low P_{O2} does not stabilize the cubic structure. The higher value of the indentation toughness K_{ind} can be attributed to the compressive stress at the lower P_{O2} side. The specimen will release oxygen when exposed to low P_{O2}, and the lattice expands with the release of oxygen. Consequently, the specimen experiences a compressive stress at lower P_{O2} side, and correspondingly, a tensile stress at higher P_{O2} side.

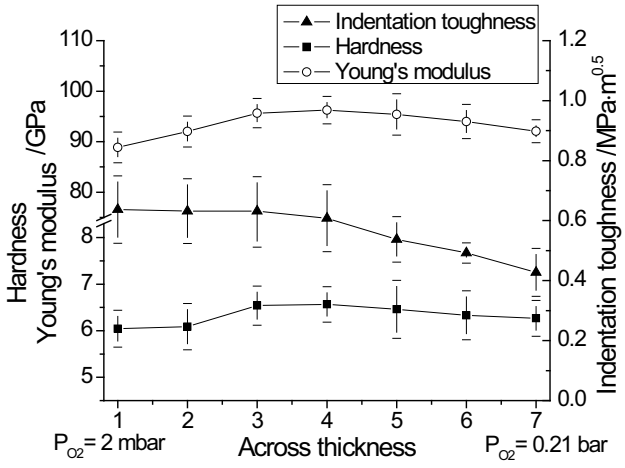

Figure 3.2.5: Young's modulus, hardness and fracture toughness through the thickness (1 mm) of a LSCF sample exposed to a gradient in P_{O2}

3.2.3 Phase compositions of LSCF

In-situ high temperature XRD was carried out to characterize the temperature dependence of the crystalline structure. Since almost all diffraction peaks of rhombohedral and cubic symmetry overlap, the determination of the temperature at which the transition actually occurs has uncertainties. From structural modeling of the XRD data, it is known that the (113) peak at

38.5 ° appears in rhombohedral, but is not present in the cubic symmetry. Characteristic curves obtained using high-temperature XRD are shown in Figure 3.2.6. The rhombohedral (113) peak disappears at 850 °C in air, which is an indication that only the cubic phase exists at (and above) this temperature. That is in agreement with literature [49].

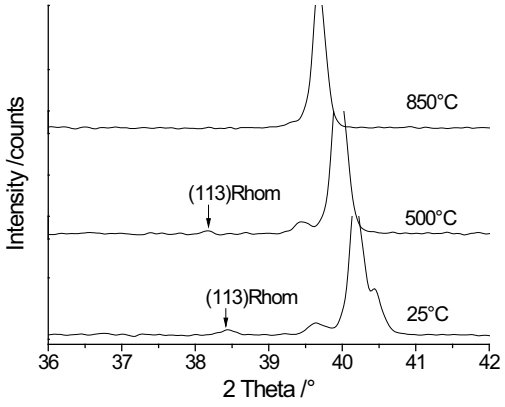

Figure 3.2.6: In-situ high-temperature XRD patterns of LSCF

Some of the LSCF samples were heat treated to study the influence of thermal history on phase composition. Figure 3.2.7 shows the XRD results after annealing at 900 °C for 2 hours and subsequent different cooling rates of 5 K/min and 8 K/min in air, and 1 K/min under vacuum (10^{-5} mbar). The phase compositions were quantified with Rietveld refinement of the XRD data. Apparently the phase composition of LSCF depends on the cooling rate and atmosphere. The crystal structure of the as-received samples was purely rhombohedral. For the samples annealed in air and cooled with rates of 5 K/min and 8 K/min the amount of cubic phase was 15 % and 23 %, respectively [59]. The samples, which were cooled down to RT under vacuum at a rate of 1 K/min, exhibited purely cubic symmetry. Also the diffraction peaks of the XRD measurements shifted to a lower angle, indicating an increase of the lattice constant. Note that the cubic symmetry could also be stabilized to RT by fast cooling in air, but typically the

quenching caused specimen fracture. The structure of the quenched sample was indexed by XRD to be also purely cubic.

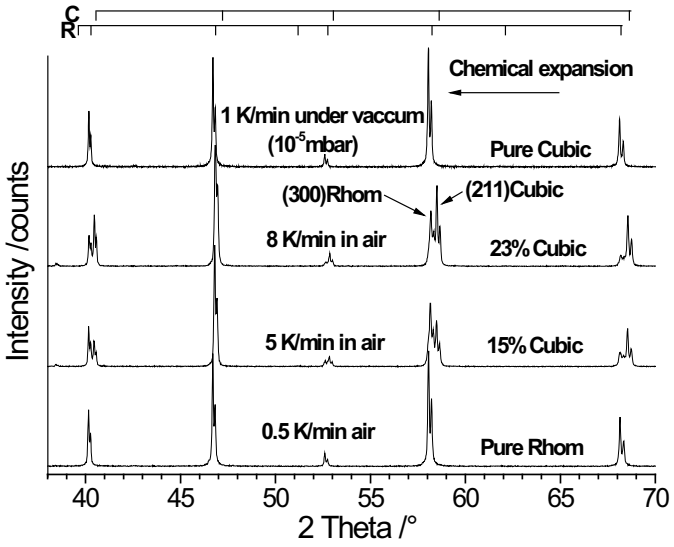

Figure 3.2.7: Room temperature XRD diffraction patterns of LSCF samples after different heat treatments. After annealing at 900 °C various cooling rates in air and under vacuum (10^{-5} mbar) were applied.

3.2.4 DTA/TG

Additional measurements were carried out using DTA/TG in air with a heating rate of 2 K/min. Between 700 °C and 850 °C in air, a sharp decrease in the DTA signal is observed (Figure 3.2.8), which could be attributed to a change in heat capacity rather than any thermal effect, since the change from rhombohedral to the cubic phase is a second-order transition [49]. The temperature range of the change in the DTA signal is in good agreement with that of the Young's modulus measurements. The curve of the TG measurement also reveals a continuous decrease of specimen weight above 600 °C with increasing temperature (Figure 3.2.7), which suggests a continuous release of oxygen. In agreement with literature, it can be concluded that there is no compositional change associated with the phase transition [49, 60].

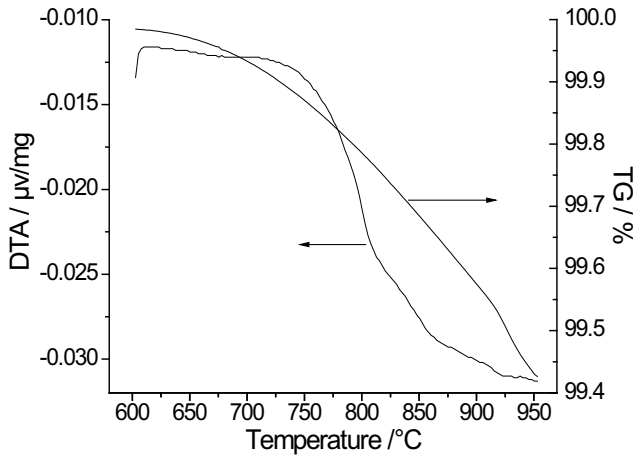

Figure 3.2.8: TG and DTA curves of LSCF measured in air with a heating rate of 2 K/min

Literature [46, 178] suggested that the lattice structure of La(Sr)Fe(Co)O_3 depends on the temperature and the amount of Sr and Co doping. The cubic symmetry was assumed to be favored by increasing temperature and oxygen deficiency [60, 178]. In $La_{0.6}Sr_{0.4}FeO_{3-\delta}$ the transition is a second-order transition, i.e. no discrete volume or enthalpy change occurs [49]. Supported by in-situ XRD and DTA measurements, LSCF was reported to transform from rhombohedral to cubic between 700 °C and 800 °C [59]. Normally, a second order transition should occur at a defined temperature, i.e. two phases cannot coexist, and the high-temperature symmetry cannot be stabilized by fast cooling alone [179]. However, the transition temperature also depends on the oxygen deficiency. Hence, since the diffusion rate of oxygen is limited, the transition could occur in a range of temperatures. Thus part of the cubic phase can be stabilized to RT if the oxygen deficiency is not homogeneously distributed. The dependence of the phase content on cooling rate and atmosphere (Fig. 3.2.7) proved this assumption. The results indicate that the kinetics of oxygen diffusion is essential for the phase compositions at low temperatures.

3.2.5 Thermal and chemical expansion

Thermal expansion and the thermal expansion coefficient (TEC) are displayed in Figure 3.2.9. The TEC increases more rapidly above ~ 600 °C, which is attributed to chemical expansion, because continuous loss of oxygen was observed from ~ 600 °C with TG (Figure 3.2.8). With increasing temperature or decreasing partial pressure of oxygen, the oxygen in the lattice will be released, and along with that the lattice expands [46, 49, 89]. Two possible explanations for this chemical expansion are given in the literature [46]: i) the repulsion forces between those mutually exposed cations when oxygen ions are released from the lattice; ii) the increase in cation size due to the reduction of the cations from higher to lower valences, an effect which occurs simultaneously with the creation of oxygen vacancies in order to maintain electrical neutrality.

In fact, both explanations predict a weakening in bond strength which contradicts the measured increase of Young's modulus with increasing oxygen vacancies. The stiffness of the LSCF samples annealed under vacuum (10^{-5}mbar) was about 139 ± 3 GPa (measured from indentation tests with a load of 1 N) and the lattice constant was 0.390 nm, while the values of as-received samples were 102 ± 4 GPa and 0.387 nm, respectively. Obviously, the hard sphere assumption of ions [46] is an oversimplified model. The properties of materials originate from the lattice electron density distribution. Up to now, no detailed analysis of the electron distribution is available. Yet, the effect may be explained in the following way: In the lattice two electrons are closely distributed around an oxygen ion due to its higher electro-negativity. When the oxygen is released, the remaining electrons move to the space between cation and anion, which results in an expansion of the lattice, and at the same time, increases the bonding strength.

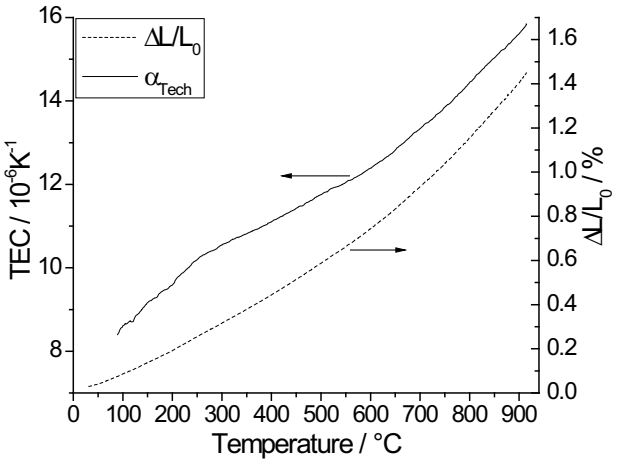

Figure 3.2.9: Thermal expansion and thermal expansion coefficient of LSCF in air

3.2.6 Domain structure of LSCF

The specimens were deformed using ring-on-ring test with a load stress of ~ 50 MPa. Although details of the ferro-elastic deformation need further elaboration, the micro-structural evidence of domains in the deformed LSCF specimens is unambiguously confirmed by SEM and TEM observations (Figure 3.2.10 and 3.2.11). Domains can be found almost in all rhombohedral grains (Fig. 3.2.10(a)), and the width of the domains is ~100 nm. The domain formation contributes to strain without increasing necessarily the stress [180]. The non-linear effect of load-displacement is attributed to this deformation. Note that a limited number of domains has also been recognized in as-received samples.

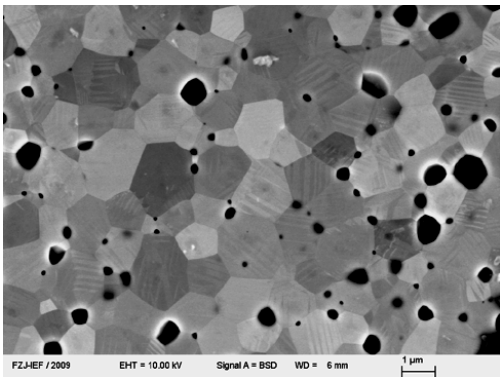

(a) Overview

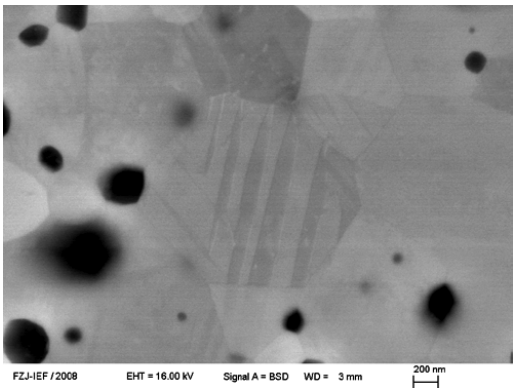

(b) Within a single grain

Figure 3.2.10: SEM micrographs of ferro-elastic domains in deformed LSCF sample

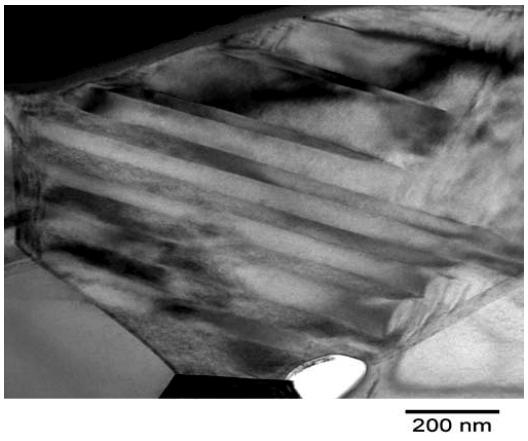

Figure 3.2.11: TEM micrograph of ferro-elastic domains in deformed LSCF sample

The domain structure was further characterized by in-situ observation using a heating stage in the TEM. Under RT conditions the domains can be clearly seen, while at 400 °C the domain contours start to fade with some weak contrast of domains still visible (Figure 3.2.12). The domains completely disappeared at 700 °C. After cooling to RT, the domains did not reappear, since the high temperature cubic structure was maintained.

As discussed before, the cubic symmetry exists at high temperature and in the presence of oxygen vacancies [60, 178], but can also be stabilized under vacuum (10^{-5} mbar) down to RT. Since the pressure in the TEM chamber is also about 10^{-5} mbar, the cubic structure is in principle thermodynamically favorable. Thus starting with a rhombohedral material it can maintain the symmetry at 400 °C due to limited diffusion rate of oxygen. The diffusion rate becomes measurable above 600 °C for bulk material. In the TEM investigation the thickness of the sample is only about 100 nm, so obvious oxygen loss is observed at 400 °C. At 700 °C the diffusion rate is high enough, and due to oxygen loss the material transforms to cubic structure. Since the cubic symmetry is stabilized by oxygen vacancies, no changes in structure can be expected when cooling down to RT. Orlovskaya et al. [168] reported a reappearance of domains in $LaCoO_3$ after cooling in a TEM chamber, which was not observed in the present experiments with LSCF.

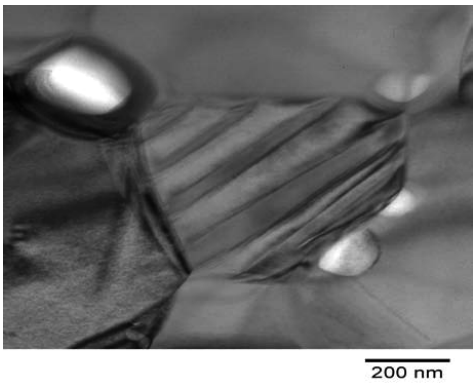

(a) Domains at RT

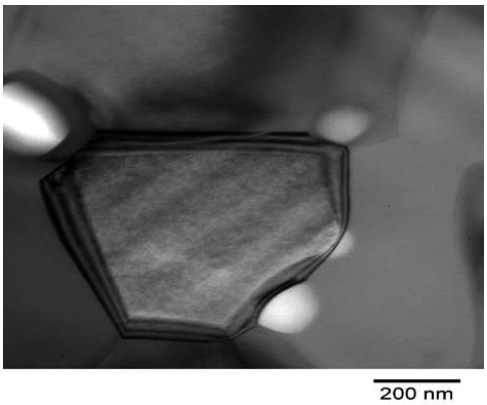

(b) 400 °C

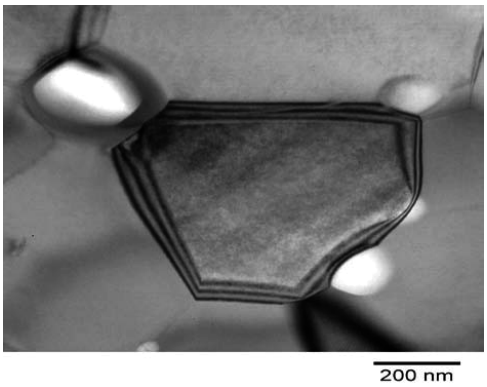

(c) Measured at RT after heated to 400 °C

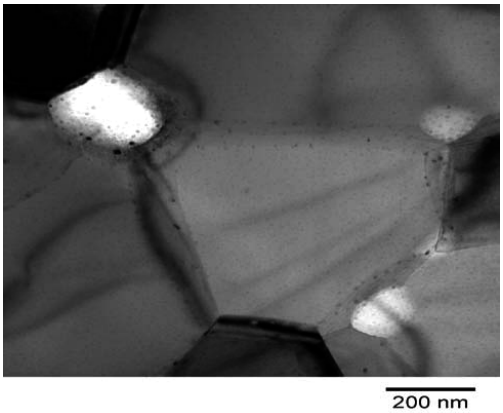

(d) Measured at RT after heated to 700 °C

Figure 3.2.12: In-situ annealing experiment in TEM

3.2.7 Fracture stress

The apparent fracture stress of LSCF measured by ring-on-ring tests was calculated based on the fracture loads using equation (2.1). 5 specimens were used for each temperature, and the standard deviation was given. The value decreases rapidly from RT to 200 °C, and then increases slowly from 200 °C to 700 °C (Figure 3.2.12). Considering the ferro-elasticity and its impact on the non-linear deformation behavior, stress relaxation due to domain formation and switching can be expected. Hence, the measured apparent value of the fracture stress is likely to be higher than the real one. Note that equation (2.1) is only valid for samples that exhibit linear-elastic behavior throughout the test [146]. An estimate of the fracture stress from the non-linear load-displacement curves can be obtained based on the following assumptions: i) the part with the highest slope in the load-displacement curve corresponds to elastic deformation; and ii) any decrease in slope is related with ferro-elastic domain activity.

In general, the stress σ is proportional to the load P and the strain ε is proportional to the deflection d. Although equation (2.1) is not valid in the given non-linear situation, it can still be stated that:

$$\frac{\delta\sigma}{\delta\varepsilon} = \frac{\sigma_a}{K}\frac{\delta P}{\delta d} \tag{3.2.1}$$

where K is the highest slope in the deformation curve, and σ_a is the apparent fracture stress. Multiplication by $\delta\varepsilon$ and integration of both sides leads to a corrected fracture stress σ:

$$\sigma = \frac{\sigma_a}{K}\int\frac{\delta P}{\delta d}\delta\varepsilon \tag{3.2.2}$$

The fracture stresses corrected on the basis of this reasoning are lower than the apparent ones and the decrease in the intermediate temperature range is less pronounced (Figure 3.2.13). The corrected fracture stress decreases by about 13 % from RT to 200 °C, increases slightly up to 700 °C and strongly between 700 °C and 800 °C (67 %).

A very similar effect was reported for $La_{0.5}Sr_{0.5}O_{3-\delta}$ and $La_{0.875}Sr_{0.125}MnO_{3+\delta}$ [111, 181]. The fracture stress of $La_{0.5}Sr_{0.5}O_{3-\delta}$ decreased from RT (80 MPa) to 200 °C (60 MPa) and then increased rapidly up to 800 °C (200 MPa). This effect is attributed to the elimination of the oxygen gradient by lattice diffusion at high temperatures [111]. However, the initial decrease of the fracture stress of LSCF cannot be explained with this assumption, since the elimination of oxygen gradient should increase the fracture stress.

The fracture stress of $La_{0.875}Sr_{0.125}MnO_{3+\delta}$ decreased from RT (164 MPa) to 400 °C (109 MPa), and then increased up to 1000 °C (222 MPa) [111, 181]. A decrease at 400 °C was attributed to the orthorhombic-to-rhombohedral phase transition that occurs in the temperature range of 150 °C - 250 °C. The further increase was associated with the decrease of distortion from cubic symmetry and the oxygen stoichiometry that influenced the oxygen-metal bonding. The fracture stress of $LaFeO_3$ was reported to be higher at 800 °C compared to RT, and the authors related this effect to the relaxation of surface stress at high temperature and toughening due to ferro-elasticity [102].

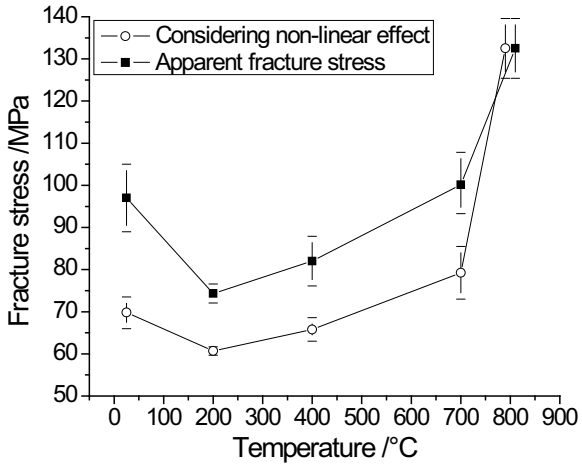

Figure 3.2.13: Fracture stress as a function of temperature in air. The 800 °C data point of the corrected fracture stress is slightly displaced with respect to the temperature scale to enhance visibility

3.2.8 Indentation

3.2.8.1 Temperature dependence

The indentation fracture toughness was determined from the length of indentation cracks. First the applicability of equation (2.3) was examined at RT assuming that K_{ind} should be independent of load for constant fracture toughness, i.e. linearity had to be demonstrated in a $c^{3/2}/P$ plot (see Figure 3.2.14). Efforts to establish the temperature dependence of toughness were again experimentally limited by the heating stage to measurements between RT and 350 °C.

The determined value of indentation fracture toughness (K_{ind} = 0.6 MPa·m$^{1/2}$) remains basically constant from RT to 350 °C (Figure 3.2.15). No effect that might be associated with the ferro-elasticity of the material is recognized. Note that Orlovskaya et al. [182] estimated that an increase in fracture toughness by domain switching alone should be less than 10 %. A small difference in the temperature dependence between fracture toughness and fracture stress can also be caused by different phase constituents in the vicinity of the artificially introduced indentation cracks and failure causing defects (flaws).

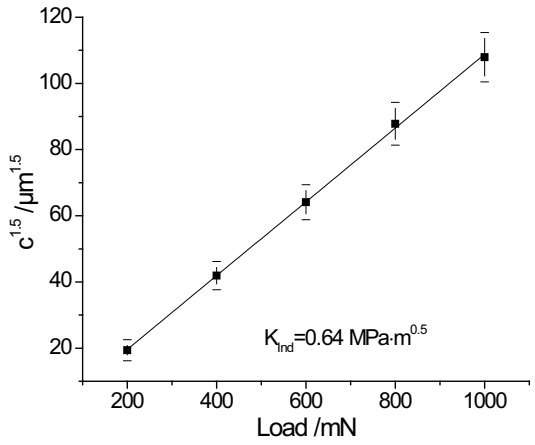

Figure 3.2.14: Indentation crack length in LSCF as a function of indentation load in ambient atmosphere. For each load 36 indentations were applied, and the standard deviation was given.

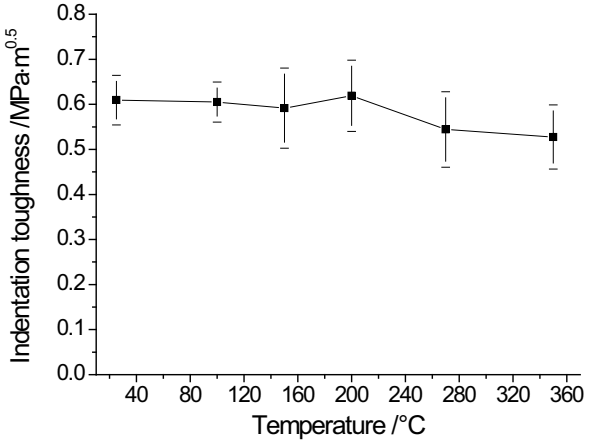

Figure 3.2.15: Indentation fracture toughness of LSCF as a function of temperature in air. For each temperature 36 indentations (600mN) were applied, and the standard deviation was given.

3.2.8.2 Cooling rate dependence

In order to investigate the dependence of Young's modulus and fracture toughness on cooling rate and atmosphere, samples were annealed at 900 °C for 2 hours, and cooled with a rate of 5 K/min. Also one sample was directly taken out of the furnace. The cooling rate of this sample is assumed to be larger than 50 K/min. Young's modulus and indentation toughness were measured by indentation with a load of 1000 mN. The Young's modulus does not really change in the range of cooling rate between 0.5 K/min and 5 K/min within the limits of uncertainty. However, an increase of ~16 % is measured at the very high cooling rate. The Young's modulus of samples annealed under vacuum (10^{-5} mbar) is 136 ± 3 GPa, compared to 75 ± 5 GPa for the same experiment in air. As discussed for the observed phase compositions, the higher value of Young's modulus of samples annealed under vacuum and with high cooling rate is due to the stabilization of the cubic structure down to RT. The fracture toughness exhibits a similar dependence on cooling rate and atmosphere like Young's modulus (Figure 3.2.16 and Fig. 3.2.17).

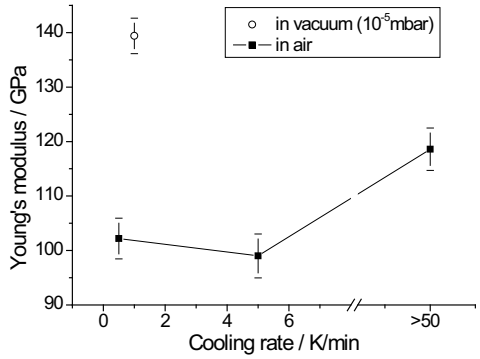

Figure 3.2.16: Dependence of Young's modulus on cooling rate and atmosphere measured at RT (indentation load 1000 mN). For each cooling rate 36 indentations were applied, and the standard deviation was given.

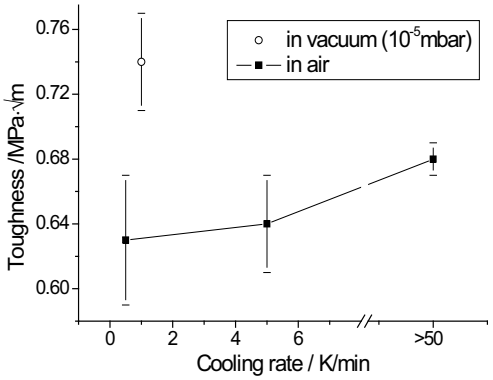

Figure 3.2.17: Dependence of fracture toughness on cooling rate and atmosphere measured at RT (indentation load 1000 mN). For each cooling rate 36 indentations were applied, and the standard deviation was given.

In order to make the obtained thermo-mechanical results comparable, the values of Young's modulus, fracture stress and fracture toughness at various temperatures were normalized with respect to the values of the as-received samples (Figure 3.2.18). The RT values for LSCF are E = 74 ± 4 GPa, σ = 70 ± 4 MPa and K_{ind} = 0.6 ± 0.1 MPa·m$^{0.5}$.

A slight initial decrease in Young's modulus is observed up to 200 °C (Figure 3.2.17), and a strong increase in Young's modulus occurs above 700 °C. The fracture stress of LSCF

decreases by about 10 % from RT to 200 °C, and increases slightly up to 700 °C, and then increases rapidly from 700 °C to 800 °C. The indentation fracture toughness appears to be weakly affected by the temperature. Complementary SEM and TEM investigations after room temperature bending tests revealed the presence of ferro-elastic domains in many grains in the stressed sample surface. Hence the non-linear deformation characteristics obtained for LSCF are related to the ferro-elasticity of this perovskite material [183].

In general, fracture toughness and fracture stress are related by equation (3.1.1) [122]. For RT the average fracture stress of ~70 MPa, with a fracture toughness of 0.64 MPa·√ m thus yields a critical crack length of $c \approx 52$ μm. The value of the crack length is much larger than the grain size (0.6 ± 0.2 μm). The size of defects may change during heating due to thermal expansion, but the relative change in size of such a defect with temperature is expected to be very small. Therefore, it is expected that the normalised values of fracture stress and fracture toughness should show identical behaviour. Indeed the normalized curves of fracture stress and fracture toughness are very close to each other (Figure 3.2.18).

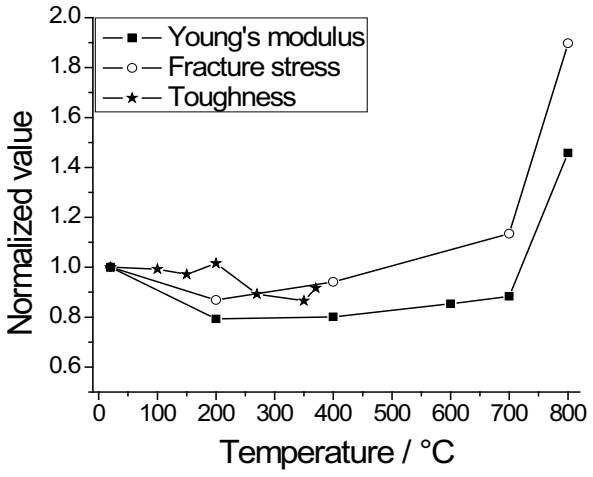

Figure 3.2.18: Thermo-mechanical properties of LSCF. Normalized values of Young's modulus, fracture stress and indentation fracture toughness are plotted (lines are guided to eyes)

3.2.9 Magnetic susceptibility

The magnetic susceptibility of LSCF exhibits the behaviour expected for paramagnetic materials, i.e. a monotonous decrease with increasing temperature (Figure 3.2.19). In a qualitative argument focusing only on Co^{3+}, the absence of spin transition in LSCF could be due to the considerably lower content of Co ions. However, the magnetic susceptibility of BSCF (~ $5 \cdot 10^{-4}$ - $5.9 \cdot 10^{-4}$) is mainly due to Co^{3+}, and the spin transition can be observed from susceptibility measurements. But the magnetic susceptibility of LSCF (~ $1 \cdot 10^{-3}$ - $1.9 \cdot 10^{-3}$), which is much higher than that of BSCF, could be mainly due to La or Fe. Therefore, the spin transition of Co^{3+} in LSCF can be masked by the higher susceptibility of La or Fe. It is not clear whether a spin transition exists in LSCF or not. In fact, a relatively strong decrease of Young's modulus in LSCF was observed from RT to ~ 400 °C.

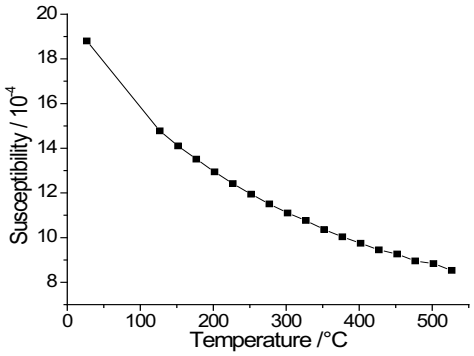

Figure 3.2.19: Magnetic susceptibility of LSCF as a function of temperature in air (lines are guided to eyes)

3.2.10 Residual stresses

In principle internal stresses in perovskite ceramics can be a result of temperature gradients, oxygen gradients and phase transition [101]. In fact, a TEM foil of LSCF prepared normal to the specimen surface by FIB technique showed strong bending effects (Figure 3.2.20), which is a clear indication of internal stresses. Taking the low cooling rate (0.5 K/min) of the specimen

into account, the internal stress is attributed to cubic-rhombohedral transition. The gradual distortion of the rhombohedral from the cubic symmetry increases with deviation from the transition temperature [173]. As a result, internal stresses are generated due to different orientations of the ferro-elastic grains. The resulting local residual stresses are partly compensated by domain formation in the rhombohedral grains. As-received samples show such transformation domains. A significantly higher amount of ferro-elastic domains is observed after applying an additional external stress on the rhombohedral grains (Figure 3.2.10(a)).

The increase of the fracture stress in the range 200 °C - 700 °C might be associated with increasing relaxation of the internal stresses at elevated temperatures. However, above 700 °C the strong increase of the fracture stress has to be attributed to the rhombohedral-cubic phase transition.

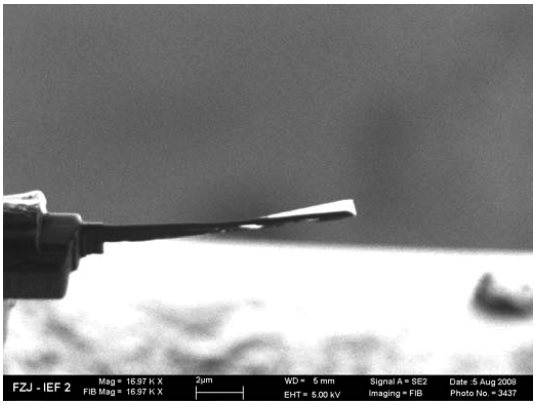

Figure 3.2.20: Bending of LSCF FIB lamella due to residual stresses

3.2.11 Fracture surface

In addition to the residual stress aspects also the micro-structural fracture path undergoes changes as a function of temperature. The fracture surfaces of the specimens tested at various temperatures reveal different fracture modes (Figure 3.2.21). At RT transgranular fracture is observed, while at 200 °C a mixture of ~ 80 % transgranular and 20 % intergranular is pesent. At 700 °C the ratio changes to ~ 15 % transgranular and ~ 85 % intergranular and at 800 °C the

fracture surface is exclusively intergranular. The transition from transgranular to intergranular fracture with increasing temperature indicates that the grain boundaries become weaker compared to the cohesion in the lattice. Traces of domains can be observed as small inclinations on the fracture surfaces in samples tested at 200 °C and 700 °C (Figure 3.2.21), but due to their limited number the hindrance of crack propagation can assumed to be small.

The LSCF transforms from rhombohedral to cubic between 700 °C and 800 °C. In order to investigate the effect of phase composition on the fracture mode, the LSCF sample was annealed under vacuum (10^{-5} mbar) at 900 °C for 2 hours, and cooled at the same P_{O2}. The heating rate and cooling rate were 3 K/min and 1 K/min, respectively. The sample was then fractured at RT (Figure 3.2.21 (e)). The fracture mode is transgranular and comparable with the as-received sample. The result suggests that the change of the fracture mode does not depend on the phase structure but is related to temperature. Grain boundary layers and their softening could play a role. In depth TEM studies that could prove this assumption are out of the scope of the present work.

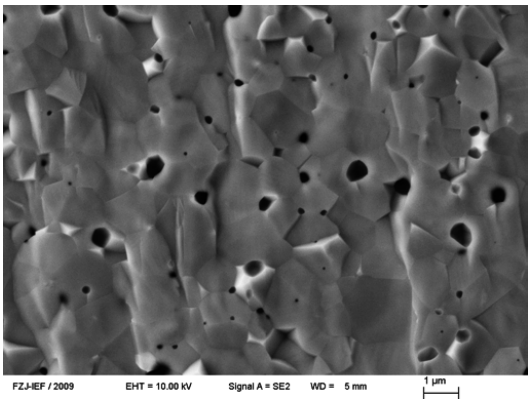

(a) Specimen fractured at RT

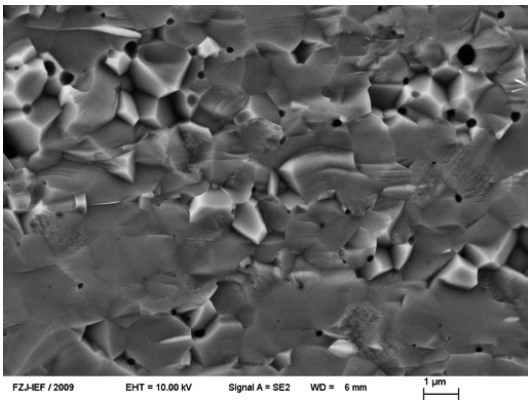

(b) Specimen fractured at 200 °C

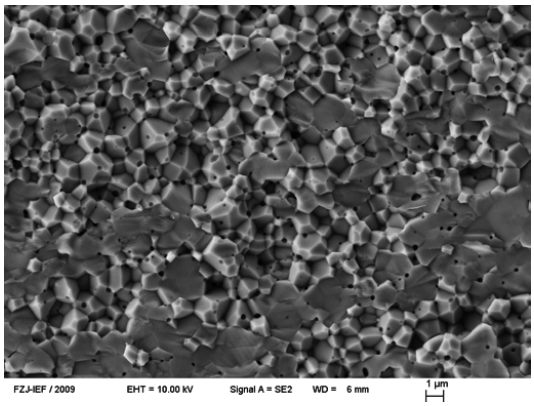

(c) Specimen fractured at 700 °C

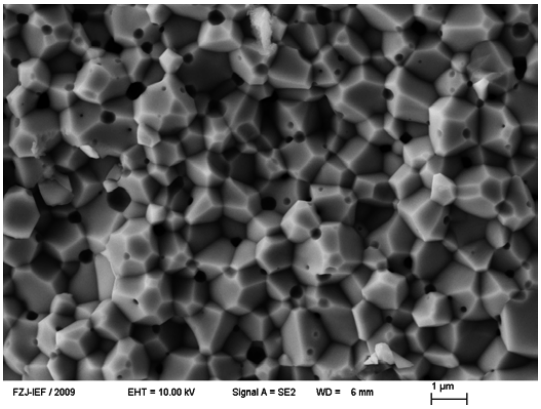

(d) Specimen fractured at 800 °C

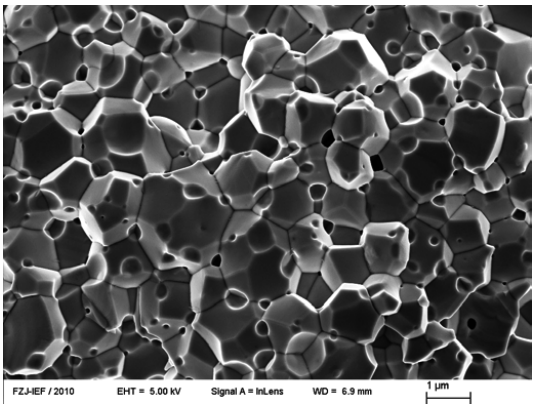

(e) Specimen fractured at 900 °C

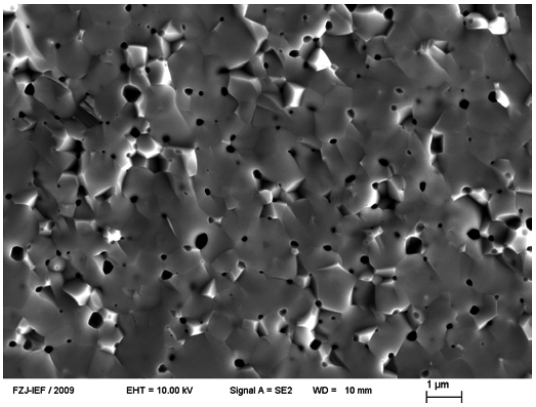

(f) Specimen fractured at RT after annealing and cooling under vacuum (10^{-5} mbar)

Figure 3.2.21: SEM micrographs of LSCF fracture surfaces obtained from ring-on-ring tests at various temperatures

3.2.12 Creep

Typical creep curve is displayed in Figure 3.2.22. It can be seen that the creep rate is high in the initial stage (~ 0 - 3 h), and then comes to a stable value in the following (~ 5 - 20). The steady-state creep rate was calculated by dividing the strain with loading time in the time range of 5 - 20 h.

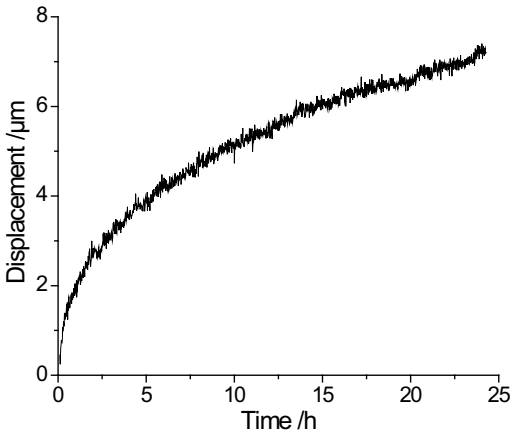

Figure 3.2.22: Typical creep curve of LSCF measured at 800 °C in air. The steady-state creep rate was calculated in the time range of 5 - 20 h.

The steady-state creep rate of LSCF was measured in air and vacuum (10^{-5} mbar) in the temperature range of 700 – 950 °C (Figure 3.2.23). For comparison, creep rates of BSCF measured by Yi et al. are also presented [184]. The Arrhenius plots show an increase of the LSCF creep rate with increasing temperature. The creep rate is almost up to 2 orders of magnitude higher in vacuum than in air for a defined temperature. Interestingly, a transition occurs for LSCF in the temperature range 800 - 850 °C independent of atmosphere, while a transition occurs for BSCF in the temperature range 850 – 900 °C.

The apparent activation energies are compiled in table 3.1. The apparent activation energy of LSCF is about ~ 66 kJ·mol^{-1} in the temperature range of 700 - 800 °C in air, and about 242 kJ·mol^{-1} in vacuum. In the temperature range of 850 - 950 °C the apparent activation energy increases to about 506 - 511 kJ·mol^{-1} for both air and vacuum condition. The value in air is comparable with the activation energy for oxygen transport [21]. The strong increase of the activation energy between 800 – 850 °C may indicate a change of the creep mechanism [185-187].

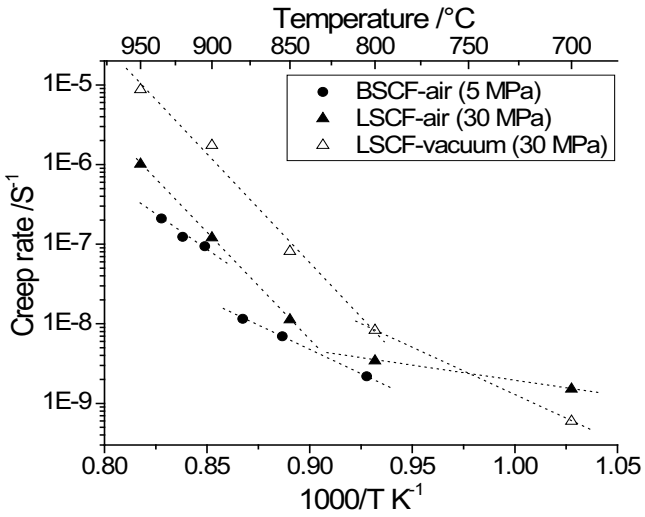

Figure 3.2.23: Steady-state creep rate of LSCF measured in air and vacuum (10^{-5} mbar). For comparison, creep rate of BSCF was displayed [184]

Table 3.1 Apparent activation energies ($kJ \cdot mol^{-1}$) for creep at low and high temperature in air and vacuum (10^{-5} mbar)

	LSCF		BSCF [184]
	air	vacuum	air
Low temperature	~ 66	236 ± 4	~ 258
High temperature	514 ± 3	520 ± 25	~ 287

The apparent activation energy of creep for ceramics is compiled in table 3.2, and the values range from 130 – 990 kJ/mol. For comparison, the apparent activation energy was normalized with respect to RT_m (R is gas constant and T_m is melting point in K). Interestingly, independent of materials, stress and temperature, the creep mechanism is lattice diffusion when the normalized value E/RT_m is larger than 25, and the creep mechanism is grain boundary diffusion when E/RT_m is smaller than 23. This can be explained by that the activation energy of diffusion for atoms is higher in lattice than in grain boundary due to the dense packed structure of the lattice.

Table 3.2 Apparent activation energy for ceramics

Materials	E (kJ/mol)	T (°C)	σ (MPa)	T/T_m	E/RT_m	Creep mechanism
$Bi_2Sr_{1.7}CaCu_2O_x$ [188]	990 ± 190	780 - 835	2 - 3	0.59 - 0.63	67	Lattice
$YAlO_3$ [127]	885 ± 85	1490 - 1600	150	0.82 - 0.88	50	Lattice
$BaTiO_3$ [129]	720 ± 70	1200 - 1300	5	0.78 - 0.83	45.8	Lattice diffusion
$CaTiO_3$ [189]	837	1100 - 1200	4 - 13	0.61 - 0.66	44.8	Lattice diffusion
$La_{0.8}Sr_{0.2}Fe_{0.8}Cr_{0.2}O_{3-\delta}$ [190]	566 ± 16	1100 - 1200	10 - 30	0.76 - 0.82	37.8	Lattice diffusion
$Sr_3Ca_{1.18}Nb_{1.82}O_{9-\delta}$ [191]	670 ± 94	1300 - 1350	40	0.71 - 0.73	36	Lattice
$SrCo_{0.8}Fe_{0.2}O_3$ [192]	471 ± 25	850 - 925	10 - 20	0.71 - 0.76	35.8	Lattice
$SrFeCo_{0.5}O_x$ [193]	453 ± 45	940 - 1000	7	0.79 - 0.83	35.5	Lattice
$La_{0.5}Sr_{0.5}CoO_3$ [194]	619 ± 56	900 - 1050	5 - 28	0.55 - 0.62	35	-
$SrFe_{1.2}Co_{0.3}O_x$ [193]	425 ± 35	940 - 1000	23	0.80 - 0.84	33.8	Lattice
$SrTiO_3$ [195]	620 ± 19	1200 - 1520	15	0.64 - 0.78	32	lattice
$La_{0.8}Sr_{0.2}Ga_{0.85}Mg_{0.15}O_{3-\delta}$ [196]	521 ± 23	1200 - 1300	5 - 20	0.75 - 0.80	32	lattice
$SrZrO_3$ [197]	710 ± 42	1160 - 1275	11	0.49 - 0.53	29.3	Lattice
NaCl [198]	240 ± 10	750 - 795	0.1	0.95 - 0.99	26.9	lattice
$La_{0.9}Sr_{0.1}MnO_3$ [130]	490 ± 30	1150 - 1300	5 - 20	0.65 - 0.72	26.8	Lattice
Bi_2O_3 [199]	230 ± 20	750 - 800	0.5 - 2	0.94 - 0.98	25.3	Lattice
$La_{0.5}Sr_{0.5}Fe_{0.5}Co_{0.5}O_3$ [194]	398 ± 28	900 - 1050	5 - 28	-	-	-
Al_2O_3 [200]	430	1200 - 1300	69	0.63 - 0.68	22.3	Grain boundary
$SrCo_{0.8}Fe_{0.2}O_3$ [192]	275 ± 19	925 - 975	10 - 20	0.76 - 0.79	20.9	Grain boundary
$Ce_{0.9}Gd_{0.1}O_{1.95}$ [201]	480 ± 100	1200 - 1300	5 - 40	0.53 - 0.57	20.8	Grain boundary
$BaZrO_3$ [202]	460 ± 30	1300 - 1400	12	0.53 - 0.56	18.6	Grain boundary
$SrFeO_3$ [128]	260 ± 30	800 - 900	5 - 20	0.63 - 0.75	18.3	Grain boundary
Bi_2O_3 [203]	130	680 - 760	0.3	0.87 - 0.95	14.3	Grain boundary
ZrO_2 [204]	345 ± 15	950 - 1000	25 - 200	0.40 - 0.42	13.7	Grain boundary
$SrFeCo_{0.5}O_x$ [193]	135 ± 27	940 - 1000	3.5	0.79 - 0.83	10.6	Grain boundary
$SrFe_{1.2}Co_{0.3}O_x$ [193]	112 ± 20	940 - 1000	1.9	0.80 - 0.84	8.9	Grain boundary
MgO [205]	204 ± 10	1500 - 1600	5 - 20	0.57 - 0.60	7.9	Grain boundary
SiC [206]	146 ± 25	1300 - 1400	34 - 86	0.52 - 0.56	5.8	Grain boundary
$La_{0.58}Sr_{0.4}Co_{0.2}Fe_{0.8}O_3$ (this work) 	514 ± 3 -	850 - 950 600 - 800	30 30	0.67 - 0.73 -	37.1 -	

The normalized value E/RT_m is plotted as a function of average creep temperature (Figure 3.2.24). When the temperature is below 0.7 T_m, creep mainly occurs by grain boundary diffusion. When the temperature is above 0.7 T_m, creep mainly occurs by lattice diffusion. However, even at high temperature, grain boundary creep could also dominate when the stress is very low. In fact, a transition from low stress to high stress was observed for Bi_2O_3, $SrFeCo_{0.5}O_x$ and $SrFe_{1.2}Co_{0.3}O_x$.

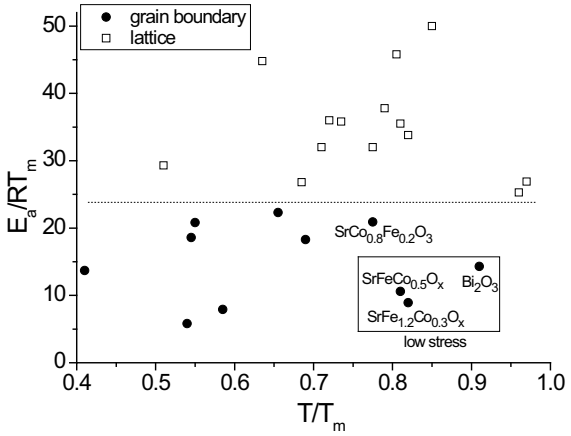

Figure 3.2.24: Normalized activation energy as a function of average creep temperature

LSCF transforms from rhombohedral to cubic between 700 °C and 800 °C in air, while under vacuum (10^{-5} mbar) the cubic structure is stable from high temperature down to RT. Therefore, it seems that the transition in creep is not related with the phase transition. It has been discussed in section 3.1.4.2 that the critical temperature of BSCF is between 800 °C and 850 °C in air.

The partial pressure of oxygen (P_{O2}) contributes to the creep of LSCF with two effects: 1. a decrease of P_{O2} increases the concentration of oxygen vacancies, which enhances the creep effect; 2. the release of oxygen makes the bonding stronger (section 3.2.5), which hinders the creep effect. Therefore, the overall contribution of P_{O2} depends on the competition of the two effects. Majkic et al. [137] have investigated the creep effect of $La_{0.2}Sr_{0.8}Fe_{0.8}Cr_{0.2}O_{3-\delta}$ with respect to P_{O2}. The material exhibits two markedly different behaviors at high and low P_{O2}. At high P_{O2}, the behavior is characterized by the oxygen partial pressure exponent of m = 0.04, followed by a drastic increase in strain rates at low P_{O2}, characterized by m = -0.5. The Young's modulus of LSCF increases rapidly from 700 °C to 800 °C in air due to the phase transition from rhombohedral to cubic, and maintains a higher value throughout the temperature in vacuum. Therefore it is proposed that the lower creep rate of LSCF in vacuum below 700 °C is attributed to the higher Young's modulus in vacuum. Above 800 °C LSCF

exhibits cubic structure both in air and vacuum, and the Young's modulus becomes comparable in both atmospheres, so the higher concentration of oxygen vacancies mainly contributes to the creep effect. Therefore, a higher creep rate is observed in vacuum above 800 °C.

3.3 LNO

3.3.1 Stiffness of LNO

The stiffness of LNO as a function of temperature is shown in Figure 3.3.1. The average stiffness values increase slightly from RT to 800 °C, and decrease rapidly from 800 °C to 900 °C. Furthermore, the stiffness is a moderately higher under vacuum (10^{-5} mbar) than in air at 800 °C. The oxygen deficiency in the material increases with increasing temperature, and is higher under vacuum than in air for a particular temperature [175, 176]. This might be the reason for the higher stiffness value under vacuum. XRD diffraction analyses verified the orthorhombic crystal structure of LNO (Figure 3.3.2). Vashook et al. reported that no significant structure change was observed with in-situ XRD from RT to 1000 °C, whereas Gopalan et al. reported that the orthorhombic structure transforms to tetragonal structure during heating at ~ 400 °C [79, 207]. However the temperature dependence of stiffness, in particular the increase at high temperatures, cannot be explained by a phase transition.

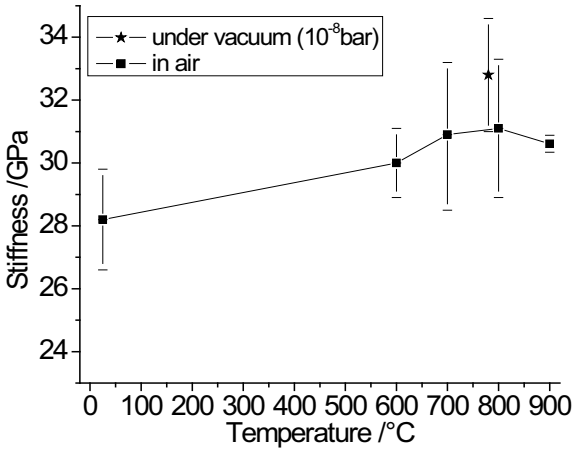

Figure 3.3.1: Stiffness of LNO as a function of temperature and atmosphere. 5 specimens were tested for each temperature, and the standard deviation was given.

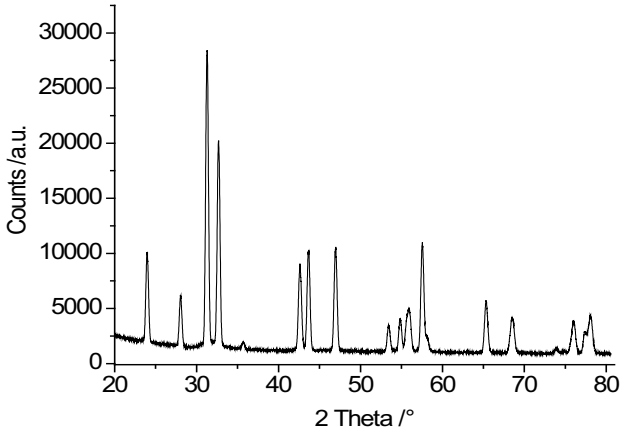

Figure 3.3.2: XRD patterns of LNO

The temperature dependence of stiffness indicates a relation with the oxygen deficiency. The increase of stiffness can be attributed to the change of the bonding property due to the release of oxygen from the lattice. Although up to now, a detailed analysis of the bonding property is not available, it can be assumed that in the lattice two electrons are closely distributed around an oxygen ion due to its higher electro-negativity. When the oxygen is released, the electrons

rearrange in the space between cation and anion, which makes their bonding stronger. The decrease of stiffness from 800 °C to 900 °C might be associated with creep effects.

3.3.2 Fracture stress

The fracture stresses were measured with 4-point bending tests, referring to section 2.2.1. The measured fracture stresses increases slightly from RT to 700 °C, and rises strongly from 700 °C to 900 °C (Figure 3.3.3). Since the measurements were carried out with as-received samples, internal stresses in the sample may have been present related with fast cooling and limitations in oxygen diffusion. The fracture stress could increase with temperature due to the relaxation of the residual stress. To exclude such an effect, the samples were annealed at 800 °C for 2 hours with a heating rate of 4 K/min and a cooling rate of 0.1 K/min. The fracture stress of the annealed samples is ~ 25 % higher than that of as-received samples, and is equal to the fracture stress of samples tested at 600 °C and 700 °C. Therefore, the increase of fracture stress from RT to 700 °C can be attributed to the elimination of residual stresses. Similar to the stiffness the increase of fracture stress from 700 °C to 900 °C might be attributed to the change of bonding property due to oxygen release.

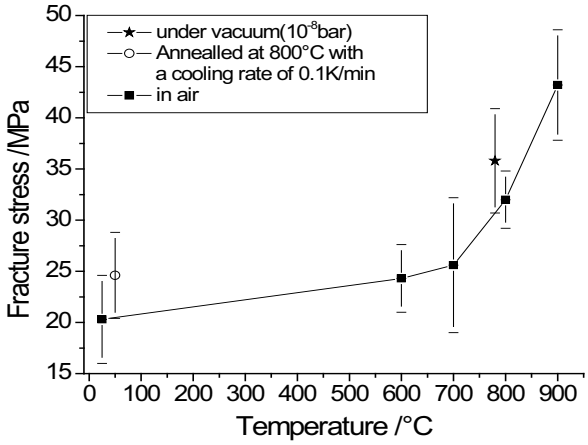

Figure 3.3.3: Fracture stress of LNO as a function of temperature

3.3.3 TG/DTA

The stoichiometry of oxygen was measured with TG, and it is assumed that only oxygen is released during heating. The initial oxygen stoichiometry is supposed to be 4.14 [77-81]. The stoichiometry and DTA curves are shown in Figure 3.3.4. The sample starts to lose oxygen from ~ 400 °C, and the δ-value decreases continuously from this temperature up to 1000 °C. A sharp decrease in the DTA signal was observed at ~ 780 °C, which could be attributed to a change in heat capacity rather than any thermal effect. It could be an indication of a second order phase transition, and this transition may partly be responsible for the increase in fracture stress.

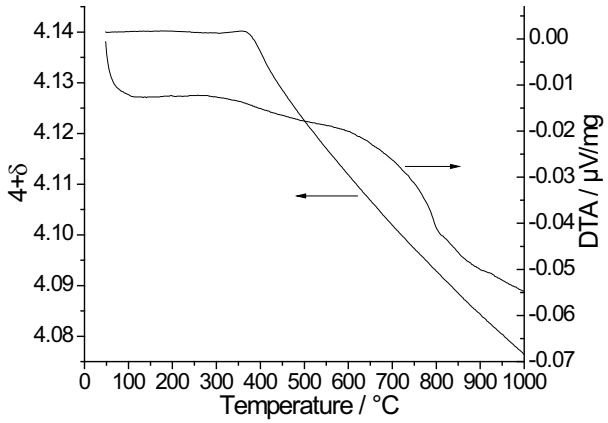

Figure 3.3.4 Differential thermal analysis and oxygen stoichiometry of LNO in air

The thermal expansion coefficient decreases slightly from 50 °C to 300 °C, and then stays stable up to 1000 °C (Figure 3.3.5). The value of TEC is in good agreement with earlier reports [73, 208]. No significant chemical expansion was observed.

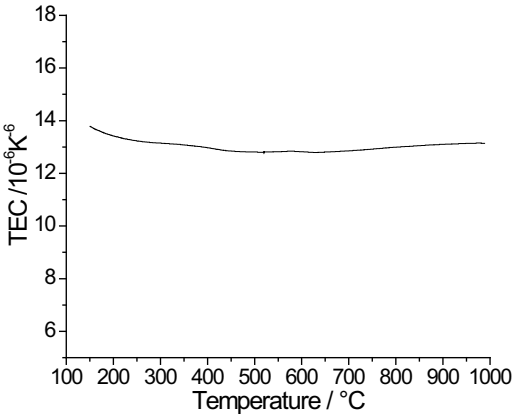

Figure 3.3.5: Thermal expansion coefficient of LNO in air

4. Conclusions

In this section, main conclusions are extracted from the experimental results and the analyses of underlying mechanisms. First the conclusions for BSCF, LSCF and LNO are presented separately. Based on the elaborated thermo-mechanical properties, the three OTM variants are compared. Finally the conclusions focus on the potential for thermo-mechanical application in gas separation components.

4.1 BSCF

BSCF exhibits an anomaly in the Young's modulus between RT and 300 °C (see Figure 3.1.1). The Young's modulus decreases strongly from RT to 200 °C, and rises to a stable value above 300 °C. The fracture stress measured with ring-on-ring tests decreases sharply from RT to 200 °C, and further decreases slightly to 400 °C, and then rises again from 500 °C (see Figure 3.1.3). The fracture surface exhibits from RT to 700 °C an exclusively transgranular failure mode. For samples tested between 700 °C and 800 °C precipitation traces are found along the grain boundaries (see Figure 3.1.14). The anomaly of the Young's modulus has been attributed to a transition of the Co^{3+} spin state (see Figure 3.1.18). Although a hexagonal phase was observed after annealing at 700 – 800 °C for longer time (10 days), BSCF maintains a cubic structure from RT to 300 °C (see Figure 3.1.15 and Figure 3.1.16). Therefore, a phase transition has to be excluded from the possible reasons. An enthalpy change is observed at about 240 °C – 250 °C, which is probably an indication of the association/dissociation of point defects (see Figure 3.1.17). However, the association/dissociation of point defects cannot explain the decrease of the fracture stress and indentation fracture toughness. Moreover, volume changes that are expected to take place as a result of such reactions cannot be observed in the thermal expansion curve (see Figure 3.1.19). Low spin – high spin transition is indicated from magnetic susceptibility measurements. The observed higher value in the α_{sci} curve between RT and 200 °C may also be related to this spin transition. Furthermore, the rapid

increase of α_{sci} from 450 °C to 530 °C is attributed to chemical expansion (see Figure 3.1.19). The indentation fracture toughness decreases from RT to 150 °C, and stays stable up to 350 °C (see Figure 3.1.11).

4.2 LSCF

The phase composition of $La_{0.58}Sr_{0.4}Co_{0.2}Fe_{0.8}O_{3-\delta}$ depends on cooling rate and atmosphere. As determined by XRD, the ratio of cubic to rhombohedral phase increases with increasing cooling rate and decreasing partial pressure of oxygen (see Figure 3.2.7). A purely rhombohedral phase of LSCF was obtained at a low cooling rate of 0.5 K/min in air, and purely cubic phase could be achieved either by quenching in air or annealing under vacuum (10^{-5} mbar) independent of cooling rate. The effect of fast cooling is equivalent to low partial pressure of oxygen, which causes a higher oxygen vacancy concentration in the perovskite due to the low diffusion rate of oxygen. Mechanical integrity could not be sustained during the fast air cooling.

The load-displacement behavior is non-linear between RT and 700 °C, and linear at 800 °C (see Figure 3.2.1). This anomalous effect is attributed to the ferro-elasticity of the rhombohedral phase, which does not exist at high temperature. The micro-structural evidence of domains in the deformed LSCF specimens could be unambiguously confirmed by SEM and TEM observation (see Figure 3.2.10 and Figure 3.2.11). When the sample is heated under in-situ observation to high temperature in the chamber of a TEM, the domains finally disappear due to the transition of the grains from rhombohedral to cubic symmetry (see Figure 3.2.12). The phase composition of LSCF also influences the fracture stress. The fracture stress decreases about 10 % from RT to 200 °C, and increases again from 200 °C to 700 °C reaching values slightly higher than those at RT. Above 750 °C the rhombohedral transforms to cubic symmetry and along with this transition the fracture stress and Young's modulus increase significantly (see Figure 3.2.3 and Figure 3.2.13). The fracture mode changes gradually with the increase in cubic symmetry from transgranular at RT to intergranular at 800 °C (see Figure

3.2.21). The indentation toughness maintains a stable value from RT to 350 °C (see Figure 3.2.15).

4.3 LNO

The mechanical properties of porous LNO samples were measured with 4-point bending tests. The stiffness increases slightly from RT to 800 °C, possibly due to an increase of bonding strength (see Figure 3.3.1). Correspondingly, the fracture stress exhibits similar temperature dependence in this temperature range (see Figure 3.3.3). Oxygen is continuously released from ~ 400 °C up to 1000 °C with increasing temperature, while a sharp decrease in the DTA curve was observed at ~ 780 °C due to the change of heat capacity, which could indicate a second order phase transition (see Figure 3.3.4). The thermal expansion coefficient maintained a stable value from RT up to 1000 °C (see Figure 3.3.5).

4.4 Comparison of BSCF, LSCF and LNO

For use as membranes in power plant application, the materials should exhibit high oxygen conductivity, chemical stability in long term operation, compatibility of thermal expansion with metallic structures, structural stability, and a high resistance to mechanical failure (e.g. fracture stress). However, an OTM material that is superior in all properties is not among the investigated candidates. For practical use one has to find a compromise between different properties, but not necessarily reject an OTM material which often not the optimum in each property. In this thesis mainly thermo-mechanical properties of three OTM materials have been elaborated and compared.

The permeability of BSCF, LSCF and LNO is presented in Figure 1.6. The highest permeability is found in BSCF. BSCF exhibits a relatively high fracture stress and Young's modulus around the proposed operation temperature for gas separation (~ 850 °C), and thus appears in this respect to be suitable for membrane application. However, the observed anomalies in the mechanical properties at intermediate temperatures may cause damage of the

membranes upon temperature transients (Figure 4.1). Therefore, special attention must be given to the heating and cooling process during operation.

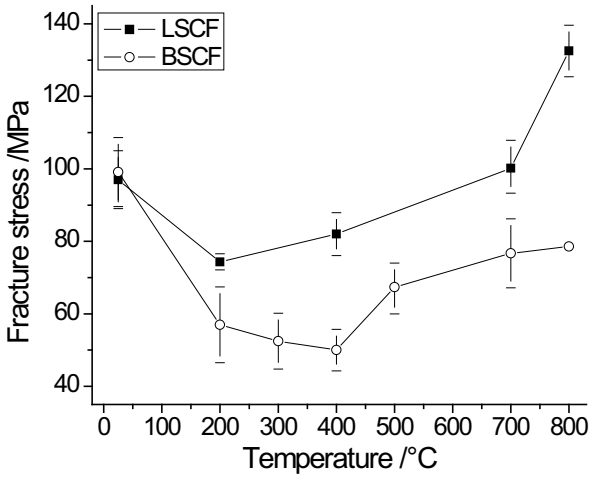

Figure 4.1: Comparison of fracture stresses of BSCF and LSCF at various temperatures, measured using ring-on-ring tests in air.

Also the high value of TEC above 500 °C may cause stresses due to the mismatch of thermal expansion between the membrane and the supporting materials (Figure 4.2). The precipitation of a second phase was observed when operated below 850 °C (see Figure 3.1.16). Since high oxygen permeability was found to sustain over 1000 h at 800 °C operation [87], the second phase does not significantly affect the oxygen permeability. However, BSCF exhibits a limited chemical stability regarding the presence of CO_2 at high temperatures [87]. Chemical stability and oxygen permeability are usually contradictory. The high oxygen permeability implies a weak bonding between oxygen and the cations in the lattice, but at the same time a weak bonding also implies that the material is more prone to react with other species. On the other hand, a chemically stable material means a strong bonding in the material, but a strong bonding would give a low permeability. Therefore, the material used as membrane should exhibit acceptable properties of chemical stability and oxygen permeability.

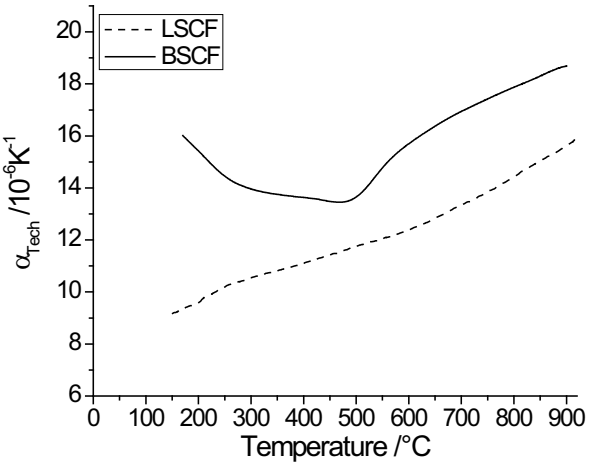

Figure 4.2: Comparison of TEC of BSCF and LSCF in air

The oxygen permeability of LSCF is lower than that of BSCF (see Figure 1.6). But the chemical stability of LSCF is superior to that of BSCF [87]. The mechanical properties are relatively stable from RT to 700 °C. A second order phase transition occurred at 700 °C - 800 °C, and Young's modulus increased about 50 % along with this transition. The impact of mechanical behaviour at the intermediate temperatures on practical membrane application of LSCF appears to be less critical compared to BSCF (Figure 4.1). However, the steep change of Young's modulus from 700 °C to 800 °C may initially generate high stresses at joints between membranes and steel components (Figure 4.3). Although they should relax in this temperature range, a ratcheting effect in case of frequent temperature cycles cannot be excluded.

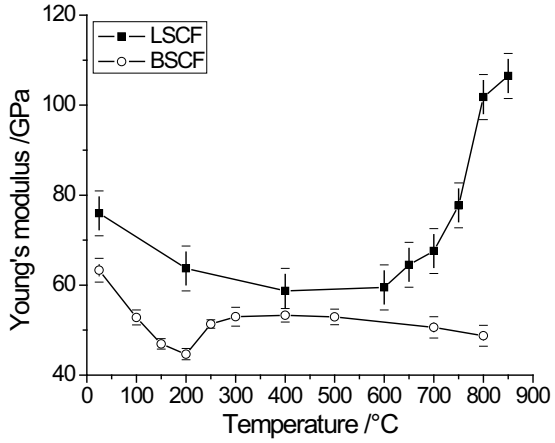

Figure 4.3: Comparison of Young's modulus of BSCF and LSCF, measured using ring-on-ring tests in air.

Finally, the LNO also exhibits lower oxygen permeability than BSCF, but slightly higher than LSCF (see Figure 1.6). The measured thermo-mechanical properties of LNO show advantages compared to those of BSCF and LSCF. The Young's modulus stays relatively stable from RT up to 900 °C, and the fracture stress begins to increase from 600 °C up to 900 °C (see Figure 3.3.3). The TEC maintains a stable value from RT up to 1000 °C (see Figure 3.3.5), implying no severe chemical expansion, which definitely facilitates the design of OTM modules.

References

[1] A. Alexiadis, Ecological Modelling 203 (2007) 243.

[2] A. Baranzini, M. Chesney and J. Morisset, Energy Policy 31 (2003) 691.

[3] L. D. D. Harvey, Energy Policy 21 (1993) 24.

[4] O. Preining, The Science of The Total Environment 126 (1992) 199.

[5] L. Y. Sun and M. H. Wang, Journal of Environmental Management 46 (1996) 327.

[6] K. E. Lonngren and E. W. Bai, Energy Policy 36 (2008) 1567.

[7] R. T. Woodward and R. C. Bishop, Ecological Economics 14 (1995) 101.

[8] P. J. Gellings and H. J. M. Bouwmeester, (CRC-Press, New York, 1997) p. 656.

[9] S. P. S. Badwal and F. T. Ciacchi, Advanced Materials 13 (2001) 993.

[10] J. Sunarso, S. Baumann, J. M. Serra, W. A. Meulenberg, S. Liu, Y. S. Lin and J. C. D. da Costa, Journal of Membrane Science 320 (2008) 13.

[11] A. A. E. Hassan, N. H. Menzler, G. Blass, M. E. Ali, H. P. Buchkremer and D. Stover, Journal of Materials Science 37 (2002) 3467.

[12] S. Ikeda, O. Sakurai, K. Uematsu, N. Mizutani and M. Kato, Journal of Materials Science 20 (1985) 4593.

[13] I. Riess, Solid State Ionics 157 (2003) 1.

[14] S. McIntosh, J. F. Vente, W. G. Haije, D. H. A. Blank and H. J. M. Bouwmeester, Solid State Ionics 177 (2006) 1737.

[15] R. Meyer and R. Waser, Journal of the European Ceramic Society 21 (2001) 1743.

[16] A. S. Bhalla, R. Y. Guo and R. Roy, Materials Research Innovations 4 (2000) 3.

[17] W. Zhou, R. Ran and Z. P. Shao, Journal of Power Sources 192 (2009) 231.

[18] C. Li, K. C. K. Soh and P. Wu, Journal of Alloys and Compounds 372 (2004) 40.

[19] L. W. Tai, M. M. Nasrallah, H. U. Anderson, D. M. Sparlin and S. R. Sehlin, Solid State Ionics 76 (1995) 259.

[20] J. F. Vente, W. G. Haije and Z. S. Rak, Journal of Membrane Science 276 (2006) 178.

[21] Z. P. Shao, W. S. Yang, Y. Cong, H. Dong, J. H. Tong and G. X. Xiong, Journal of Membrane Science 172 (2000) 177.

[22] L. M. Liu, T. H. Lee, L. Qiu, Y. L. Yang and A. J. Jacobson, Materials Research Bulletin 31 (1996) 29.

[23] Y. Teraoka, H. M. Zhang, K. Okamoto and N. Yamazoe, Materials Research Bulletin 23 (1988) 51.

[24] H. Kruidhof, H. J. M. Bouwmeester, R. H. E. Vondoorn and A. J. Burggraaf, Solid State Ionics 63-5 (1993) 816.

[25] Z. Q. Deng, W. S. Yang, W. Liu and C. S. Chen, Journal of Solid State Chemistry 179 (2006) 362.

[26] Y. Ito, R. F. Klie, N. D. Browning and T. J. Mazanec, Journal of the American Ceramic Society 85 (2002) 969.

[27] J. C. Grenier, L. Fournes, M. Pouchard and P. Hagenmuller, Materials Research Bulletin 21 (1986) 441.

[28] J. Rodriguez, J. M. Gonzalezcalbet, J. C. Grenier, J. Pannetier and M. Anne, Solid State Communications 62 (1987) 231.

[29] V. V. Vashook, M. V. Zinkevich and Y. G. Zonov, Solid State Ionics 116 (1999) 129.

[30] J. E. Tenelshof, H. J. M. Bouwmeester and H. Verweij, Applied Catalysis A: General 130 (1995) 195.

[31] L. Qiu, T. H. Lee, L. M. Liu, Y. L. Yang and A. J. Jacobson, Solid State Ionics 76 (1995) 321.

[32] H. H. Wang, Y. Cong and W. S. Yang, Journal of Membrane Science 210 (2002) 259.

[33] J. E. Tenelshof, H. J. M. Bouwmeester and H. Verweij, Solid State Ionics 81 (1995) 97.

[34] T. Ishihara, T. Yamada, H. Arikawa, H. Nishiguchi and Y. Takita, Solid State Ionics 135 (2000) 631.

[35] V. V. Kharton, A. A. Yaremchenko, A. V. Kovalevsky, A. P. Viskup, E. N. Naumovich and P. F. Kerko, Journal of Membrane Science 163 (1999) 307.

[36] Y. Teraoka, T. Nobunaga and N. Yamazoe, Chemistry Letters (1988) 503.

[37] Y. Teraoka, H. M. Zhang, S. Furukawa and N. Yamazoe, Chemistry Letters (1985) 1743.

[38] S. Pei, M. S. Kleefisch, T. P. Kobylinski, J. Faber, C. A. Udovich, V. Zhangmccoy, B. Dabrowski, U. Balachandran, R. L. Mieville and R. B. Poeppel, Catalysis Letters 30 (1995) 201.

[39] Z. P. Shao, G. X. Xiong, J. H. Tong, H. Dong and W. S. Yang, Separation and Purification Technology 25 (2001) 419.

[40] Z. H. Chen, R. Ran, W. Zhou, Z. P. Shao and S. M. Liu, Electrochimica Acta 52 (2007) 7343.

[41] S. Svarcova, K. Wiik, J. Tolchard, H. J. M. Bouwmeester and T. Grande, Solid State Ionics 178 (2008) 1787.

[42] J. Ovenstone, J. I. Jung, J. S. White, D. D. Edwards and S. T. Misture, Journal of Solid State Chemistry 181 (2008) 576.

[43] C. B. Alcock, R. C. Doshi and Y. Shen, Solid State Ionics 51 (1992) 281.

[44] Y. Zeng, Y. S. Lin and S. L. Swartz, Journal of Membrane Science 150 (1998) 87.

[45] J. Mizusaki, T. Sasamoto, W. R. Cannon and H. K. Bowen, Journal of the American Ceramic Society 66 (1983) 247.

[46] S. R. Wang, M. Katsuki, M. Dokiya and T. Hashimoto, Solid State Ionics 159 (2003) 71.

[47] A. Mineshige, J. Izutsu, M. Nakamura, K. Nigaki, J. Abe, M. Kobune, S. Fujii and T. Yazawa, Solid State Ionics 176 (2005) 1145.

[48] L. W. Tai, M. M. Nasrallah, H. U. Anderson, D. M. Sparlin and S. R. Sehlin, Solid State Ionics 76 (1995) 273.

[49] A. Fossdal, M. Menon, I. Waernhus, K. Wiik, M. A. Einarsrud and T. Grande, Journal of the American Ceramic Society 87 (2004) 1952.

[50] B. Wang, B. Zydorczak, Z. T. Wu and K. Li, Journal of Membrane Science 344 (2009) 101.

[51] S. J. Xu and W. J. Thomson, Industrial & Engineering Chemistry Research 37 (1998) 1290.

[52] K. Swierczek, Solid State Ionics 179 (2008) 126.

[53] B. C. H. Steele and J. M. Bae, Solid State Ionics 106 (1998) 255.

[54] C. S. Hsu and B. H. Hwang, Journal of the Electrochemical Society 153 (2006) A1478.

[55] S. J. Benson, D. Waller and J. A. Kilner, Journal of the Electrochemical Society 146 (1999) 1305.

[56] E. Bakken, N. L. Allan, T. H. K. Barron, C. E. Mohn, I. T. Todorov and S. Stolen, Physical Chemistry Chemical Physics 5 (2003) 2237.

[57] R. D. Shannon, Acta Crystallographica Section A 32 (1976) 751.

[58] H. L. Lein, K. Wiik and T. Grande, Solid State Ionics 177 (2006) 1795.

[59] B. X. Huang, J. Malzbender, R. W. Steinbrech and L. Singheiser, Solid State Ionics 180 (2009) 241.

[60] J. C. Grenier, N. Ea, M. Pouchard and P. Hagenmuller, Journal of Solid State Chemistry 58 (1985) 243.

[61] K. Hilpert, R. W. Steinbrech, F. Boroomand, E. Wessel, F. Meschke, A. Zuev, O. Teller, H. Nickel and L. Singheiser, Journal of the European Ceramic Society 23 (2003) 3009.

[62] C. S. Montross, Journal of the European Ceramic Society 18 (1998) 353.

[63] K. Aizu, Journal of the Physical Society of Japan 27 (1969) 387.

[64] E. K. Salje, Phase Transitions in Ferroelastic and Co-elastic Crystals (University of Cambridge, Cambridge, 1993).

[65] P. Müllner and W. M. Kriven, Journal of Materials Research 12 (1997) 1771.

[66] K. Kleveland, N. Orlovskaya, T. Grande, A. M. M. Moe, M. A. Einarsrud, K. Breder and G. Gogotsi, Journal of the American Ceramic Society 84 (2001) 2029.

[67] Y. Liu, X. Tan and K. Li, Catalysis Reviews 48 (2006) 145.

[68] S. M. Liu and G. R. Gavalas, Journal of Membrane Science 246 (2005) 103.

[69] J. W. Stevenson, T. R. Armstrong, R. D. Carneim, L. R. Pederson and W. J. Weber, Journal of the Electrochemical Society 143 (1996) 2722.

[70] N. Miura, Y. Okamoto, J. Tamaki, K. Morinaga and N. Yamazoe, Solid State Ionics 79 (1995) 195.

[71] K. Li, X. Y. Tan and Y. T. Liu, Journal of Membrane Science 272 (2006) 1.

[72] C. Y. Tsai, A. G. Dixon, Y. H. Ma, W. R. Moser and M. R. Pascucci, Journal of the American Ceramic Society 81 (1998) 1437.

[73] E. V. Tsipis, E. N. Naumovich, A. L. Shaula, M. V. Patrakeev, J. C. Waerenborgh and V. V. Kharton, Solid State Ionics 179 (2008) 57.

[74] E. N. Naumovich, M. V. Patrakeev, V. V. Kharton, A. A. Yaremchenko, D. I. Lopinovich and F. M. B. Marques, Solid State Sciences 7 (2005) 1353.

[75] V. V. Kharton, A. A. Yaremchenko and E. N. Naumovich, Journal of Solid State Electrochemistry 3 (1999) 303.

[76] L. Minervini, R. W. Grimes, J. A. Kilner and K. E. Sickafus, Journal of Materials Chemistry 10 (2000) 2349.

[77] D. E. Rice and D. J. Buttrey, Journal of Solid State Chemistry 105 (1993) 197.

[78] H. Kanai, J. Mizusaki, H. Tagawa, S. Hoshiyama, K. Hirano, K. Fujita, M. Tezuka and T. Hashimoto, Journal of Solid State Chemistry 131 (1997) 150.

[79] V. V. Vashook, S. P. Tolochko, L. Yushkevich, L. V. Makhnach, I. F. Kononyuk, H. Altenburg, J. Hauck and H. Ullmann, Solid State Ionics 110 (1998) 245.

[80] V. V. Vashook, I. I. Yushkevich, L. V. Kokhanovsky, L. V. Makhnach, S. P. Tolochko, I. F. Kononyuk, H. Ullmann and H. Altenburg, Solid State Ionics 119 (1999) 23.

[81] H. Tamura, A. Hayashi and Y. Ueda, Physica C 216 (1993) 83.

[82] V. V. Kharton, A. V. Kovalevsky, M. Avdeev, E. V. Tsipis, M. V. Patrakeev, A. A. Yaremchenko, E. N. Naumovich and J. R. Frade, Chemistry of Materials 19 (2007) 2027.

[83] T. Ishihara, K. Nakashima, S. Okada, M. Enoki and H. Matsumoto, Solid State Ionics 179 (2008) 1367.

[84] S. Miyoshi, T. Furuno, H. Matsumoto and T. Ishihara, Solid State Ionics 177 (2006) 2269.

[85] V. V. Kharton, A. P. Viskup, A. V. Kovalevsky, E. N. Naumovich and F. M. B. Marques, Solid State Ionics 143 (2001) 337.

[86] S. Ziesche, R. Jurk, N. Trofimenko and M. Kusnezoff, Solid State Ionics 179 (2008) 1351.

[87] D. Schlehuber, Sauerstofftransport und Degradationsverhalten von Hochtemperatur-membranen für CO2-freie Kraftwerke, in "Faculty of Mechanical Engineering" (RWTH Aachen, Aachen, 2010).

[88] C. Kittel, Introduction to Solid State Physics (John Wiley & Sons, New York, 2004).

[89] S. B. Adler, Journal of the American Ceramic Society 84 (2001) 2117.

[90] Q. S. Zhu, T. A. Jin and Y. Wang, Solid State Ionics 177 (2006) 1199.

[91] R. Kriegel, R. Kircheisen and J. Töpfer, Solid State Ionics 181 (2010) 64.

[92] T. R. Armstrong, J. W. Stevenson, L. R. Pederson and P. E. Raney, Journal of the Electrochemical Society 143 (1996) 2919.

[93] V. V. Kharton, A. A. Yaremchenko, M. V. Patrakeev, E. N. Naumovich and F. M. B. Marques, Journal of the European Ceramic Society 23 (2003) 1417.

[94] P. M. Raccah and Goodenou.Jb, Physical Review 155 (1967) 932.

[95] K. Asai, A. Yoneda, O. Yokokura, J. M. Tranquada and G. Shirane, Journal of the Physical Society of Japan 67 (1998) 290.

[96] P. G. Radaelli and S. W. Cheong, Physical Review B 66 (2002) 094408.

[97] K. Knížek, Z. Jirák, J. Hejtmánek, M. Veverka, M. Maryško, G. Maris and T. T. M. Palstra, The European Physical Journal B 47 (2005) 213.

[98] R. Mahendiran and A. K. Raychaudhuri, Physical Review B 54 (1996) 16044.

[99] H. L. Lein, O. S. Andersen, P. E. Vullum, E. Lara-Curzio, R. Holmestad, M. A. Einarsrud and T. Grande, Journal of Solid State Electrochemistry 10 (2006) 635.

[100] I. Lubomirsky, Solid State Ionics 177 (2006) 1639.

[101] A. Atkinson and A. Selcuk, Solid State Ionics 134 (2000) 59.

[102] A. Fossdal, M. A. Einarsrud and T. Grande, Journal of the European Ceramic Society 25 (2005) 927.

[103] N. Orlovskaya, K. Kleveland, T. Grande and M. A. Einarsrud, Journal of the European Ceramic Society 20 (2000) 51.

[104] N. Orlovskaya, M. Lugovy, S. Pathak, D. Steinmetz, J. Lloyd, L. Fegely, M. Radovic, E. A. Payzant, E. Lara-Curzio, L. F. Allard and J. Kuebler, Journal of Power Sources 182 (2008) 230.

[105] Y. S. Chou, J. W. Stevenson, T. R. Armstrong and L. R. Pederson, Journal of the American Ceramic Society 83 (2000) 1457.

[106] N. M. Sammes, R. Ratnaraj and M. G. Fee, Journal of Materials Science 29 (1994) 4319.

[107] S. W. Paulik, S. Baskaran and T. R. Armstrong, Journal of Materials Science 33 (1998) 2397.

[108] N. Nagendra and S. Bandopadhyay, Scripta Materialia 48 (2003) 37.

[109] Y. S. Chou, K. Kerstetter, L. R. Pederson and R. E. Williford, Journal of Materials Research 16 (2001) 3545.

[110] N. M. Sammes and R. Ratnaraj, Journal of Materials Science 32 (1997) 687.

[111] D. L. Meixner and R. A. Cutler, Solid State Ionics 146 (2002) 273.

[112] C. M. D'Souza and N. M. Sammes, J. Am. Ceram. Soc. 83 (2000) 47.

[113] C. S. Montross, H. Yokokawa, M. Dokiya and L. Bekessy, Journal of the American Ceramic Society 78 (1995) 1869.

[114] J. Drennan, V. Zelizko, D. Hay, F. T. Ciacchi, S. Rajendran and S. P. S. Badwal, Journal of Materials Chemistry 7 (1997) 79.

[115] N. M. Sammes, F. M. Keppeler, H. Nafe and F. Aldinger, Journal of the American Ceramic Society 81 (1998) 3104.

[116] K. J. deVries, Solid State Ionics 100 (1997) 193.

[117] S. Baskaran, C. A. Lewinsohn, Y. S. Chou, M. Qian, J. W. Stevenson and T. R. Armstrong, Journal of Materials Science 34 (1999) 3913.

[118] D. Dierickx, I. Houben, J. Lapin, F. Delannay and O. VanDerBiest, Journal of Materials Science Letters 15 (1996) 1573.

[119] K. C. Goretta, E. T. Park, R. E. Koritala, M. M. Cuber, E. A. Pascual, N. Chen, A. R. d. Arellano-López and J. L. Routbort, Physica C 309 (1998) 245.

[120] S. Yamanaka, T. Maekawa, H. Muta, T. Matsuda, S. Kobayashi and K. Kurosaki, Journal of Alloys and Compounds 381 (2004) 295.

[121] A. Julian, E. Juste, P. M. Geffroy, N. Tessier-Doyen, P. Del Gallo, N. Richet and T. Chartier, Journal of the European Ceramic Society 29 (2009) 2603.

[122] J. B. Watchman, Mechanical Properties of Ceramics (Wiley & Sons, New York, 1996).

[123] R. L. Coble, Journal of Applied Physics 34 (1963) 1679.

[124] C. Herring, Journal of Applied Physics 21 (1950) 437.

[125] J. N. Wang, Acta Materialia 48 (2000) 1517.

[126] M. E. Kassner and T. A. Hayes, International Journal of Plasticity 19 (2003) 1715.

[127] Z. C. Wang, C. Dupas-Bruzek and S. Karato, Physics of the Earth and Planetary Interiors 110 (1999) 51.

[128] K. Kleveland, A. Wereszczak, T. P. Kirkland, M. A. Einarsrud and T. Grande, Journal of the American Ceramic Society 84 (2001) 1822.

[129] E. T. Park, P. Nash, J. Wolfenstine, K. C. Goretta and J. L. Routbort, Journal of Materials Research 14 (1999) 523.

[130] J. Wolfenstine, T. R. Armstrong, W. J. Weber, M. A. BolingRisser, K. C. Goretta and J. L. Routbort, Journal of Materials Research 11 (1996) 657.

[131] W. E. Luecke and T. R. Armstrong, Journal of Materials Research 17 (2002) 532.

[132] J. Wolfenstine, P. Huang and A. Petric, Journal of the Electrochemical Society 147 (2000) 1668.

[133] H. L. Lein, K. Wiik, M. A. Einarsrud and T. Grande, Journal of the American Ceramic Society 89 (2006) 2895.

[134] G. Majkic, L. Wheeler and K. Salama, Acta Materialia 48 (2000) 1907.

[135] G. Majkic, L. T. Wheeler and K. Salama, Solid State Ionics 146 (2002) 393.

[136] J. L. Routbort, K. C. Goretta, R. E. Cook and J. Wolfenstine, Solid State Ionics 129 (2000) 53.

[137] G. Majkic, L. T. Wheeler and K. Salama, Solid State Ionics 164 (2003) 137.

[138] H. Yamada, Journal of Materials Science 19 (1984) 2639.

[139] K. C. Goretta, E. T. Park, J. Guan, U. Balachandran, S. E. Dorris and J. L. Routbort, Solid State Ionics 111 (1998) 295.

[140] C. H. Chen, H. J. M. Bouwmeester, R. H. E. vanDoorn, H. Kruidhof and A. J. Burggraaf, Solid State Ionics 98 (1997) 7.

[141] A. L. Shaula, V. V. Kharton, F. M. B. Marques, A. V. Kovalevsky, A. P. Viskup and E. N. Naumovich, Journal of Solid State Electrochemistry 10 (2006) 13.

[142] S. J. Xu and W. J. Thomson, Chemical Engineering Science 54 (1999) 3839.

[143] P. Kountouros, R. Förthmann, A. Naoumidis, G. Stochniol and E. Syskakis, Ionics 1 (1995) 40.

[144] H. Fessler and D. C. Fricker, Journal of the American Ceramic Society 67 (1984) 582.

[145] T. Fett, G. Rizzi, J. P. Guin and S. M. Wiederhorn, Journal of Materials Science 42 (2007) 393.

[146] ASTM C 1499-05.

[147] R. W. Schmitt and G. Schönbrunn, Sprechsaal 116 (1983) 387.

[148] W. C. Oliver and G. M. Pharr, Journal of Materials Research 7 (1992) 1564.

[149] J. Malzbender, J. M. J. d. Toonder, A. R. Balkenende and G. d. With, Materials Science and Engineering: R: Reports 36 (2002) 47.

[150] D. B. Marshall and B. R. Lawn, Journal of the American Ceramic Society 60 (1977) 86.

[151] E. Manika and J. Maniks, Acta Materialia 54 (2006) 2049.

[152] G. P. Upit and Varcheny.Sa, Phys Status Solidi 17 (1966) 831.

[153] W. W. Gerberich, N. I. Tymiak, J. C. Grunlan, M. F. Horstemeyer and M. I. Baskes, Journal of Applied Mechanics 69 (2002) 433.

[154] W. D. Nix and H. J. Gao, Journal of the Mechanics and Physics of Solids 46 (1998) 411.

[155] J. Y. Shu and N. A. Fleck, International Journal of Solids and Structures 35 (1998) 1363.

[156] H. Gao, Y. Huang, W. D. Nix and J. W. Hutchinson, Journal of the Mechanics and Physics of Solids 47 (1999) 1239.

[157] N. Gane and J. M. Cox, Philos Mag 22 (1970) 881.

[158] H. Li, A. Ghosh, Y. H. Han and R. C. Bradt, Journal of Materials Research 8 (1993) 1028.

[159] G. Farges and D. Degout, Thin Solid Films 181 (1989) 365.

[160] K. W. McElhaney, J. J. Vlassak and W. D. Nix, Journal of Materials Research 13 (1998) 1300.

[161] L. Hong and R. C. Bradt, J Non-Cryst Solids 146 (1992) 197.

[162] F. Q. Yang, J. Y. Y. Zhou, V. Kordonski and S. D. Jacobs, Journal of Materials Science Letters 15 (1996) 1523.

[163] Z. Hashin and S. Shtrikman, Journal of the Mechanics and Physics of Solids 11 (1963) 127.

[164] R. Chaim and M. Hefetz, Journal of Materials Science 39 (2004) 3057.

[165] B. X. Huang, J. Malzbender, R. W. Steinbrech, P. Grychtol, C. M. Schneider and L. Singheiser, Applied Physics Letters 95 (2009) 051901.

[166] R. J. Harrison, S. A. T. Redfern and E. K. H. Salje, Physical Review B 69 (2004) 144101.

[167] M. Greenberg, E. Wachtel, I. Lubomirsky, J. Fleig and J. Maier, Advanced Functional Materials 16 (2006) 48.

[168] N. Orlovskaya, N. Browning and A. Nicholls, Acta Materialia 51 (2003) 5063.

[169] S. Murata, S. Isida, M. Suzuki, Y. Kobayashi, K. Asai and K. Kohn, Physica B-Condensed Matter 263 (1999) 647.

[170] L. Minervini, M. O. Zacate and R. W. Grimes, Solid State Ionics 116 (1999) 339.

[171] C. Garrod, Statistical Mechanics and Thermodynamics (Oxford University Press, Oxford, 1995).

[172] S. V. Chavan, M. D. Mathews and A. K. Tyagi, Journal of the American Ceramic Society 87 (2004) 1977.

[173] A. Mineshige, M. Inaba, T. S. Yao, Z. Ogumi, K. Kikuchi and M. Kawase, Journal of Solid State Chemistry 121 (1996) 423.

[174] A. I. Becerro, C. McCammon, F. Langenhorst, F. Seifert and R. Angel, Phase Transitions 69 (1999) 133.

[175] D. Mantzavinos, A. Hartley, I. S. Metcalfe and M. Sahibzada, Solid State Ionics 134 (2000) 103.

[176] T. Nakamura, G. Petzow and L. J. Gauckler, Materials Research Bulletin 14 (1979) 649.

[177] M. A. Alariofranco, J. M. Gonzalezcalbet, M. Valletregi and J. C. Grenier, Journal of Solid State Chemistry 49 (1983) 219.

[178] J. M. Gonzalezcalbet, M. Parras, M. Valletregi and J. C. Grenier, Journal of Solid State Chemistry 86 (1990) 149.

[179] J. Zinn-Justin, Phase Transitions and Renormalization Group (Oxford University Press, Oxford, 2007).

[180] P. Gumbsch, S. Taeri-Baghbadrani, D. Brunner, W. Sigle and A. Ruhle, Physical Review Letters 87 (2001) 085505.

[181] C. M. D'Souza and N. M. Sammes, Journal of the American Ceramic Society 83 (2000) 47.

[182] N. Orlovskaya, Y. Gogotsi, M. Reece, B. L. Cheng and I. Gibson, Acta Materialia 50 (2002) 715.

[183] M. Radovic and E. Lara-Curzio, Acta Materialia 52 (2004) 5747.

[184] J. X. Yi, H. L. Lein, T. Grande, S. Yakovlev and H. J. M. Bouwmeester, Solid State Ionics 180 (2009) 1564.

[185] M. Palcut, K. Wiik and T. Grande, The Journal of Physical Chemistry B 111 (2007) 2299.

[186] M. Palcut, K. Wiik and T. Grande, The Journal of Physical Chemistry C 111 (2007) 813.

[187] J. B. Smith and T. Norby, Journal of the Electrochemical Society 153 (2006) A233.

[188] J. L. Routbort, K. C. Goretta, D. J. Miller, D. B. Kazelas, C. Clauss and A. Dominguezrodriguez, Journal of Materials Research 7 (1992) 2360.

[189] H. Yamada, Journal of Materials Science 19 (1984) 2639.

[190] G. Majkic, L. T. Wheeler and K. Salama, Solid State Ionics 146 (2002) 393.

[191] M. J. López-Robledo, A. R. de Arellano-López, J. Martínez-Fernández and A. Sayir, Solid State Ionics 178 (2007) 207.

[192] G. Majkic, L. Wheeler and K. Salama, Acta Materialia 48 (2000) 1907.

[193] A. R. de Arellano-López, U. Balachandran, K. C. Goretta, B. Ma and J. L. Routbort, Acta Materialia 49 (2001) 3109.

[194] H. L. Lein, K. Wiik, M.-A. Einarsrud, T. Grande and E. Lara-Curzio, J. Am. Ceram. Soc. 89 (2006) 2895.

[195] Z. C. Wang, S. Karato and K. Fujino, Physics of the Earth and Planetary Interiors 79 (1993) 299.

[196] J. Wolfenstine, Solid State Ionics 126 (1999) 293.

[197] J. Nemeth and J. G. Parr, Journal of the American Ceramic Society 55 (1972) 125.

[198] J. P. Poirier, Philosophical Magazine 26 (1972) 701.

[199] A. Vilette and S. L. Kampe, Journal of Materials Research 11 (1996) 1433.

[200] R. M. Cannon, W. H. Rhodes and A. H. Heuer, Journal of the American Ceramic Society 63 (1980) 46.

[201] J. L. Routbort, K. C. Goretta, A. R. de Arellano-López and J. Wolfenstine, Scripta Materialia 38 (1997) 315.

[202] K. C. Goretta, E. T. Park, R. E. Koritala, M. M. Cuber, E. A. Pascual, N. Chen, A. R. de Arellano-López and J. L. Routbort, Physica C: Superconductivity 309 (1998) 245.

[203] J. L. Grabowski and D. C. Dunand, Scripta Materialia 43 (2000) 1033.

[204] M. J. Roddy, W. R. Cannon, G. Skandan and H. Hahn, Journal of the European Ceramic Society 22 (2002) 2657.

[205] D. Yang and H. Conrad, Journal of Materials Science 37 (2002) 615.

[206] V. Krishnamachari and M. R. Notis, Materials Science and Engineering 27 (1977) 83.

[207] P. Gopalan, M. W. Mcelfresh, Z. Kakol, J. Spalek and J. M. Honig, Physical Review B 45 (1992) 249.

[208] S. J. Skinner, Solid State Sciences 5 (2003) 419.

List of Figures

Figure 1.1: Schematic representation of possible separation processes in fossil power plants

Figure 1.2: Schematic representation of the transport process of oxygen through a membrane with different oxygen partial pressure P_{O2}'>P_{O2}'' on both surfaces

Figure 1.3: Atomic structure of perovskite, (a) Transition metal ion (B) cube centered, (b) Rear earth metal ion (A) cube centered

Figure 1.4: Pseudobinary phase diagram for the $La_{1-x}Sr_xFeO_{3-\delta}$ system ($x \leq 0.75$) in air

Figure 1.5: Atomic structure of LNO

Figure 1.6: Dependence of oxygen flux of LSCF, BSCF und $La_2NiO_{4+\delta}$ on temperature

Figure 1.7: Potential energy as a function of bond length

Figure 1.8: Contribution of chemical expansion to the thermal expansion

Figure 1.9: Thermal expansion behaviour of $Ba_xSr_{1-x}Co_{0.8}Fe_{0.2}O_{3-\delta}$ in air

Figure 1.10: The cubic lattice constant of $La_{0.5}Sr_{0.5}Fe_{0.5}Co_{0.5}O_{3-\delta}$ (LSFC55) and $La_{0.5}Sr_{0.5}CoO_{3-\delta}$ (LSC) as a function of temperature in air and in nitrogen atmosphere. The solid and dashed lines are guides to the eye. The squares are the pseudo cubic lattice constant in air obtained from a rhombohedral model

Figure 1.11: Thermal expansion behaviour of $La_{0.4}Sr_{0.6}Co_{0.2}Fe_{0.8}O_{3-\delta}$ in air

Figure 1.12: Lattice constant of $La_{0.6}Sr_{0.4}Fe_{0.2}Co_{0.8}O_{3-\delta}$ as a function of oxygen partial pressure (P_0 = 1 atm)

Figure 1.13: Schematic diagram of Co^{3+} spin transition in perovskites

Figure 1.14: Fracture toughness of perovskites as a function of temperature

Figure 1.15: Dependence of Young's modulus of perovskite materials on temperature

Figure 1.16: Schematic representation of creep, (a) Three stages of creep process in tension. I) primary II) secondary III) tertiary, (b) Three stages of creep process in compression. I) primary II) secondary III) tertiary

Figure 2.1: Schematic representation of ring-on-ring test, (a) Overview, (b) Cross section

Figure 2.2: Typical load-displacement curves of indentation

Figure 2.3: Impression of indentation, (a) Optical microscopy image of indentation impression, (b) schematic indentation impression

Figure 2.4: Investigated LNO samples, (a) Photo of the LNO samples, (b) Cross section of the LNO sample

Figure 3.1.1: Young's modulus of BSCF measured in ring-on-ring bending test as a function of temperature and P_{O2} (air and 10^{-5} mbar). The Young's modulus expected for 'normal' ceramics (dotted line) is displayed for comparison.

Figure 3.1.2: Young's modulus measured with ring-on-ring test and dynamic resonance frequency method in air (data provided by IMCE, Belgium)

Figure 3.1.3: Fracture stress of BSCF measured with ring-on-ring bending test as a function of temperature in air

Figure 3.1.4: Impression of indentation, (a) SEM micrograph of BSCF with Vickers impression (600mN) and indentation cracks, (b) Magnified bottom corner of the impression

Figure 3.1.5: Young's modulus of BSCF measured by indentation as a function of loading force in ambient atmosphere. For each load 36 indentations were applied, and the standard deviation was given.

Figure 3.1.6: Hardness of BSCF measured by indentation as a function of loading force in ambient atmosphere. For each load 36 indentations were applied, and the standard deviation was given.

Figure 3.1.7: Crack length as a function of indentation load in ambient atmosphere. For each load 36 indentations were applied, and the standard deviation was given.

Figure 3.1.8: Young's modulus as a function of cooling rate measured in ambient atmosphere. For each cooling rate 36 indentations were applied, and the standard deviation was given.

Figure 3.1.9: Fracture toughness as a function of cooling rate measured in ambient atmosphere. For each cooling rate 36 indentations were applied, and the standard deviation was given.

Figure 3.1.10: Young's modulus, hardness and fracture toughness through the thickness of BSCF specimens annealed in dual atmosphere (air/2 mbar)

Figure 3.1.11: Indentation fracture toughness of BSCF as a function of temperature in air

Figure 3.1.12: Slip traces of BSCF around indentation impression observed by TEM and SEM, (a) Slip traces around indentation impression (600 mN). Optical micrograph of impression performed at 260 °C, (b) Slip traces around indentation impression observed by SEM, (c) Lamella of FIB cutting, (d) TEM micrograph of Slip traces indexed as (111) planes, (e) Diffraction patterns by TEM

Figure 3.1.13: Normalized values of the stiffness, fracture stress and indentation fracture toughness

Figure 3.1.14: Fracture surfaces of BSCF specimens tested at various temperatures, (a) RT, (b) 200 °C, (c) 400 °C, (d) 500 °C, (e) 700 °C, (f) 800 °C, (g) 900 °C

Figure 3.1.15: XRD results of BSCF annealed at various temperatures

Figure 3.1.16: Optical micrographs of samples annealed at various temperature, (a) 750 °C for 336 hours, (b) 800 °C for 336 hours, (c) 850 °C for 336 hours, (d) 900 °C for 336 hours, (e) 950 °C for 336 hours

Figure 3.1.17: Differential thermal analysis (DTA) curve of BSCF in air

Figure 3.1.18: Magnetic susceptibility of BSCF as a function of temperature in air

Figure 3.1.19: Thermal expansion behavior of BSCF, (a) Thermal expansion, (b) α_{Sci} (solid line) and α_{Tech} (dotted line)

Figure 3.1.20: Thermal gravity (TG) curves of BSCF

Figure 3.2.1: Typical load-displacement curves of LSCF at various temperatures in air. The first deviation of the slope from linearity is indicated by circles (○), and the saturation point is indicated by rectangles (□) . The samples fractured at the end of the curves.

Figure 3.2.2: Temperature dependence of onset and saturation load of domain switching in LSCF

Figure 3.2.3: Young's modulus of LSCF as a function of temperature measured by ring-on-ring test and resonance method. For ring-on-ring tests, 5 measurements were carried out for each temperature, and the standard deviations were given.

Figure 3.2.4: Young's modulus of LSCF under vacuum (10^{-5} mbar). The average value was calculated from 5 measurements, and the standard deviation was given.

Figure 3.2.5: Young's modulus, hardness and fracture toughness through the thickness (1 mm) of a LSCF sample exposed to a gradient in P_{O2}

Figure 3.2.6: In-situ high-temperature XRD patterns of LSCF

Figure 3.2.7: Room temperature XRD diffraction patterns of LSCF samples after different heat treatments. After annealing at 900 °C various cooling rates in air and under vacuum (10^{-5} mbar) were applied.

Figure 3.2.8: TG and DTA curves of LSCF measured in air with a heating rate of 2 K/min

Figure 3.2.9: Thermal expansion and thermal expansion coefficient of LSCF in air

Figure 3.2.10: SEM micrographs of ferro-elastic domains in deformed LSCF sample, (a) Overview, (b) Within a single grain

Figure 3.2.11: TEM micrograph of ferro-elastic domains in deformed LSCF sample

Figure 3.2.12: In-situ annealing experiment in TEM, (a) Domains at RT, (b) 400 °C, (c) Measured at RT after heated to 400 °C, (d) Measured at RT after heated to 700 °C

Figure 3.2.13: Fracture stress of LSCF as a function of temperature in air. The 800 °C data point of the corrected fracture stress is slightly displaced with respect to the temperature scale to enhance visibility

Figure 3.2.14: Indentation crack length in LSCF as a function of indentation load in ambient atmosphere. For each load 36 indentations were applied, and the standard deviation was given.

Figure 3.2.15: Indentation fracture toughness of LSCF as a function of temperature in air. For each temperature 36 indentations (600mN) were applied, and the standard deviation was given.

Figure 3.2.16: Dependence of Young's modulus on cooling rate and atmosphere measured at RT (indentation load 1000 mN). For each cooling rate 36 indentations were applied, and the standard deviation was given.

Figure 3.2.17: Dependence of fracture toughness on cooling rate and atmosphere measured at RT (indentation load 1000 mN). For each cooling rate 36 indentations were applied, and the standard deviation was given.

Figure 3.2.18: Thermo-mechanical properties of LSCF. Normalized values of the Young's modulus, fracture stress and indentation fracture toughness are plotted (lines are guided to eyes)

Figure 3.2.19: Magnetic susceptibility of LSCF as a function of temperature in air (lines are guided to eyes)

Figure 3.2.20: Bending of LSCF FIB lamella due to residual stresses

Figure 3.2.21: SEM micrographs of LSCF fracture surfaces obtained from ring-on-ring tests at various temperatures, (a) Specimen fractured at RT, (b) Specimen fractured at 200 °C, (c) Specimen fractured at 700 °C, (d) Specimen fractured at 800 °C, (e) Specimen fractured at 900 °C, (f) Specimen fractured at RT after annealing and cooling under vacuum (10^{-5}mbar)

Figure 3.2.22: Typical creep curve of LSCF measured at 800 °C in air. The steady-state creep rate was calculated in the time range of 5 - 20 h.

Figure 3.2.23: Steady-state creep rate of LSCF measured in air and vacuum (10^{-5} mbar). For comparison, creep rate of BSCF was displayed

Figure 3.2.24: Normalized activation energy as a function of average creep temperature

Figure 3.3.1: Stiffness of LNO as a function of temperature and atmosphere. 5 specimens were tested for each temperature, and the standard deviation was given.

Figure 3.3.2: XRD patterns of LNO

Figure 3.3.3: Fracture stress of LNO as a function of temperature

Figure 3.3.4: Differential thermal analysis and oxygen stoichiometry of LNO in air

Figure 3.3.5: Thermal expansion coefficient of LNO in air

Figure 4.1: Comparison of fracture stresses of BSCF and LSCF at various temperatures, measured using ring-on-ring tests in air.

Figure 4.2: Comparison of TEC of BSCF and LSCF in air

Figure 4.3: Comparison of Young's modulus of BSCF and LSCF, measured using ring-on-ring tests in air.

List of Tables

Table 1.1: Oxygen permeation flux data for perovskite structure membranes

Table 1.2: Oxygen permeation flux data for K_2NiF_4 structured membranes

Table 1.3: Chemical expansions for different compositions

Table 1.4: Fracture stresses of perovskite materials at various temperatures

Table 1.5: Fracture toughness of perovskite materials at various temperatures

Table 1.6: Young's modulus of perovskite materials at various temperatures

Table 1.7: Creep rates at 1200 °C in air and 5 MPa load for different compositions

Table 3.1: The apparent activation energy for creep at low and high temperature in air and vacuum (10^{-5} mbar)

Nomenclature

Acronyms

MIEC	mixed ionic-electronic conducting
OTM	oxygen transport membrane
SOFC	solid state fuel cell
BSCF	$Ba_{0.5}Sr_{0.5}Co_{0.8}Fe_{0.2}O_{3-\delta}$
LSCF	$La_{0.58}Sr_{0.4}Co_{0.8}Fe_{0.2}O_{3-\delta}$
LNO	$La_2NiO_{4+\delta}$
LSFC55	$La_{0.5}Sr_{0.5}Fe_{0.5}Co_{0.5}O_{3-\delta}$
LSC	$La_{0.5}Sr_{0.5}CoO_{3-\delta}$
TEC	thermal expansion coefficient
SENB	single edge notched beam
SEVNB	single edge V notched beam
RT	room temperature
atm	ambient atmosphere
DTA	differential thermal analysis
TG	thermogravimetry
XRD	X-ray diffraction
SEM	scanning electron microscopy
TEM	transmission electron microscopy
FIB	focused ion beam
LS	low spin
HS	high spin
ISE	indentation size effect
PPMS	Physical Property Measurement System

Latin symbols

ABO_3	the type of perovskite oxides
R_A	radius of rear earth metal ion in the perovskite [m]
R_B	radius of transition metal ion in the perovskite [m]
R_O	radius of oxygen ion in the perovskite [m]
a	lattice constant of the perovskite [m]
t	tolerance factor of the perovskite
T	temperature [°C or K]
L	specimen length measured at a given temperature T [m]
r_0	equilibrium bond length [m]
r	bond length [m]
H_{IT}	indentation hardness [MPa]
F_m	maximum load of Indentation [m]
A_P	projection area of indentation impression [m^2]
E_{IT}	indentation elastic modulus [GPa]
E_r	Reduced modulus [GPa]
E_i	elastic modulus of indenter [GPa]
K_{Ind}	indentation fracture toughness [MPa·√m]
T_m	absolute melting temperature [K]
P_{O2}	partial pressure of oxygen [atm]
E_a	activation energy [$kJ \cdot mol^{-1}$]
R	gas constant [$J \cdot mol^{-1} \cdot K^{-1}$]
P	applied force of ring-on-ring test [N]
t_h	specimen thickness [m]
R_1	radius of the loading ring [m]
R_2	radius of the supporting ring [m]
R_3	radius of the LSCF or BSCF specimen [m]

I	moment of inertial [m^4]
w	width of LNO specimen [m]
h	height of LNO specimen [m]
h_1	height of 2 compartments in the LNO specimen [m]
w_1	width of a compartment in the LNO specimen [m]
M	moment [N·m]
L_s	support pin distance in 4 point bending test [m]
l_s	load pin distance in 4 point bending test [m]
H	enthalpy [J]
G	Gibbs energy [J]
S	entropy [$J \cdot K^{-1}$]
T_e	reaction temperature without external stress [K]
d_e	central deflection of the specimen [m]
n_1	density of magnetic moments [m^{-3}]

Greek symbols

β	indenter constant
δ	oxygen non-stoichiometry
α_{Tech}	technical thermal expansion coefficient [K^{-1}]
α_{Sci}	scientific thermal expansion coefficient [K^{-1}]
σ	flexure stress of ring-on-ring test [MPa]
v	poisson ratio
v_s	poisson's ratio of sample
v_i	poisson's ratio of indenter
χ	magnetic susceptibility
ε_t	total strain
ε_r	reaction strain
ε_c	chemical expansion

Acknowledgements

First of all I would like to thank Professor L. Singheiser for offering me a doctoral thesis in the exciting field of oxygen transport membranes and for his continuous support of the work in the Institute of Energy Research (IEF-2), Forschungszentrum Jülich.

I gratefully acknowledge my supervisor, Dr. R. W. Steinbrech, for his valuable instructions and encouragements during the past three years. I have learnt a lot from him not only in science but also in working style. My sincere thanks are also given to Dr. J. Malzbender, who helped me throughout the whole thesis with experimental advice and in-depth theoretical discussions. I am grateful to Professor T. Beck for supervising my thesis and defense.

I would like to acknowledge my colleagues from IEF-1 and the other in membrane projects participating institutes for continuous support and useful discussions.

I would like to express my gratitude to Mr. J. Mönch, Ms. T. Osipova and Ms. X. Yang for the technical support, Mrs. M. Lipinska-Chwalek and Mr. B. Rutkowski for valuable discussions. Dr. W. Meulenberg and Dr. S. Baumann from IEF-1 for providing the BSCF and LSCF samples. My special thanks for the experimental support to Dr. A. Möbius and Dr. T. Markus for TG/DTA measurements, Dr. H. J. Penkalla for TEM characterization, Dr. E. Wessel for the SEM work, Mr. P. Grychtol and Professor C. M. Schneider for the susceptibility measurements. Moreover, the invaluable support by XRD characterization provided by Dr. W. Fischer is highly appreciated.

The work was funded by the German Ministry of Economics and Technology within the frame of the project OXYMEM.

List of publications

1. Mechanical properties of $La_{0.58}Sr_{0.4}Co_{0.2}Fe_{0.8}O_{3-\delta}$ membranes, B. X. Huang, J. Malzbender, R. W. Steinbrech, L. Singheiser, Solid State Ionics 180 (2009) 241-245
2. Anomalies in the thermomechanical behavior of $Ba_{0.5}Sr_{0.5}Co_{0.8}Fe_{0.2}O_{3-\delta}$ ceramic oxygen conductive membranes at intermediate temperatures, B. X. Huang, J. Malzbender, R. W. Steinbrech, P. Grychtol, C. M. Schneider, L. Singheiser, Applied Physics Letters 95 (2009) 051901
3. Discussion of the complex thermo-mechanical behavior of $Ba_{0.5}Sr_{0.5}Co_{0.8}Fe_{0.2}O_{3-\delta}$, B.X. Huang, J. Malzbender, R.W. Steinbrech, L. Singheiser, Journal of Membrane Science, 359 [1-2] (2010) 80-85
4. Mechanical aspects of ferro-elastic behavior and phase composition of $La_{0.58}Sr_{0.4}Co_{0.2}Fe_{0.8}O_{3-\delta}$, B.X. Huang, J. Malzbender, R.W. Steinbrech, E. Wessel, H.J. Penkalla, L. Singheiser, Journal of Membrane Science, 349 [1-2] (2010) 183-188
5. A comparison of results obtained using different methods to assess the elastic properties of ceramic materials exemplified for $Ba_{0.5}Sr_{0.5}Co_{0.8}Fe_{0.2}O_{3-\delta}$, J. Malzbender, B. Huang, J. Mönch, R. W. Steinbrech, Journal of Materials Science, 45 [5] (2010) 1227-1230

1. **Einsatz von multispektralen Satellitenbilddaten in der Wasserhaushalts- und Stoffstrommodellierung – dargestellt am Beispiel des Rureinzugsgebietes**
   von C. Montzka (2008), XX, 238 Seiten
   ISBN: 978-3-89336-508-1

2. **Ozone Production in the Atmosphere Simulation Chamber SAPHIR**
   by C. A. Richter (2008), XIV, 147 pages
   ISBN: 978-3-89336-513-5

3. **Entwicklung neuer Schutz- und Kontaktierungsschichten für Hochtemperatur-Brennstoffzellen**
   von T. Kiefer (2008), 138 Seiten
   ISBN: 978-3-89336-514-2

4. **Optimierung der Reflektivität keramischer Wärmedämmschichten aus Yttrium-teilstabilisiertem Zirkoniumdioxid für den Einsatz auf metallischen Komponenten in Gasturbinen**
   von A. Stuke (2008), X, 201 Seiten
   ISBN: 978-3-89336-515-9

5. **Lichtstreuende Oberflächen, Schichten und Schichtsysteme zur Verbesserung der Lichteinkopplung in Silizium-Dünnschichtsolarzellen**
   von M. Berginski (2008), XV, 171 Seiten
   ISBN: 978-3-89336-516-6

6. **Politikszenarien für den Klimaschutz IV – Szenarien bis 2030**
   hrsg.von P. Markewitz, F. Chr. Matthes (2008), 376 Seiten
   ISBN 978-3-89336-518-0

7. **Untersuchungen zum Verschmutzungsverhalten rheinischer Braunkohlen in Kohledampferzeugern**
   von A. Schlüter (2008), 164 Seiten
   ISBN 978-3-89336-524-1

8. **Inorganic Microporous Membranes for Gas Separation in Fossil Fuel Power Plants**
   by G. van der Donk (2008), VI, 120 pages
   ISBN: 978-3-89336-525-8

9. **Sinterung von Zirkoniumdioxid-Elektrolyten im Mehrlagenverbund der oxidkeramischen Brennstoffzelle (SOFC)**
   von R. Mücke (2008), VI, 165 Seiten
   ISBN: 978-3-89336-529-6

10. **Safety Considerations on Liquid Hydrogen**
    by K. Verfondern (2008), VIII, 167 pages
    ISBN: 978-3-89336-530-2

11. **Kerosinreformierung für Luftfahrtanwendungen**
von R. C. Samsun (2008), VII, 218 Seiten
ISBN: 978-3-89336-531-9

12. **Der 4. Deutsche Wasserstoff Congress 2008 – Tagungsband**
hrsg. von D. Stolten, B. Emonts, Th. Grube (2008), 269 Seiten
ISBN: 978-3-89336-533-3

13. **Organic matter in Late Devonian sediments as an indicator for environmental changes**
by M. Kloppisch (2008), XII, 188 pages
ISBN: 978-3-89336-534-0

14. **Entschwefelung von Mitteldestillaten für die Anwendung in mobilen Brennstoffzellen-Systemen**
von J. Latz (2008), XII, 215 Seiten
ISBN: 978-3-89336-535-7

15. **RED-IMPACT**
Impact of Partitioning, Transmutation and Waste Reduction Technologies on the Final Nuclear Waste Disposal
SYNTHESIS REPORT
ed. by W. von Lensa, R. Nabbi, M. Rossbach (2008), 178 pages
ISBN 978-3-89336-538-8

16. **Ferritic Steel Interconnectors and their Interactions with Ni Base Anodes in Solid Oxide Fuel Cells (SOFC)**
by J. H. Froitzheim (2008), 169 pages
ISBN: 978-3-89336-540-1

17. **Integrated Modelling of Nutrients in Selected River Basins of Turkey**
Results of a bilateral German-Turkish Research Project
project coord. M. Karpuzcu, F. Wendland (2008), XVI, 183 pages
ISBN: 978-3-89336-541-8

18. **Isotopengeochemische Studien zur klimatischen Ausprägung der Jüngeren Dryas in terrestrischen Archiven Eurasiens**
von J. Parplies (2008), XI, 155 Seiten, Anh.
ISBN: 978-3-89336-542-5

19. **Untersuchungen zur Klimavariabilität auf dem Tibetischen Plateau - Ein Beitrag auf der Basis stabiler Kohlenstoff- und Sauerstoffisotope in Jahrringen von Bäumen waldgrenznaher Standorte**
von J. Griessinger (2008), XIII, 172 Seiten
ISBN: 978-3-89336-544-9

20. **Neutron-Irradiation + Helium Hardening & Embrittlement Modeling of 9%Cr-Steels in an Engineering Perspective (HELENA)**
by R. Chaouadi (2008), VIII, 139 pages
ISBN: 978-3-89336-545-6

21. **in Bearbeitung**

22. **Verbundvorhaben APAWAGS (AOEV und Wassergenerierung) – Teilprojekt: Brennstoffreformierung – Schlussbericht**
von R. Peters, R. C. Samsun, J. Pasel, Z. Porš, D. Stolten (2008), VI, 106 Seiten
ISBN: 978-3-89336-547-0

23. **FREEVAL**
Evaluation of a Fire Radiative Power Product derived from Meteosat 8/9 and Identification of Operational User Needs
Final Report
project coord. M. Schultz, M. Wooster (2008), 139 pages
ISBN: 978-3-89336-549-4

24. **Untersuchungen zum Alkaliverhalten unter Oxycoal-Bedingungen**
von C. Weber (2008), VII, 143, XII Seiten
ISBN: 978-3-89336-551-7

25. **Grundlegende Untersuchungen zur Freisetzung von Spurstoffen, Heißgaschemie, Korrosionsbeständigkeit keramischer Werkstoffe und Alkalirückhaltung in der Druckkohlenstaubfeuerung**
von M. Müller (2008), 207 Seiten
ISBN: 978-3-89336-552-4

26. **Analytik von ozoninduzierten phenolischen Sekundärmetaboliten in *Nicotiana tabacum* L. cv Bel W3 mittels LC-MS**
von I. Koch (2008), III, V, 153 Seiten
ISBN 978-3-89336-553-1

27. **IEF-3 Report 2009. Grundlagenforschung für die Anwendung**
(2009), ca. 230 Seiten
ISBN: 978-3-89336-554-8

28. **Influence of Composition and Processing in the Oxidation Behavior of MCrAlY-Coatings for TBC Applications**
by J. Toscano (2009), 168 pages
ISBN: 978-3-89336-556-2

29. **Modellgestützte Analyse signifikanter Phosphorbelastungen in hessischen Oberflächengewässern aus diffusen und punktuellen Quellen**
von B. Tetzlaff (2009), 149 Seiten
ISBN: 978-3-89336-557-9

30. **Nickelreaktivlot / Oxidkeramik – Fügungen als elektrisch isolierende Dichtungskonzepte für Hochtemperatur-Brennstoffzellen-Stacks**
von S. Zügner (2009), 136 Seiten
ISBN: 978-3-89336-558-6

31. **Langzeitbeobachtung der Dosisbelastung der Bevölkerung in radioaktiv kontaminierten Gebieten Weißrusslands – Korma-Studie**
von H. Dederichs, J. Pillath, B. Heuel-Fabianek, P. Hill, R. Lennartz (2009), Getr. Pag.
ISBN: 978-3-89336-532-3

32. **Herstellung von Hochtemperatur-Brennstoffzellen über physikalische Gasphasenabscheidung**
von N. Jordán Escalona (2009), 148 Seiten
ISBN: 978-3-89336-532-3

33. **Real-time Digital Control of Plasma Position and Shape on the TEXTOR Tokamak**
by M. Mitri (2009), IV, 128 pages
ISBN: 978-3-89336-567-8

34. **Freisetzung und Einbindung von Alkalimetallverbindungen in kohlebefeuerten Kombikraftwerken**
von M. Müller (2009), 155 Seiten
ISBN: 978-3-89336-568-5

35. **Kosten von Brennstoffzellensystemen auf Massenbasis in Abhängigkeit von der Absatzmenge**
von J. Werhahn (2009), 242 Seiten
ISBN: 978-3-89336-569-2

36. **Einfluss von Reoxidationszyklen auf die Betriebsfestigkeit von anodengestützten Festoxid-Brennstoffzellen**
von M. Ettler (2009), 138 Seiten
ISBN: 978-3-89336-570-8

37. **Großflächige Plasmaabscheidung von mikrokristallinem Silizium für mikromorphe Dünnschichtsolarmodule**
von T. Kilper (2009), XVII, 154 Seiten
ISBN: 978-3-89336-572-2

38. **Generalized detailed balance theory of solar cells**
by T. Kirchartz (2009), IV, 198 pages
ISBN: 978-3-89336-573-9

39. **The Influence of the Dynamic Ergodic Divertor on the Radial Electric Field at the Tokamak TEXTOR**
von J. W. Coenen (2009), xii, 122, XXVI pages
ISBN: 978-3-89336-574-6

40. **Sicherheitstechnik im Wandel Nuklearer Systeme**
von K. Nünighoff (2009), viii, 215 Seiten
ISBN: 978-3-89336-578-4

41. **Pulvermetallurgie hochporöser NiTi-Legierungen für Implanat- und Dämpfungsanwendungen**
von M. Köhl (2009), XVII, 199 Seiten
ISBN: 978-3-89336-580-7

42. **Einfluss der Bondcoatzusammensetzung und Herstellungsparameter auf die Lebensdauer von Wärmedämmschichten bei zyklischer Temperaturbelastung**
von M. Subanovic (2009), 188, VI Seiten
ISBN: 978-3-89336-582-1

43. **Oxygen Permeation and Thermo-Chemical Stability of Oxygen Permeation Membrane Materials for the Oxyfuel Process**
by A. J. Ellett (2009), 176 pages
ISBN: 978-3-89336-581-4

44. **Korrosion von polykristallinem Aluminiumoxid (PCA) durch Metalljodidschmelzen sowie deren Benetzungseigenschaften**
von S. C. Fischer (2009), 148 Seiten
ISBN: 978-3-89336-584-5

45. **IEF-3 Report 2009. Basic Research for Applications**
(2009), 217 Seiten
ISBN: 978-3-89336-585-2

46. **Verbundvorhaben ELBASYS (Elektrische Basissysteme in einem CFK-Rumpf) - Teilprojekt: Brennstoffzellenabgase zur Tankinertisierung - Schlussbericht**
von R. Peters, J. Latz, J. Pasel, R. C. Samsun, D. Stolten
(2009), xi, 202 Seiten
ISBN: 978-3-89336-587-6

47. **Aging of ^{14}C-labeled Atrazine Residues in Soil: Location, Characterization and Biological Accessibility**
by N. D. Jablonowski (2009), IX, 104 pages
ISBN: 978-3-89336-588-3

48. **Entwicklung eines energetischen Sanierungsmodells für den europäischen Wohngebäudesektor unter dem Aspekt der Erstellung von Szenarien für Energie- und CO_2 - Einsparpotenziale bis 2030**
von P. Hansen (2009), XXII, 281 Seiten
ISBN: 978-3-89336-590-6

49. **Reduktion der Chromfreisetzung aus metallischen Interkonnektoren für Hochtemperaturbrennstofzellen durch Schutzschichtsysteme**
von R. Trebbels (2009), iii, 135 Seiten
ISBN: 978-3-89336-591-3

50. **Bruchmechanische Untersuchung von Metall / Keramik-Verbundsystemen für die Anwendung in der Hochtemperaturbrennstoffzelle**
von B. Kuhn (2009), 118 Seiten
ISBN: 978-3-89336-592-0

51. **Wasserstoff-Emissionen und ihre Auswirkungen auf den arktischen Ozonverlust**
Risikoanalyse einer globalen Wasserstoffwirtschaft
von T. Feck (2009), 180 Seiten
ISBN: 978-3-89336-593-7

52. **Development of a new Online Method for Compound Specific Measurements of Organic Aerosols**
by T. Hohaus (2009), 156 pages
ISBN: 978-3-89336-596-8

53. **Entwicklung einer FPGA basierten Ansteuerungselektronik für Justageeinheiten im Michelson Interferometer**
von H. Nöldgen (2009), 121 Seiten
ISBN: 978-3-89336-599-9

54. **Observation – and model – based study of the extratropical UT/LS**
by A. Kunz (2010), xii, 120, xii pages
ISBN: 978-3-89336-603-3

55. **Herstellung polykristalliner Szintillatoren für die Positronen-Emissions-Tomographie (PET)**
von S. K. Karim (2010), VIII, 154 Seiten
ISBN: 978-3-89336-610-1

56. **Kombination eines Gebäudekondensators mit H2-Rekombinatorelementen in Leichwasserreaktoren**
von S. Kelm (2010), vii, 119 Seiten
ISBN: 978-3-89336-611-8

57. **Plant Leaf Motion Estimation Using A 5D Affine Optical Flow Model**
by T. Schuchert (2010), X, 143 pages
ISBN: 978-3-89336-613-2

58. **Tracer-tracer relations as a tool for research on polar ozone loss**
by R. Müller (2010), 116 pages
ISBN: 978-3-89336-614-9

59. **Sorption of polycyclic aromatic hydrocarbon (PAH) to Yangtze River sediments and their components**
by J. Zhang (2010), X, 109 pages
ISBN: 978-3-89336-616-3

60. **Weltweite Innovationen bei der Entwicklung von CCS-Technologien und Möglichkeiten der Nutzung und des Recyclings von CO_2**
Studie im Auftrag des BMWi
von W. Kuckshinrichs et al. (2010), X, 139 Seiten
ISBN: 978-3-89336-617-0

61. **Herstellung und Charakterisierung von sauerstoffionenleitenden Dünnschichtmembranstrukturen**
von M. Betz (2010), XII, 112 Seiten
ISBN: 978-3-89336-618-7

62. **Politikszenarien für den Klimaschutz V – auf dem Weg zum Strukturwandel, Treibhausgas-Emissionsszenarien bis zum Jahr 2030**
hrsg. von P. Hansen, F. Chr. Matthes (2010), 276 Seiten
ISBN: 978-3-89336-619-4

63. **Charakterisierung Biogener Sekundärer Organischer Aerosole mit Statistischen Methoden**
von C. Spindler (2010), iv, 163 Seiten
ISBN: 978-3-89336-622-4

64. **Stabile Algorithmen für die Magnetotomographie an Brennstoffzellen**
von M. Wannert (2010), ix, 119 Seiten
ISBN: 978-3-89336-623-1

65. **Sauerstofftransport und Degradationsverhalten von Hochtemperaturmembranen für CO2-freie Kraftwerke**
von D. Schlehuber (2010), VII, 139 Seiten
ISBN: 978-3-89336-630-9

66. **Entwicklung und Herstellung von foliengegossenen, anodengestützten Festoxidbrennstoffzellen**
von W. Schafbauer (2010), VI, 164 Seiten
ISBN: 978-3-89336-631-6

67. **Disposal strategy of proton irradiated mercury from high power spallation sources**
by S. Chiriki (2010), xiv, 124 pages
ISBN: 978-3-89336-632-3

68. **Oxides with polyatomic anions considered as new electrolyte materials for solid oxide fuel cells (SOFCs)**
by O. H. Bin Hassan (2010), vii, 121 pages
ISBN: 978-3-89336-633-0

69. **Von der Komponente zum Stack: Entwicklung und Auslegung von HT-PEFC-Stacks der 5 kW-Klasse**
von A. Bendzulla (2010), IX, 203 Seiten
ISBN: 978-3-89336-634-7

70. **Satellitengestützte Schwerewellenmessungen in der Atmosphäre und Perspektiven einer zukünftigen ESA Mission (PREMIER)**
von S. Höfer (2010), 81 Seiten
ISBN: 978-3-89336-637-8

71. **Untersuchungen der Verhältnisse stabiler Kohlenstoffisotope in atmosphärisch relevanten VOC in Simulations- und Feldexperimenten**
von H. Spahn (2010), IV, 210 Seiten
ISBN: 978-3-89336-638-5

72. **Entwicklung und Charakterisierung eines metallischen Substrats für nanostrukturierte keramische Gastrennmembranen**
von K. Brands (2010), vii, 137 Seiten
ISBN: 978-3-89336-640-8

73. **Hybridisierung und Regelung eines mobilen Direktmethanol-Brennstoffzellen-Systems**
von J. Chr. Wilhelm (2010), 220 Seiten
ISBN: 978-3-89336-642-2

74. **Charakterisierung perowskitischer Hochtemperaturmembranen zur Sauerstoffbereitstellung für fossil gefeuerte Kraftwerksprozesse**
von S.A. Möbius (2010) III, 208 Seiten
ISBN: 978-3-89336-643-9

75. **Characterization of natural porous media by NMR and MRI techniques: High and low magnetic field studies for estimation of hydraulic properties**
by L.-R. Stingaciu (2010), 96 pages
ISBN: 978-3-89336-645-3

76. **Hydrological Characterization of a Forest Soil Using Electrical Resistivity Tomography**
by Chr. Oberdörster (2010), XXI, 151 pages
ISBN: 978-3-89336-647-7

77. **Ableitung von atomarem Sauerstoff und Wasserstoff aus Satellitendaten und deren Abhängigkeit vom solaren Zyklus**
von C. Lehmann (2010), 127 Seiten
ISBN: 978-3-89336-649-1

78. **18th World Hydrogen Energy Conference 2010 – WHEC2010 Proceedings**
Speeches and Plenary Talks
ed. by D. Stolten, B. Emonts (2010)
ISBN: 978-3-89336-658-3

78-1. **18th World Hydrogen Energy Conference 2010 – WHEC2010 Proceedings**
Parallel Sessions Book 1:
Fuel Cell Basics / Fuel Infrastructures
ed. by D. Stolten, T. Grube (2010), ca. 460 pages
ISBN: 978-3-89336-651-4

78-2. **18th World Hydrogen Energy Conference 2010 – WHEC2010 Proceedings**
Parallel Sessions Book 2:
Hydrogen Production Technologies – Part 1
ed. by D. Stolten, T. Grube (2010), ca. 400 pages
ISBN: 978-3-89336-652-1

78-3. **18th World Hydrogen Energy Conference 2010 – WHEC2010 Proceedings**
Parallel Sessions Book 3:
Hydrogen Production Technologies – Part 2
ed. by D. Stolten, T. Grube (2010), ca. 640 pages
ISBN: 978-3-89336-653-8

78-4. **18th World Hydrogen Energy Conference 2010 – WHEC2010 Proceedings**
Parallel Sessions Book 4:
Storage Systems / Policy Perspectives, Initiatives and Cooperations
ed. by D. Stolten, T. Grube (2010), ca. 500 pages
ISBN: 978-3-89336-654-5

78-5. **18th World Hydrogen Energy Conference 2010 – WHEC2010 Proceedings**
Parallel Sessions Book 5:
Stategic Analysis / Safety Issues / Existing and Emerging Markets
ed. by D. Stolten, T. Grube (2010), ca. 530 pages
ISBN: 978-3-89336-655-2

78-6. **18th World Hydrogen Energy Conference 2010 – WHEC2010 Proceedings**
Parallel Sessions Book 6:
Stationary Applications / Transportation Applications
ed. by D. Stolten, T. Grube (2010), ca. 330 pages
ISBN: 978-3-89336-656-9

78 Set (complete book series)

18th World Hydrogen Energy Conference 2010 – WHEC2010 Proceedings
ed. by D. Stolten, T. Grube, B. Emonts (2010)
ISBN: 978-3-89336-657-6

79. **Ultrafast voltex core dynamics investigated by finite-element micromagnetic simulations**
by S. Gliga (2010), vi, 144 pages
ISBN: 978-3-89336-660-6

80. **Herstellung und Charakterisierung von keramik- und metallgestützten Membranschichten für die CO_2-Abtrennung in fossilen Kraftwerken**
von F. Hauler (2010), XVIII, 178 Seiten
ISBN: 978-3-89336-662-0

81. **Experiments and numerical studies on transport of sulfadiazine in soil columns**
by M. Unold (2010), xvi, 115 pages
ISBN: 978-3-89336-663-7

82. **Prompt-Gamma-Neutronen-Aktivierungs-Analyse zur zerstörungsfreien Charakterisierung radioaktiver Abfälle**
von J.P.H. Kettler (2010), iv, 205 Seiten
ISBN: 978-3-89336-665-1

83. **Transportparameter dünner geträgerter Kathodenschichten der oxidkeramischen Brennstoffzelle**
von C. Wedershoven (2010), vi, 137 Seiten
ISBN: 978-3-89336-666-8

84. **Charakterisierung der Quellverteilung von Feinstaub und Stickoxiden in ländlichem und städtischem Gebiet**
von S. Urban (2010), vi, 211 Seiten
ISBN: 978-3-89336-669-9

85. **Optics of Nanostructured Thin-Film Silicon Solar Cells**
by C. Haase (2010), 150 pages
ISBN: 978-3-89336-671-2

86. **Entwicklung einer Isolationsschicht für einen Leichtbau-SOFC-Stack**
von R. Berhane (2010), X, 162 Seiten
ISBN: 978-3-89336-672-9

87. **Hydrogen recycling and transport in the helical divertor of TEXTOR**
by M. Clever (2010), x, 172 pages
ISBN: 978-3-89336-673-6

88. **Räumlich differenzierte Quantifizierung der N- und P-Einträge in Grundwasser und Oberflächengewässer in Nordrhein-Westfalen unter besonderer Berücksichtigung diffuser landwirtschaftlicher Quellen**
von F. Wendland et. al. (2010), xii, 216 Seiten
ISBN: 978-3-89336-674-3

89. **Oxidationskinetik innovativer Kohlenstoffmaterialien hinsichtlich schwerer Lufteinbruchstörfälle in HTR´s und Graphitentsorgung oder Aufarbeitung**
von B. Schlögl (2010), ix, 117 Seiten
ISBN: 978-3-89336-676-7

90. **Chemische Heißgasreinigung bei Biomassenvergasungsprozessen**
von M. Stemmler (2010), xv, 196 Seiten
ISBN: 978-3-89336-678-1

91. **Untersuchung und Optimierung der Serienverschaltung von Silizium-Dünnschicht-Solarmodulen**
von S. Haas (2010), ii, 202 Seiten
ISBN: 978-3-89336-680-4

92. **Non-invasive monitoring of water and solute fluxes in a cropped soil**
by S. Garré (2010), xxiv, 133 pages
ISBN: 978-3-89336-681-1

93. **Improved hydrogen sorption kinetics in wet ball milled Mg hydrides**
by L. Meng (2011), II, 119 pages
ISBN: 978-3-89336-687-3

94. **Materials for Advanced Power Engineering 2010**
ed. by J. Lecomte-Beckers, Q. Contrepois, T. Beck and B. Kuhn
(2010), 1327 pages
ISBN: 978-3-89336-685-9

95. **2D cross-hole MMR – Survey design and sensitivity analysis for cross-hole applications of the magnetometric resistivity**
by D. Fielitz (2011), xvi, 123 pages
ISBN: 978-3-89336-689-7

96. **Untersuchungen zur Oberflächenspannung von Kohleschlacken unter Vergasungsbedingungen**
von T. Melchior (2011), xvii, 270 Seiten
ISBN: 978-3-89336-690-3

97. **Secondary Organic Aerosols: Chemical Aging, Hygroscopicity, and Cloud Droplet Activation**
by A. Buchholz (2011), xiv, 134 pages
ISBN: 978-3-89336-691-0

98. **Chrom-bezogene Degradation von Festoxid-Brennstoffzellen**
von A. Neumann (2011), xvi, 218 Seiten
ISBN: 978-3-89336-692-7

99. **Amorphous and microcrystalline silicon applied in very thin tandem solar cells**
by S. Schicho (2011), XII, 190 pages
ISBN: 978-3-89336-693-4

100. **Sol-gel and nano-suspension electrolyte layers for high performance solid oxide fuel cells**
by F. Han (2011), iv, 131 pages
ISBN: 978-3-89336-694-1

101. **Impact of different vertical transport representations on simulating processes in the tropical tropopause layer (TTL)**
by F. Plöger (2011), vi, 104 pages
ISBN: 978-3-89336-695-8

102. **Untersuchung optischer Nanostrukturen für die Photovoltaik mit Nahfeldmikroskopie**
von T. Beckers (2011), xiii, 128 Seiten
ISBN: 978-3-89336-696-5

103. **Impact of contamination on hydrogenated amorphous silicon thin films & solar cells**
by J. Wördenweber (2011), XIV, 138 pages
ISBN: 978-3-89336-697-2

104. **Water and Organic Nitrate Detection in an AMS: Laboratory Characterization and Application to Ambient Measurements**
by A. Mensah (2011), XI, 111 pages
ISBN: 978-3-89336-698-9

105. **Entwicklung eines neuen Konzepts zur Steuerung der thermischen Ausdehnung von glaskeramischen Verbundwerkstoffen mit angepasster Fließfähigkeit am Beispiel der Hochtemperatur-Brennstoffzelle**
von E. Wanko (2011), xi, 134 Seiten
ISBN: 978-3-89336-705-4

106. **Tomographic reconstruction of atmospheric volumes from infrared limb-imager measurements**
by J. Ungermann (2011), xiv, 153 pages
ISBN: 978-3-89336-708-5

107. **Synthese und Identifizierung von substituierten Mg-Al-Cl Doppelhydroxidverbindungen mit Schwerpunkt IR-Spektroskopie**
von B. Hansen (2011), XII, 121 Seiten
ISBN: 978-3-89336-709-2

108. **Analysis of spatial soil moisture dynamics using wireless sensor networks**
by U. Rosenbaum (2011), xxii, 120 pages
ISBN: 978-3-89336-710-8

109. **Optimierung von APS-ZrO2-Wärmedämmschichten durch Variation der Kriechfestigkeit und der Grenzflächenrauhigkeit**
von M. E. Schweda (2011), 168 Seiten
ISBN: 978-3-89336-711-5

110. **Sorption of a branched nonylphenol isomer and perfluorooctanoic acid on geosorbents and carbon nanotubes**
by C. Li (2011), X, 102 pages
ISBN: 978-3-89336-716-0

111. **Electron Transport in the Plasma Edge with Rotating Resonant Magnetic Perturbations at the TEXTOR Tokamak**
by H. Stoschus (2011), iv, 113 pages
ISBN: 978-3-89336-718-4

112. **Diffusion and Flow Investigations in Natural Porous Media by Nuclear Magnetic Resonance**
by N. Spindler (2011), viii, 144 pages
ISBN: 978-3-89336-719-1

113. **Entwicklung und Erprobung des Hygrometer for Atmospheric Investigations**
von T. Klostermann (2011), IV, 118 Seiten
ISBN: 978-3-89336-723-8

114. **Application of functional gene arrays for monitoring influences of plant/seasons on bacterial functions and community structures in constructed wetlands (Bitterfeld, Germany)**
by J. Ning (2011), xiv, 157 pages
ISBN: 978-3-89336-724-5

115. **Wasseraustrag aus den Kathodenkanälen von Direkt-Methanol-Brennstoffzellen**
von A. Schröder (2011), VII, 228 Seiten
ISBN: 978-3-89336-727-6

116. **CITYZEN Climate Impact Studies**
ed. by M. Schultz (2011), 45 pages
ISBN: 978-3-89336-729-0

117. **Software Tools zum interoperablen Austausch und zur Visualisierung von Geodatensätzen über das Internet**
von M. Schultz, M. Decker, S. Lührs (2011), iv, 156 Seiten
ISBN: 978-3-89336-730-6

118. **Optimierung eines Leichtbaudesigns für ein SOFC-Brennstoffzellenstack**
von T. Nguyen-Xuan (2011), III, 154 Seiten
ISBN: 978-3-89336-732-0

119. **Institute of Energy and Climate Research IEK-6:**
Nuclear Waste Management & Reactor Safety Report 2009/2010
Material Science for Nuclear Waste Management
ed. by M. Klinkenberg, S. Neumeier, D. Bosbach (2011), 242 pages
ISBN: 978-3-89336-735-1

120. **Fate of the Antibiotic Sulfadiazine in Yangtze River Sediments: Transformation, Sorption and Transport**
by N. Meng (2011), XII, 111 pages
ISBN: 978-3-89336-736-8

121. **Thermodynamische Eigenschaften gasförmiger und kondensierter Verbindungen für Hochtemperaturanwendungen**
von T. Markus (2011), II, 131 Seiten
ISBN: 978-3-89336-728-3

122. **Ein neues LIF-Instrument für flugzeug- und bodengebundene Messungen von OH- und HO_2-Radikalen in der Troposphäre**
von S. Broch (2011), IV, 160 Seiten
ISBN: 978-3-89336-742-9

123. **Processes in the Yangtze River System - Experiences and Perspectives**
Workshop-Proceedings
ed. by S. Küpper, G. Subklew, R.-D. Wilken (2011), 83 pages
ISBN: 978-3-89336-744-3

124. **Thermo-Mechanical Properties of Mixed Ion-Electron Conducting Membrane Materials**
by B. Huang (2011), 130 pages
ISBN: 978-3-89336-746-7

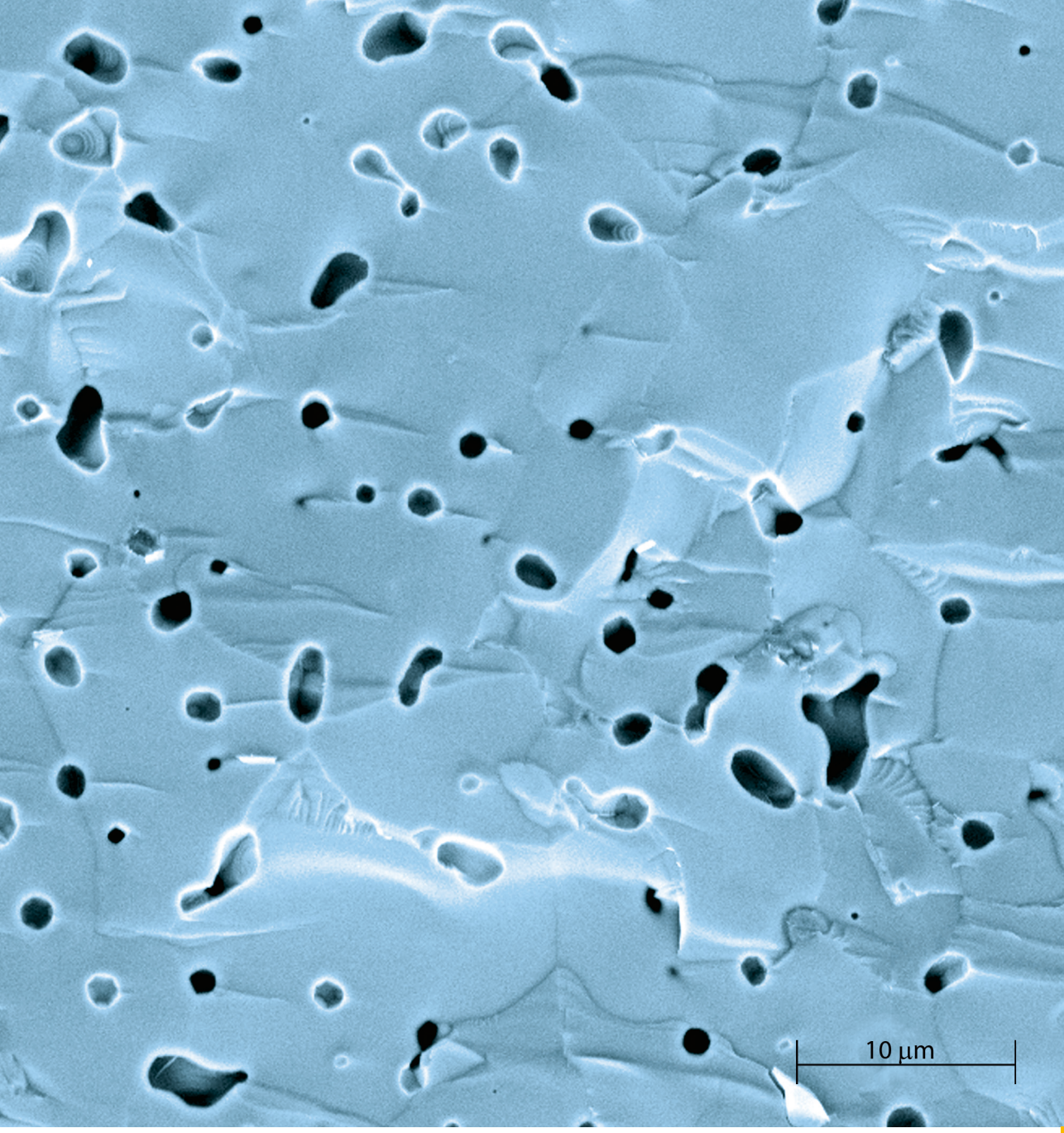

Energie & Umwelt / Energy & Environment
Band / Volume 124
ISBN 978-3-89336-746-7

JÜLICH
FORSCHUNGSZENTRUM